Quantum-Well Lasers and Their Applications☆

LJ Mawst, University of Wisconsin-Madison, Madison, WI, USA
N Tansu, Lehigh University, Bethlehem, PA, USA
AZMS Rahman, University of Malaya, Kuala Lumpur, Malaysia

1 Introduction

Quantum-well (QW) active semiconductor lasers enjoy widespread commercial use in optoelectronic applications ranging from high-power sources for medical therapy, material processing, laser printing, and pumps for solid-state lasers to lower output power single-mode, single-frequency sources for telecommunications. The advent of highly controllable semiconductor growth technologies, such as molecular beam epitaxy (MBE) and metal-organic chemical vapor deposition (MOCVD), led to device quality, nearly ideal QW materials in the 1980s. Since then, there has been continuous improvement in QW-based device performance. Strained-layer QWs, such as InGaAs/GaAs and InGaAs/InP, have become the workhorse materials for near-infrared (IR) diode laser sources. More recently, the large energy band gap bowing in dilute nitride materials is further opening up the emission wavelength windows, which is otherwise limited by material strain relaxation.

☆*Change History:* July 2015. A.Z.M.S. Rahman added keywords, updated Section 6.2, references and did minor editing.

 doi:10.1016/B978-0-12-803581-8.00825-0

In this chapter, we review the general characteristics of QW lasers in Section 2, with emphasis on the device physics and design issues for QW lasers which distinguish them from bulk active-layer double-heterostructure (DH) semiconductor diode lasers. As a result of the thin-active, QW active region, the concept of current injection efficiency becomes of paramount importance, strongly influencing the optical gain and device temperature sensitivity. Highly strained QWs, new materials such as the dilute nitrides, and type-II QWs are active areas of current research in QW lasers. Nonideal properties of QW materials, presented in Section 3, can significantly influence the optical properties and directly impact the device performance. Material strain relaxation considerations ultimately limit the wavelength extension in virtually all QW material systems, and highly strained QWs are quite useful for accessing wavelength regions needed for a variety of applications. QW laser design considerations for high-output-power applications are presented in Section 4. Emphasis is placed on the underlying factors that influence the device temperature sensitivity and ultimately limit the optical output power. Al-free active region diode lasers can offer performance and reliability advantages over conventional Al-containing QWs for high-output-power applications, particularly within the $\lambda \sim 0.7$–0.8-μm wavelength region. The properties of high-power near-IR ($\lambda \sim 0.7$–1.2 μm) InGaAs/GaAs QW and Al-free InGaAsP/GaAs QW diode lasers are reviewed. Longer wavelength sources, reaching into the telecommunication range ($\lambda \sim 1.3$–1.5 μm), generally suffer from higher device temperature sensitivity and are discussed in Section 5. New QW material systems, such as the dilute nitride InGaAsN QWs, demonstrate device performance in the $1.3-$μm wavelength region now surpassing conventional InP-based devices. Yet, the influence of these QW materials on device performance is still an area of active research. Visible diode laser sources based on the InGaN/(Al)GaN QW material system are strongly influenced by the piezoelectric effects inherent with these QW materials. Unique issues, not observed in the near-IR emitting QWs, such as reduced optical gain as a result of poor electronic wave function overlap induced by the built-in electric fields, play an important role in these devices. The design and material issues associated with these QW materials are presented in Section 6.

2 General Characteristics of QW Lasers

2.1 Type-I QWs

When a thin semiconductor laser active region approaches the width of de Broglie wavelength ($\lambda = h/p$) of the electron and hole, quantum size effects become significant and the injected electrons and holes behave as two-dimensionally confined carriers (Dingle *et al.*, 1974; Holonyak *et al.*, 1980). if the electrons and holes are spatially confined to the same lower energy band-gap layer, then the QW is referred to as a type-I QW. This two-dimensional (2D) confinement modifies the density of states (DOS) in the conduction and valence band compared with that of bulk material, directly impacting the optical gain properties of the active region (Sugimura, 1983). In addition to a modification in the DOS (to stair-case like) over that of a bulk active region, the quantum size effects shift the transition energies above that of the bulk conduction and valence band edges, allowing for emission wavelength tuning through active layer thickness changes. The computed effective energy gap between the first confined electron state in the conduction band and the first confined heavy-hole state in the valence band for an $In_{1-x}Ga_xAs/GaAs$ type-I QW is shown in **Figure 1** for various values of Ga content and QW thickness. The limit of a thick active layer yields the strained band-gap energy for the bulk $In_{1-x}Ga_x$ As material.

A detailed account of the history of the QW and its first application to lasers was given by Henry (1993). The first QW injection laser which operated CW at room temperature was grown by MOCVD and reported by Dupuis *et al.* (1978). Perhaps most important for QW lasers, the small active volume of the QW directly scales down the amount of current required to reach transparency (i.e., J_{tr}, transparency current density is reduced) over thick active layer devices. This fact generally leads to significantly reduced threshold current densities for QW lasers over that for bulk active layer devices. However, if the threshold gain requirements are high, carrier bandfilling in the QW can lead to significant active region carrier leakage and a resulting drop in the current injection efficiency, as discussed in Section 2.4. For example, short-cavity-length single-QW (SQW) active region lasers exhibit unusually high-threshold current densities and low external differential quantum efficiencies (DQEs) as a result of the excessive threshold gain requirement originating from the large mirror losses (Zory *et al.*, 1986).

Knowing the relationship between optical gain and injected current density is necessary for calculating the threshold current density of the QW laser. The relationship between the injected carrier density and the quasi-Fermi-level positions for the electrons in the conduction band and the holes in the valence band allows the optical gain to be evaluated as a function of active layer carrier density. However, the relationship between carrier density and injected current density is significantly more complex, since the details of the carrier recombination mechanisms must be known, as discussed further in Section 2.4.

A simplified gain model can be used to understand how the peak optical gain is affected by the QW design. The simplified peak gain, g_p, as a function of quasi-Fermi levels (Chuang, 1995), with the assumption of zero scattering linewidth and only one occupied conduction and valence subband, is given by

$$g_p(E) = g_m[f_c(E = E_{h1}^{e1}) - fv(E = E_{h1}^{e1})] \quad [1]$$

The E_{h1}^{e1} term in eqn [1] is defined as the energy-level separation between the first conduction and the first valence subbands in the QW active region. The g_m value represents the gain coefficient determined by transition matrix element and the 2D reduced DOS.

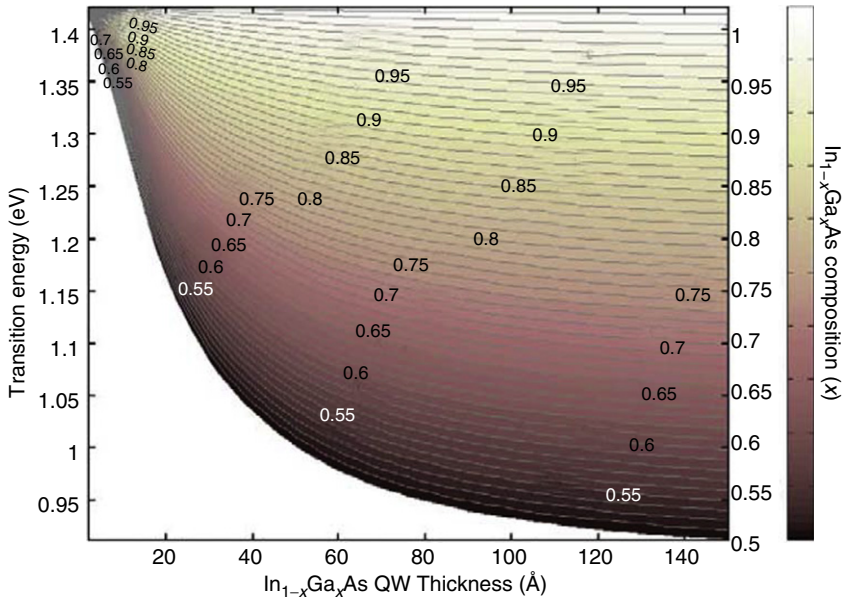

Figure 1 Computed transition energies for an $In_{1-x}Ga_xAs/GaAs$ quantum-well (QW) based on an eight-band $k \cdot p$ simulation.

For an undoped QW active region, the electron carrier density (n) is assumed to be equal to the hole carrier density (p). Taking the approximation used by Vahala and Zah (1988), the quasi-Fermi level of the conduction band (f_c) and the valence band (f_v) can be approximated as

$$f_c(E = E_{h1}^{e1}) \cong 1 - e^{-n/n_c} \quad [2]$$

$$f_v(E = E_{h1}^{e1}) \cong e^{-p/n_v} \quad [3]$$

The effective DOS for the conduction and valence band can be expressed as

$$n_c \cong \frac{m_e^* kT\pi}{h^2 L_z} \sum_{n=1}^{\infty} e^{(Eel - Een)/kT} \quad [4]$$

$$n_v \cong \frac{m_h^* kT\pi}{h^2 L_z} \sum_{n=1}^{\infty} e^{(E_{hn} - E_{hl})/kT} \quad [5]$$

For the case of an undoped QW (with the condition $n=p$), the peak gain (eqn [1]) can then be expressed as a function of carrier density:

$$g_p = g_m(1 - e^{-n/n_c} - e^{-n/n_v}) \quad [6]$$

$$g_p = g_m(1 - e^{-n/n_c} - e^{-n/R \cdot n_c}) \quad [7]$$

Note that the R ratio can be expressed as

$$R = \frac{n_v}{n_c} = \frac{m_{hh}^*}{m_e^*} \quad [8]$$

The transparency carrier density is defined as the carrier density at which the peak gain g_p is equal to zero. The condition of the $g_p = 0$ occurs when $e^{-n/n_c} + e^{-n/n_v} = 1$. The g_m parameter can be expressed as function of the QW thickness, transition matrix element, and reduced effective mass, as given by

$$g_m = \frac{\pi e^2}{n_r c \varepsilon_0 m_0 \omega} |M_T|^2 \frac{m_r}{\pi^2 L_Z} \quad [9]$$

As an example, comparing the g_m parameter for a conventional 980-nm emitting (7-nm thick) $In_{0.2}Ga_{0.8}As$ QW with a thin highly strained 1200-nm emitting (7-nm thick) $In_{0.4}Ga_{0.6}As$ QW, we can evaluate the ratio of g_m for both QWs, given by

$$\frac{g_m(1200)}{g_m(980)} = \frac{\left[|M_T|^2 \frac{m_r}{\omega L_z}\right]_{1200}}{\left[|M_T|^2 \frac{m_r}{\omega L_z}\right]_{980}} \quad [10]$$

Assuming the following values for the two QW designs:

(1) a 1200-nm emitting InGaAs QW
$m_r = 0.0446\ m_o$
$L_z = 7$ nm

$$R = \frac{0.48 m_o}{0.0582 m_o} = 8.25$$

(2) a 980-nm emitting InGaAs QW
$m_r = 0.0519 m_o$
$L_z = 7$ nm

$$R = \frac{0.48 m_o}{0.0582 m_o} = 8.25$$

The matrix element $|M_T|^2$ for transverse electric (TE)-polarized gain in $In_xGa_{1-x}As$ active region material can be expressed (Coldren and Corzine, 1995) as follows:

$$|M_T|^2 = \frac{2}{3}\frac{(28.8 - 6.6x)m_o}{2} \quad [11]$$

Thus, the ratio of g_m parameters for both QWs can be obtained by

$$\frac{g_m(1200)}{g_m(980)} = \frac{\left[|M_T|^2 \frac{m_r}{L_z}\right]_{1200}}{\left[|M_T|^2 \frac{m_r}{L_z}\right]_{980}} \underbrace{\frac{\omega_{980}}{\omega_{1200}}}_{=1.255} \quad [12a]$$

$$\frac{g_m(1200)}{g_m(980)} = (0.818)(1.225) = 1.002 \quad [12b]$$

It is important to note that the peak of gain of the QW active region (eqn [7]) depends on both the g_m parameter and the quasi-Fermi-level separation term. The g_m parameters for both QW active regions for 1200 and 980 nm are found to be relatively similar. The reduced m_r will reduce the g_m value for the highly strained $In_{0.4}Ga_{0.6}As$ QW; however, the lower frequency ω for the $In_{0.4}Ga_{0.6}As$ QW leads to similar g_m value with that of $In_{0.2}Ga_{0.8}As$ QW. The reduced DOS in the highly strained $In_{0.4}Ga_{0.6}As$ QW, primarily from its lower electron effective mass, leads to improved quasi-Fermi-level separation and lower transparency carrier density. The relative peak gain as a function of carrier density for the two QW structures is shown in **Figure 2**, indicating that a higher optical gain is obtained for the highly strained QW considered here. The slight reduction of transparency carrier density is also observed in the case of $In_{0.4}Ga_{0.6}As$ QW, which is primarily attributed to the reduced DOS from its lower electron and hole effective masses. It is important to note that accurate modeling of the gain and carrier density relation needs to take into account the impact of valence band mixing by using a six-band $k \cdot p$ model for the energy dispersion relation (Coldren and Corzine, 1995; Chuang, 1995). Experimental gain studies on these two important QW systems are further discussed in Section 2.5.3.

2.2 Type-II QWs

In a type-I QW, the longest emission wavelength achievable is limited by the (strained) band-gap energy of the QW material. For example, in the InP-based material system, the conventional approach of using a highly strained $In_xGa_{1-x}As$ QW encounters difficulties for wavelength extension beyond $\lambda \sim 2\ \mu m$, due to strain relaxation. By contrast, a type-II QW, such as the InGaAs/GaAsSb QW structure on an InP substrate, removes this constraint and allows for spatially indirect electron–hole recombination to occur with a corresponding transition energy which is smaller than the energy band gap of either the InGaAs (electron well) or the

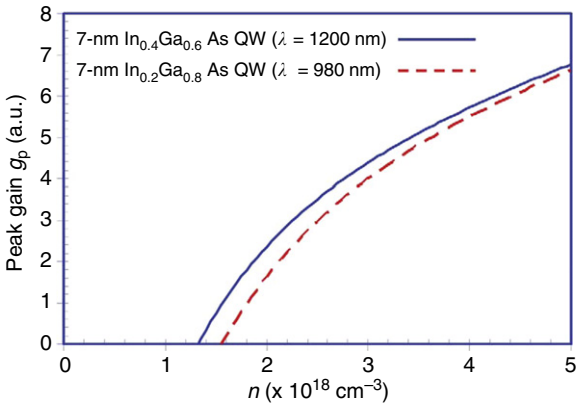

Figure 2 Comparison of peak optical gain for InGaAs quantum-well (QW) with similar thickness (7 nm). The two QW structures consist of In contents of 20 and 40%, respectively, for 980-nm and 1200-nm emission.

GaAsSb (hole well). The primary drawback of such a structure is that there is reduced spatial overlap (i.e., reduced optical matrix element) of the electron and hole wavefunction, compared with that of a type-I QW. In addition, the spatial charge separation in a type-II QW leads to a built-in electric field with a magnitude that depends on the carrier density. This built-in electric field generally results in an undesirable blue-shift that is carrier density dependent, so that the emission wavelength may strongly depend on the threshold gain. Such InP-based type-II QW structures have been realized by Peter and coworkers, employing a superlattice active region consisting of compressively strained InGaAs and tensile-strained GaAsSb (Peter *et al.*, 1999).

Type-II QWs on GaSb substrates have been extensively researched and incorporated into mid-IR laser structures. The type-II InGaSb/AlSb W-structure was proposed (Meyer *et al.*, 1995) and first implemented on a GaSb substrate, as a means to optimize the electron–hole wave function overlap and retain a 2D DOS. Such structures exhibit emission over a wide wavelength range ($\lambda = 3$–6 μm) within the mid-IR spectral region. The reduced wave function overlap may also provide a possible mechanism for Auger recombination suppression (Meyer *et al.*, 1995). Recently, GaSb-based type-II QW lasers have demonstrated $\lambda = 3.7$-μm emission with room-temperature (RT) continuous-wave (CW) operation (Kim *et al.*, 2008). GaAs-based type-II QWs, which employ strained GaInAs/GaAsSb-active regions, have also been reported previously, as a means to extend the emission wavelength of GaAs-based sources into the telecommunication range ($\lambda = 1.3$–1.55 μm) (Dowd *et al.*, 1999). Furthermore, the addition of nitrogen into the electron wells of such structures would allow for additional wavelength extension, and design studies indicate that a multiple-stage GaInNAs–GaAsSb type-II QW 'W' active region holds potential for realizing GaAs-based diode lasers with emission wavelengths beyond $\lambda = 1.5$ μm (Vurgaftman *et al.*, 2003b).

Type-II QW structures on InP may hold potential for efficient mid-IR emission, with significant advantages over GaSb-based designs. Immature GaSb-based growth and processing have somewhat hindered the progress of GaSb-based laser technology. On the other hand, InP offers many advantages over GaSb, such as better thermal conductivity, the ability to utilize a buried heterostructure design, and optical pumping capability with high-power, high-efficiency, near-IR diode lasers, since InP is transparent at 0.98 μm. For example, the computed type-II InGaAs/GaAsSb W-structure energy band diagram is shown in **Figure 3**, along with the electron and hole wave functions. **Figure 4** illustrates the compositional dependence of the optical matrix element and emission wavelength from the type-II transition of the InGaAs/GaAsSb W-structure on an InP substrate. These design studies have been performed using a 10-band $k \cdot p$ simulation, as described by Vurgaftman *et al.* (2003b).

To illustrate the potential of the type-II QW structure, it is instructive to compare with a conventional type-I highly strained $In_{0.77}Ga_{0.23}As$ (11.5 nm) ($\Delta a/a \sim -1.65\%$) multiple QW (MQW) reported by Mitsuhara *et al.* (1998). For QW structures, the active region has a net strain (ε^*) given by

$$\varepsilon^* = \frac{\varepsilon_w L_w + \varepsilon_b L_b}{L_w + L_b} \quad [13]$$

where ε_w, L_w, ε_b, and L_b are well strain, well thickness, barrier strain, and barrier thickness, respectively. The calculated emission wavelength of the MQW described by Mitsuhara *et al.* (1998) is 2091 nm at 300 K, which is in accordance with the experiential result of the lasing wavelength at 2070 nm (Huang *et al.*, 2009). Consider a W-structure consisting of $In_{0.7}Ga_{0.3}As$ (4 nm)/$GaAs_{0.4}Sb_{0.55}$ (3.5 nm)/$In_{0.7}Ga_{0.3}As$ (4 nm) with the same total thickness of 11.5 nm as the highly strained type-I QW reported by Mitsuhara *et al.* (1998). The value of ε^* is calculated to be –0.953% for this W-structure with an emission wavelength of 3163 nm and an interband optical matrix element value only 35% that of the type-I QW described by Mitsuhara *et al.* (1998). Thus, longer emission wavelength can be achieved with lower net strain from the type-II QW, although to achieve sufficient optical gain from the type-II QW structure multiple stages of the W-structure are required.

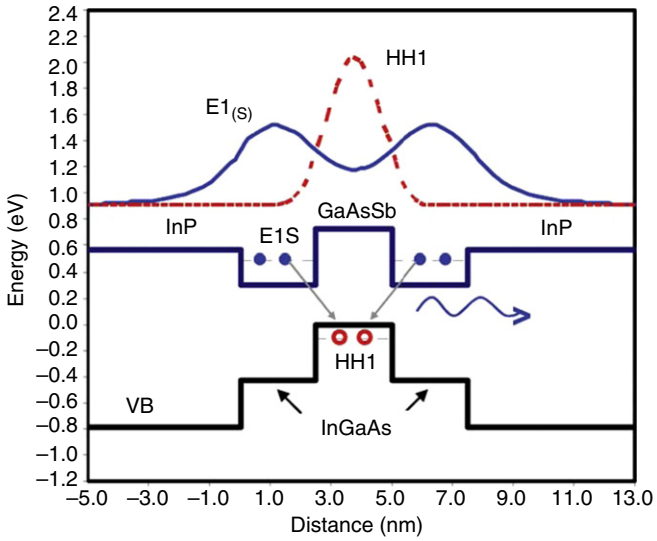

Figure 3 Energy band diagram and selected wavefunction components designed for emission around 2.1 μm of latticed-matched $In_{0.53}Ga_{0.47}As$ (2.5 nm)/$GaAs_{0.51}Sb_{0.49}$ (2.5 nm)/$In_{0.53}Ga_{0.47}As$ (2.5 nm) type-II quantum-wells (QWs) with InP barrier.

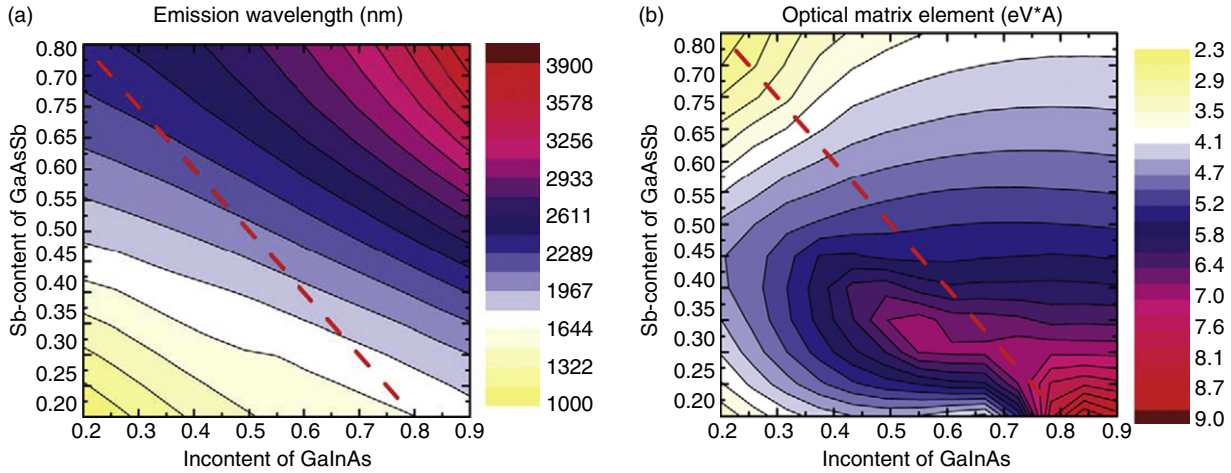

Figure 4 Contour plots for (a) emission wavelength and (b) optical matrix element at the zone center at room temperature of InGaAs (2.5 nm)/GaAsSb (2.5 nm) type-II 'W' quantum-well (QW) structure as a function of In content in electron wells and Sb content in hole wells. The electron and hole QW widths are arbitrarily fixed at 2.5 nm. The dashed lines show the strain-compensated compositions and the star indicates the lattice-matched compositions (Huang *et al.*, 2009).

2.3 Strained-Layer QWs

Strained QW semiconductors and heterostructures have been studied for several decades because they possess many advantages for device applications. The main effect of strain on the bandstructure is a deformation potential that leads to a dramatic change of the optical properties in III–V semiconducting materials (Adams, 1986; Yablonovitch and Kane, 1986). This change can be used in designing improved laser performance over lattice-matched QW structures. In the conduction band of III–V semiconductors, biaxial strain shifts the position of the band edge and has a small effect on the conduction band effective mass. However, a more dramatic effect can be observed in the valence bandstructure and hole effective masses. In addition to a change in the band-gap energy, the energy difference between the light- and heavy-hole bands also changes and the compressive or tensile strain breaks the degeneracy of the heavy- and light-hole valence bands. Larger values of strain will move the hole subband energy separation further apart. Finally, due to the changes in the coupling between the light- and heavy-hole bands, the in-plane hole effective mass is reduced, almost by a factor of 3 or more. Since the DOS in the valence band is reduced with the reduction in effective mass, it becomes comparable to that in the conduction band, and the population inversion becomes more efficient, that is, lower transparency current density (due to symmetry between conduction and valence bands). As a result of the strain-induced band

structure modification, the differential gain dg/dN increases (Corzine *et al.*, 1990). In addition, the Auger recombination rates were predicted to change as the amount of strain changes, although this has been proven difficult to confirm experimentally.

There is another important effect of strain in the output characteristics of QW lasers. Optical transitions between electron and heavy-hole bands are coupled to the TE mode, while the transitions involving light-hole bands are coupled to the transverse magnetic (TM) modes. In a lattice-matched QW laser, the laser output is generally a mixture of TE and TM modes. With the application of compressive strain (CS) the modes are more TE-like (TM mode suppressed), and with the application of tensile strain the modes are more TM-like (TE mode suppressed), due to the strain-induced changes in the valence band structure that results in predominately heavy-hole (TE) or light-hole (TM) occupancy.

Experimental data confirm the theoretical predictions that a strained QW laser can demonstrate very low-threshold current densities (see Sections 2.5.3 and 4.2). This is because the laser can operate with a higher differential gain and lower transparency current density, compared to a bulk laser, for the same threshold gain. A larger number of QWs in an MQW laser result in higher gain, which can overcome the relatively high mirror losses for short-cavity-length devices. This is important for high-speed devices, where short cavity lengths are necessary for high $f_{3\ dB}$. For example, large reductions in transparency current densities are theoretically predicted for strained QWs (Yablonovitch and Kane, 1986; Corzine *et al.*, 1990). In addition, the differential gain, which is related to the ultimate modulation speed of QW lasers, is improved by as much as a factor of 2 for an unstrained QW over bulk (Zmudzinski *et al.*, 1991) and a factor of 7 for a strained QW over bulk (Lester *et al.*, 1991), implying that strained QW lasers should be faster (Offsey *et al.*, 1991) as well as having lower threshold currents than their unstrained counterparts.

2.4 Injection Efficiency and Carrier Recombination

Relating the optical gain of the QW to the current injected into the device allows the threshold current density to be calculated, provided the threshold gain requirement is known. One needs to first understand what fraction of the injected current leads to carrier recombination within the QW. In addition, only a fraction of carriers that will recombine radiatively within the QW produces optical gain. Since the carrier capture (and transport) into the QW and the emission of carriers out of the QW are both temperature-sensitive processes, the relationship of the optical gain to the injected current is also expected to be temperature dependent. The current injection efficiency (η_{inj}) of a QW laser is defined as the fraction of the injected current that recombines, both radiatively and nonradiatively, in the QW active region of the laser. The current injection efficiency (η_{inj}) is distinct from the internal efficiency (η_i), as the internal efficiency is defined as the fraction of the injected current that recombines radiatively in the QW active region (Lim *et al.*, 1991). Thus, the internal efficiency is also referred to as the radiative efficiency. The relationship between the internal efficiency and the current injection efficiency can be written as

$$\eta_i = \eta_{inj}\eta_{Quantum_{Efficiency}} \quad [14]$$

The $\eta_{Quantum\_Efficiency}$ ($=R_{rad}/R_{total}$) is defined as the fraction of the total recombination in the QW ($R_{total}=R_{rad}+R_{nonrad}$) that recombines radiatively (R_{rad}). The nonradiative recombination in the QW (R_{nonrad}) may consist of recombination through monomolecular or Auger processes. Note that the above laser threshold, where stimulated emission lifetime becomes very short, the $\eta_{Quantum\_Efficiency}$ is usually assumed to be ~ 1.

The concept of the current injection efficiency of QW lasers is often misunderstood in the literature (Smowton and Blood, 1997). The current injection efficiency of a QW laser is generally assumed to be the same in the below-threshold, at-threshold, and above-threshold operating regimes. The current injection efficiency of a properly designed DH laser generally has similar values for the above- and at-threshold conditions. However, as the dimensionality of the active region is reduced, the at-threshold and above-threshold current injection efficiencies of the active region cannot be assumed as similar. This represents a fundamental difference between thin QW active devices and thick bulk active layer devices, and has a significant impact on device performance.

The current injection efficiency (η_{inj}) consists of the structural current injection efficiency ($\eta_{inj\_structure}$) and the current injection efficiency of the QW (η_{inj_QW}), which can be expressed as

$$\eta_{inj_X} = \eta_{inj_{structure}}\eta_{inj_{QW}X} \quad [15]$$

where X represents the below-threshold (below_th), at-threshold (at_th), or above-threshold (above_th) conditions. Under most cases, the $\eta_{inj\_structure}$ can be assumed as constant over a limited temperature regime. This assumption is typically very good for wide-stripe lasers with a stripe width (w) of many times the diffusion length, as the lateral current spreading and diffusion in such broad-area lasers play a limited role. The $\eta_{inj\_structure}$ will also play a role in the lasers that have poor interfaces or defect recombination outside of the QW active region or within the separate-confining heterostructure (SCH) barrier regions, as these carrier losses will lead to a reduction of the $\eta_{inj\_structure}$.

The output power of semiconductor lasers can be expressed as a function of the physical parameters

$$P_{\text{output}} = \eta_{\text{diff}_{\text{ext}}}(\mathcal{F} - \mathcal{F}_{\text{th}})A\frac{E_{\text{p}}}{q} \quad [16]$$

with the J and J_{th} representing the injected and threshold current densities, $\eta_{\text{diff\_ext}}$ the external differential efficiency, and A the area of the laser stripe, respectively. The E_{p} and q correspond to the photon energy of the lasing wavelength and the electron charge, respectively. The external differential efficiency ($\eta_{\text{diff\_ext}}$) can be expressed as

$$\eta_{\text{diff}_{\text{ext}}} = \eta_{\text{inj}_{\text{above}}\text{th}}\frac{\alpha_{\text{m}}(L)}{\alpha_{\text{i}} + \alpha_{\text{m}}(L)} \quad [17]$$

The $\eta_{\text{inj\_above\_th}}$ is the differential fraction of the injected current that recombines in the QW, after lasing occurs. The modal gain is clamped in the QW at and above laser threshold; however, this does not necessarily lead to full clamping of carriers in the QW or SCH regions above threshold (Nagarajan and Bowers, 1993). The full or partial clamping of carriers in the QW above laser threshold can lead to the $\eta_{\text{inj\_above\_th}}$ having very different values from the at-threshold current injection efficiency. The commonly used method of cavity-length analysis (CLA), which involves measuring $\eta_{\text{diff\_ext}}$ values for various cavity-length devices, will only result in the extraction of $\eta_{\text{inj\_above\_th}}$ value and α_{i}. Note that an experimental method to extract the $\eta_{\text{inj\_below\_th}}$ value has not been reported.

The threshold current density, J_{th}, of QW lasers can be expressed as a function of device parameters, which include transparency current density (J_{tr}), the at-threshold current injection efficiency ($\eta_{\text{inj\_at\_th}}$), the material gain parameter (g_{oJ}), and the internal loss (α_{i}) (Coldren and Corzine, 1995):

$$\mathcal{F}_{\text{th}} = \frac{\mathcal{F}_{\text{tr}}}{\eta_{\text{inj}_{\text{at}}\text{th}}}\exp\left(\frac{\alpha_{\text{i}} + (1/L)\ln(1/R)}{\Gamma g_{\text{oJ}}}\right) \quad [18]$$

The $\eta_{\text{inj\_at\_th}}$ is defined as the fraction of the injected current that recombines in the QW active region near the threshold condition. Since no method has been put forth for the experimental extraction of $\eta_{\text{inj\_below}}$ or $\eta_{\text{inj\_at\_th}}$, it is important to have an accurate model to estimate the value and understand the dependence on temperature and carrier density.

Employing a rate equation analysis, a general equation for current injection efficiency of a QW for the below- and at-threshold conditions under the assumption of low photon density (S) was given by Tansu and Mawst (2005)

$$\eta_{\text{inj}_{\text{below}}}(S \to 0) \cong \frac{1}{\left[1 + \frac{\tau_{\text{bw}}}{\tau_{\text{b}}}\left(1 + \frac{\tau_{\text{QW\_total}}}{\tau_{\text{e}}}\right)\right]} \quad [19]$$

with τ_{bw} as the total carrier transport time, τ_{b} as the total recombination lifetime in the SCH region, $\tau_{\text{QW\_total}}$ as the total recombination lifetime in the QW active region, and τ_{e} as the thermionic carrier escape lifetime. **Figure 5** indicates lifetimes associated with the carrier escape and recombination paths in the SCH QW laser, which were utilized in deriving eqn [19]. Note that to obtain the complete current injection efficiency below threshold, the value from eqn [19] must be multiplied by $\eta_{\text{inj\_structure}}$ value, as in eqn [15].

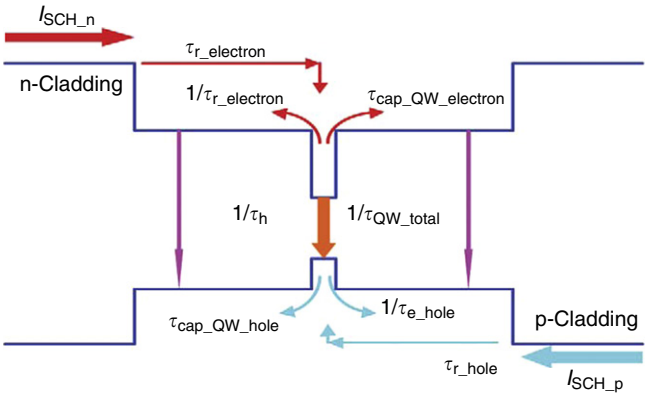

Figure 5 Schematic diagram illustrating the capture and escape times used in the injection efficiency model (Tansu and Mawst, 2005).

The thermionic escape lifetime ($\tau_{e\_e,h}$ for electrons and holes, respectively) of the carriers in the QW can also be expressed as (Tansu and Mawst, 2005)

$$\frac{1}{\tau_{e_e,h}} \propto \frac{1}{N_{QW}L_z} T^2 \exp\left(-\frac{\Delta E_{b_e,h}}{k_B T}\right) \quad [20]$$

with k_B as the Boltzmann constant, T as the temperature, N_{QW} as the carrier density in QW, L_z as the thickness of QW, and $\Delta E_{b\_e,h}$ as the carrier confinement energy of the QW (for electrons and holes, respectively). The total thermionic carrier escape time of the QW (τ_e) can be expressed as functions of the $\tau_{e\_electron}$ and τ_{e_holes} as $1/\tau_e = 1/\tau_{e\_electron} + 1/\tau_{e\_holes}$. The escape phenomenon is dominated by the escape rate of the carriers with the fastest escape time. Once the carriers escape, the carriers in the QW and SCH will redistribute themselves to maintain charge neutrality in the QW and SCH due to the high mobility of the carriers. Note that all the lifetimes shown in **Figure 5** are functions of the carrier density in the QW and temperature specific to each QW active region under study. A large thermionic carrier escape rate will lead to a reduction in τ_e and τ_b, which will in turn lead to severe degradation of the $\eta_{inj\_QW\_below\_th}$ and $\eta_{inj\_QW\_at\_th}$.

The above-threshold current injection efficiency of the QW ($\eta_{inj\_QW\_above\_th}$) is the fraction of the I_{SCH} above threshold that recombines in the QW, after the lasing occurs. For the above-threshold analysis, the expression for η_{inj_QW} is distinctly different from that under below-threshold conditions. The partial clamping of carriers, above threshold, in the QW can be of a result of carrier heating or a variation in the lateral mode profile.

The above-threshold current injection efficiency ($\eta_{inj\_QW\_above\_th}$) can be expressed (Tansu and Mawst, 2005) as

$$\eta_{inj_{QW}above_{th}} = \frac{1 - \Delta_{QW}\left[\frac{1}{\eta_{inj_{QW}at_{th}}} - \beta\left(1 + \frac{\tau_{bw}}{\tau_b}\right)\right]}{1 + \frac{\tau_{bw}}{\tau_b}} \quad [21]$$

where $\eta_{inj\_QW\_at\_th}$ is given by eqn [19] evaluated at laser threshold. Typical unclamping rates for carriers in the QW (Δ_{QW}) are approximately 8–12% (Nagarajan and Bowers, 1993). Note that in the case of full clamping of carriers in the QW, the $\eta_{inj\_QW\_above\_th}$ will reduce to the simple form given by

$$\eta_{inj_{QW}above_{th}} \sim \frac{1}{\left(1 + \frac{\tau_{bw}}{\tau_b}\right)} \quad [22]$$

Note that the thermionic carrier leakage at high temperature plays significant role, especially in reducing the $\eta_{inj\_QW\_at\_th}$ value and increasing the value of $1/\tau_b$, which will in turn lead to a reduction in $\eta_{inj\_QW\_above\_th}$. Using eqns [19] and [21], the values of injection efficiency in the above-threshold and below-threshold regime for a $\lambda \sim 1.2$ (1.3) – μm emitting InGaAs (InGaAsN) QW with GaAs SCH are plotted in **Figure 6** as a function of temperature. The measured injection efficiency from CLA is compared to the simulated above-threshold values.

The current injection efficiency of a QW laser is significantly affected by the carrier transport in the SCH region. Very large SCH regions, found in broad waveguide laser structures, can lead to reduced current injection efficiency due to the interplay between carrier transport in the SCH and carrier escape from the QW (Knauer *et al.*, 2005). To understand the effects of carrier transport on η_{inj}, a laser structure design consisting of an asymmetrically placed QW can be utilized. A comparison of the injection efficiency of two laser structures for which the active region is intentionally placed close to either the p-cladding or the n-cladding layers has been reported by Yeh *et al.* (2005). This method was also utilized by Nagarajan *et al.* (1992) to demonstrate the impact of QW position on device high-frequency modulation response. Note that the threshold gain condition of the two lasers shown in **Figure 8** is the same (i.e., same optical confinement factor Γ, mirror loss α_m, and internal loss α_i), resulting in nominally identical

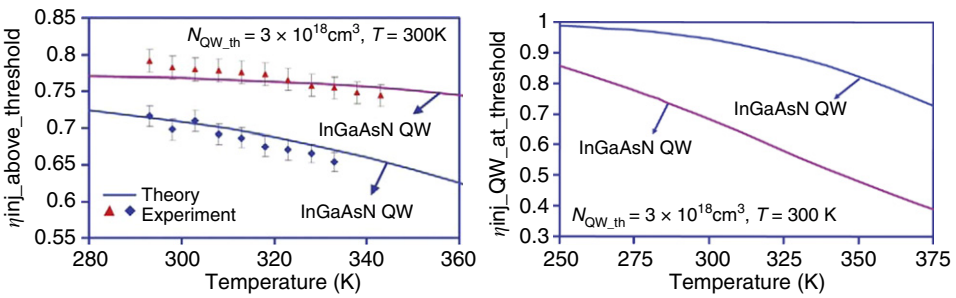

Figure 6 Simulated current injection efficiency for InGaAs(N) quantum-well (QW) lasers in the above- and below-threshold regimes (Yeh *et al.*, 2005).

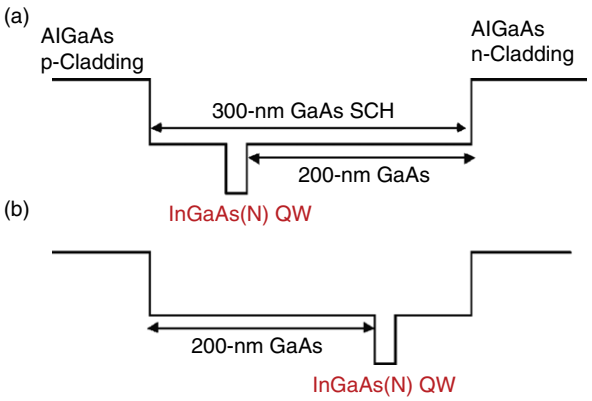

Figure 7 Schematic band diagram of the offset quantum-well (QW) laser structures used to study (Yeh *et al.*, 2005) the impact of carrier transport on the above-threshold current injection efficiency. (a) Laser N has the QW offset to the N-side and (b) laser P has the QW offset to the p-side.

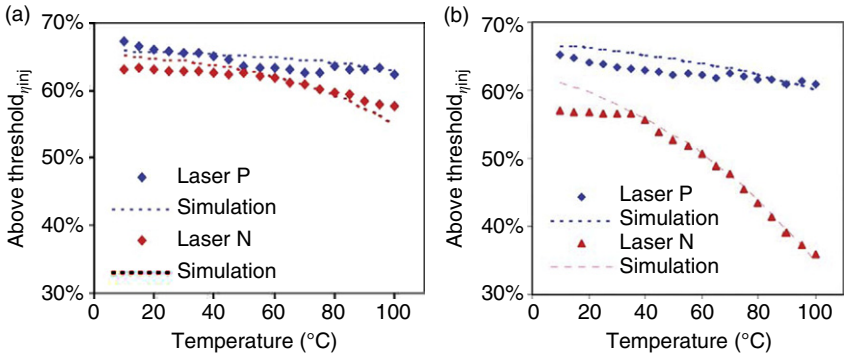

Figure 8 Comparison of measured and simulated above-threshold current injection efficiency for (a) InGaAs quantum-well (QW) and (b) InGaAsN QW lasers structures (Yeh *et al.*, 2005).

values of threshold carrier density N_{th}. However, the carrier transport in the SCH region is altered in the two structure designs. Therefore, the two structures should exhibit similar values of recombination lifetime and thermionic escape lifetime of carriers in the QW. This allows for direct study of carrier transport effects on the device η_{inj} without consideration of carrier recombination and leakage processes.

The measured and simulated (using eqn [21]) above-threshold current injection efficiency for the two laser structures of **Figure 7** are shown in **Figure 8**. It is clear from **Figure 8** that the InGaAsN QW laser behaves very differently as a function of temperature compared with the InGaAs QW laser. A careful examination for the carrier lifetimes of these four major processes is necessary to understand the differences observed in the behavior of the current injection efficiency. To evaluate τ_{QW_total}, a knowledge of the monomolecular, bimolecular, and Auger recombination coefficients A, B, and C, and their temperature dependence is needed. However, for these structures τ_{QW_total} has little effect on the calculated η_{inj} mainly due to a much higher temperature sensitivity of τ_{esc}. The carrier transport behavior in the SCH obeys the ambipolar carrier transport and can be expressed by

$$\tau_{bw} = \frac{1}{2}\left(\frac{L_n^2}{2D_n} + \frac{L_p^2}{2D_p}\right) \quad [23]$$

where L_n and L_p are the thickness of GaAs SCH measured from the QW edge to n-cladding and p-cladding, respectively. The D_n and D_p are the diffusion coefficients of electrons and holes, respectively, which can be related to carrier mobility by the Einstein relation. Since the undoped GaAs SCH is background n-type ($n \sim 10^{16}\,cm^{-3}$), the majority electron mobility and minority hole mobility are used in this calculation. Due to the significantly smaller value of hole mobility μ_p ($\sim 400\,cm^2\,V^{-1}\,s^{-1}$ at 300 K) compared to electron mobility μ_n ($\sim 9200\,cm^2\,V^{-1}\,s^{-1}$), τ_{bw} is ultimately determined by how fast holes can move across SCH region to QW and electron transport has a minimal effect. The significance of the temperature dependence of the minority hole mobility on η_{inj} should also be noted. The carrier lifetime in the SCH waveguide region, τ_b, is calculated from eqns [24] and [25]

considering carrier recombination in the QW, thermionic escape rate, and carrier transport in the SCH

$$N_B = N_{QW}\left(\frac{1}{\tau_{QW_{total}}} + \frac{1}{\tau_{esc}}\right)\left(\frac{V_{QW}}{V_B}\right)\tau_{bw} \quad [24]$$

$$\tau_b = \frac{1}{A_B + B_B N_B} \quad [25]$$

where N_B is the carrier density, A_B and B_B are the monomolecular and bimolecular recombination coefficients in the SCH, and V_B is the volume of the SCH. For the InGaAsN QW lasers (Yeh *et al.*, 2005), the calculated τ_b of both laser P and N exhibits a monotonically decreasing behavior with temperature, reducing from 9.5×10^{-9} s at 10 °C to 8.2×10^{-9} s at 100 °C for laser P and from 8.6×10^{-9} s at 10 °C to 6.1×10^{-9} s at 100 °C for laser N. The longer τ_b of laser P arises from its smaller τ_{bw} value compared to that of laser N. Moreover, stronger carrier leakage at high temperature leads to an increased N_B and therefore a reduced τ_b. This leads to the strong drop of the above-threshold current injection efficiency with increasing temperature in the InGaAsN QW laser structure with the QW offset to the n-side (laser N).

By contrast, for an InGaAs QWs, the injection efficiencies for laser N and laser P are very similar. This is primarily due to the longer thermionic escape time calculated for the InGaAs QW as a result of stronger hole confinement compared with the InGaAsN QW. Nevertheless, for both InGaAs and InGaAsN QWs, the laser P always possesses a higher efficiency than laser N due to the shorter SCH region thickness on the side near p-cladding layer.

The current injection efficiency and its temperature dependence also have a significant impact on the threshold current density. The total threshold current density (J_{th}) of a QW laser can be expressed as a function of the total recombination current in the QW ($\mathcal{F}_{QW} = qL_z(AN_{th} + BN_{th}^2 + CN_{th}^3)$)divided by the current injection efficiency evaluated at laser threshold ($\eta_{inj\_at\_th}$), that is, $J_{th} = J_{QW}/\eta_{inj\_at\_th}$, where q is the electron charge; L_z is the thickness of the QW; N_{th} is the threshold carrier density in the QW; and A, B, and C are the monomolecular, bimolecular, and Auger recombination coefficients in the QW, respectively. Thus, the threshold current density of a QW laser will increase significantly at high temperature if the current injection efficiency decreases significantly with temperature, independently of the existence or absence of Auger recombination in the QW. Therefore, the temperature dependence of the injection efficiency can also lead to ambiguity in determining the dominant recombination mechanism occurring in a QW. One method used to identify the influence of the A, B, and C coefficients on QW laser recombination is the Z-parameter analysis (Sweeney *et al.*, 1998), in which the threshold current is assumed to vary as proportional to n^z. Identification of the value of Z may provide insights into which recombination mechanism dominates over a given temperature range. However, care must be taken to account for the possible temperature dependence of the current injection efficiency, which may result in an effectively larger Z parameter. Another important consequence of the temperature dependence of the injection efficiency is that the differential gain of the QW active region may be reduced at high temperature, since the differential gain is proportional to the square root of the injection efficiency (Coldren, 1995).

2.5 Optical Gain and Radiative Efficiency

For QW structures, the optical gain will depend on the overlap of the QW active region and the optical field of the waveguide mode, since it is the electric field of the mode that ultimately generates the gain through the stimulated emission process. It is common to characterize an active region by material gain g_m which is related to modal gain g by

$$g = \Gamma g_m \quad [26]$$

where Γ is optical confinement factor. If the active region is a planar QW of width, d, then $\Gamma = \Gamma_z$ and for the TE mode with Γ_z is given by

$$\phi_z = \frac{\int_{-d/2}^{d/2} E_y^2 dz}{\int_{-\infty}^{\infty} E_y^2 dz} \quad [27]$$

where (x,y) defines the plane of the QW and the z-direction is perpendicular (transverse) to the QW plane. Gain measurements yield the modal gain; thus, insight into the actual material gain requires knowledge of the modal properties of the waveguide. One of the most commonly used methods of active media characterization is the so-called CLA. This characterization method is based on two fundamental points of laser physics:

(1) Above laser threshold the gain saturates at the value equal to the total loss, α_{tot}, which is equal to a sum of the internal loss and the mirror loss, $\alpha_{tot} = \alpha_i + \alpha_m$.

(2) Above threshold the laser is a converter of injected electrons into photons in the lasing mode with an internal efficiency equal to the current injection efficiency, η_{inj}.

Because of the short stimulated emission lifetime, all injected electrons and holes recombine radiatively above laser threshold. Thus, nonradiative recombination within the QW does not impact the external DQE of the device; it only increases the threshold current density. The number of photons emitted out of the laser, for two facets, is then proportional to α_m/α_{tot}.

Through repeated measurements of devices with varying cavity lengths (i.e., varying mirror loss), the saturated (threshold) gain is obtained as a function of threshold current density. Thus, we can then construct the $g(J)$ characteristic of the QW structure. However, note that only the peak gain as a function of current density is obtained. Note that no information on the spectral dependence of the optical gain is obtained from this measurement. Furthermore, if the active layer under study does not provide enough gain to reach laser threshold, then no information is obtained from the CLA.

2.5.1 Hakki–Paoli method

The modal gain, g, is a function of frequency and injection current density, J. In addition, a modal loss α_i is assumed to be present, typically due to free carrier absorption and waveguide imperfections. The single-pass modal gain, g, results from the gain or absorption due to transitions in resonance with the mode ν under consideration. In a QW amplifier, when a photon seed travels a distance L, its power will be amplified by the factor given by

$$G_1 = \exp[(g - \alpha_i)L] \quad [28]$$

In a Fabry–Perot (FP) amplifier, the electroluminescence (EL) spectrum oscillates with the periodicity of the FP resonances of the cavity. These resonances give rise to a modulation of the intensity in the EL spectrum. If a device is sufficiently short so that the individual FP resonances can be resolved by spectrometer (typically around 300 μm for near-IR devices), it is possible to extract the single-pass gain directly from the EL spectrum. This is done within the Hakki–Paoli approximation considering the intensity maximum of the Nth FP resonance and the adjacent intensity minimum (Hakki and Paoli, 1975). Introducing the notation $R^2 = R1R2$, where $R1$ and $R2$ are the mirror reflectivities for intensity, the ratio of the measured intensity maximum and minimum is given by

$$\frac{I_{N\max}}{I_{N\min}} = \left(\frac{1 + |RG_1|}{1 - |RG_1|}\right)^2 = r_i \quad [29]$$

Solving for G_1 when $0 < RG_1 < 1$, we obtain

$$G_1 = \frac{1}{R}\left(\frac{r_i^{1/2} - 1}{r_i^{1/2} + 1}\right) \quad [30]$$

Thus, a measurement of r_i yields the single-pass modal gain, g, through eqn [28]. Some of the challenges associated with Hakki–Paoli method include the need for a high-resolution spectral measurement. The finite spectral instrument response function will reduce modulation depth of FP resonances and hence the accuracy of extracted gain. A refinement of Hakki–Paoli technique addressing this issue was introduced by Cassidy (1984). Another restriction is that the method is most easily applied to narrow ridge-waveguide structure, which supports a single lateral mode. By contrast, in a broad-area laser, multiple lateral modes may obscure the true modulation depth of the fundamental mode. However, these difficulties can be overcome by special far-field spatial filtering techniques (Bossert and Gallant, 1996). Furthermore, the measurement technique will only be valid up to drive currents below laser threshold. Barring these restrictions, the Hakki–Paoli method is efficient in a sense that from one acquired EL spectrum we derive one gain spectrum. This is in contrast to other single-pass techniques discussed below, where multiple spectra for different lengths, L, of active segment are required for extraction of one gain spectrum.

The spectral (net) gain characteristics of highly strained InGaAs QW and InGaAsN QW ridge-waveguide lasers measured using the Hakki–Paoli method are shown in **Figure 9** (Shterengas *et al.*, 2004). Measurements are performed under pulsed operation to avoid heating effects associated with CW operation. These data reveal that the peak gain as a function of injected current of the InGaAsN QW laser has a dg/dI which is 4 times lower than that of the InGaAs QW laser. This peak gain behavior with current density of InGaAsN QW lasers is also consistent with that observed from CLA. Since the mirror losses ($\alpha_m \sim 22\ cm^{-1}$) can be estimated from the known cavity length and facet reflectance, the internal loss is extracted at low energy limit of the net gain.

2.5.2 Single-pass gain and radiative efficiency measurements

Traveling wave amplifiers (i.e., $R1 = R2 = 0$) can also be utilized to extract the single-pass optical gain. In addition, extraction of the radiative efficiency can be easily obtained, as discussed below. In single-pass measurements, care should be taken to minimize possible round-trip feedback. This can be achieved by combination of methods: leaving a large absorbing, unpumped segment at one end of the device, defining the back facet by scratching through the epitaxial layer to destroy mirror reflectivity, and applying an antireflection coating on the front facet. Shaklee and Leheny (1971) and Bakker and Acket (1977) used optical pumping and

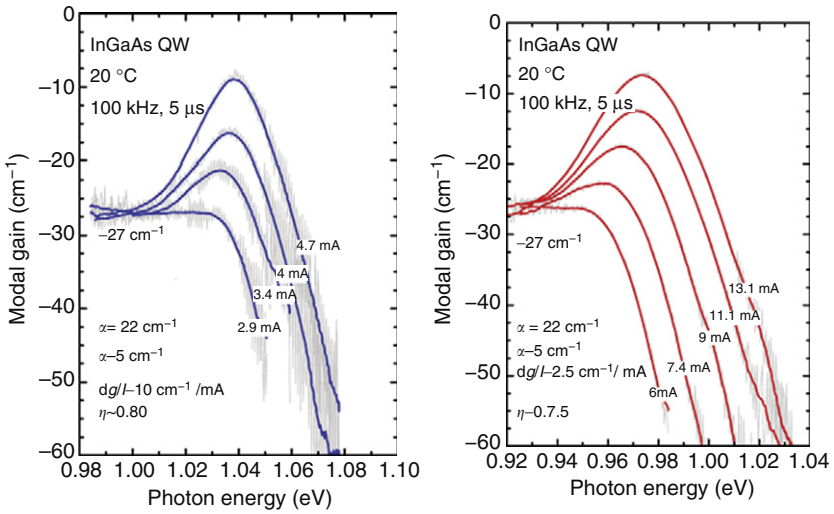

Figure 9 Spectral gain characteristics as a function of current injection for InGaAs quantum-well (QW) and InGaAsN QW ridge-waveguide lasers measured using the Hakki–Paoli technique (Shterengas *et al.*, 2004).

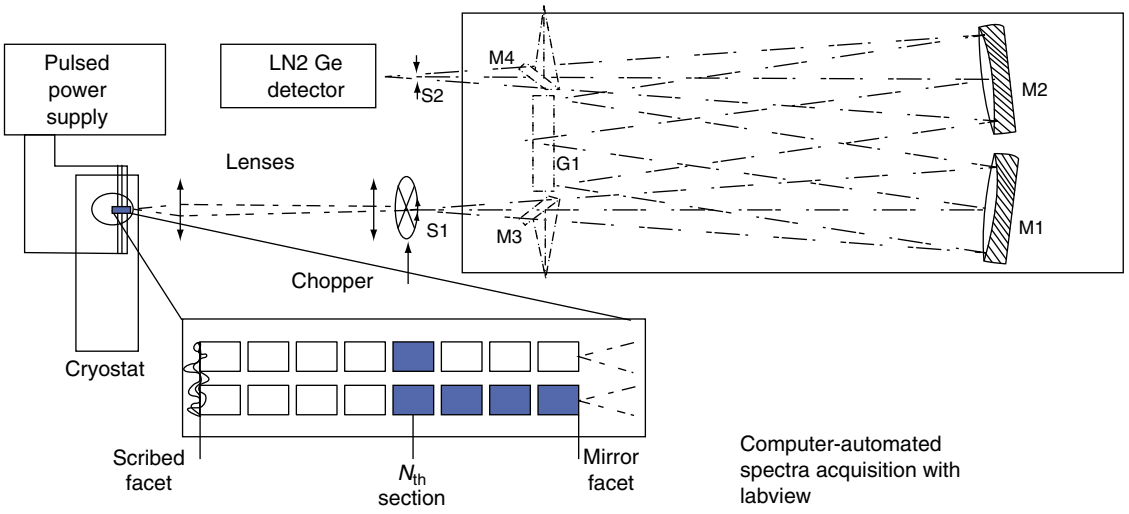

Figure 10 Schematic diagram of the amplified spontaneous emission (ASE) measurement system.

combination of lenses and slits to create a variable-length uniform illumination stripe next to a semiconductor edge. An advantage of the optical pumping setup is that it does not require device fabrication. Thus, a material can be characterized quickly. However, the challenges are to achieve controlled uniform illumination of sufficient intensity and make it stable for the duration of an experiment. Uniform and controlled pumping levels are more easily achieved with electrically injected devices, which were reported by Oster *et al.* (1997) using variable length devices and by Thomson *et al.* (1999) using electrically isolated segments to vary the length of a pumped segment. The multisegmented device approach lends itself better to automation because it avoids any mechanical movements when varying the length of a pumped segment. However, the use of variable length devices avoids issues related to current spreading between segments and the introduction of additional optical losses from the electrical isolation regions. Single-pass techniques are based on the assumption of uniform gain, g, uniform injection level or quasi-Fermi-level, V, and uniform spontaneous emission, R_{sp}, over the length of the pumped segment. This is expected to hold true at low injection levels but will break down at sufficiently high pumping and gain levels. At sufficiently high injection, lasing may occur in one of the filaments and nonlinear effects, such as gain saturation, may set in.

In a multisegment device measurement, for each current density, amplified spontaneous emission (ASE) spectra are recorded corresponding to the total length, N^*L (L=segment length), of the pumped segments, $N=1, 2, \ldots$. A schematic diagram of the ASE measurement system is shown in **Figure 10**.

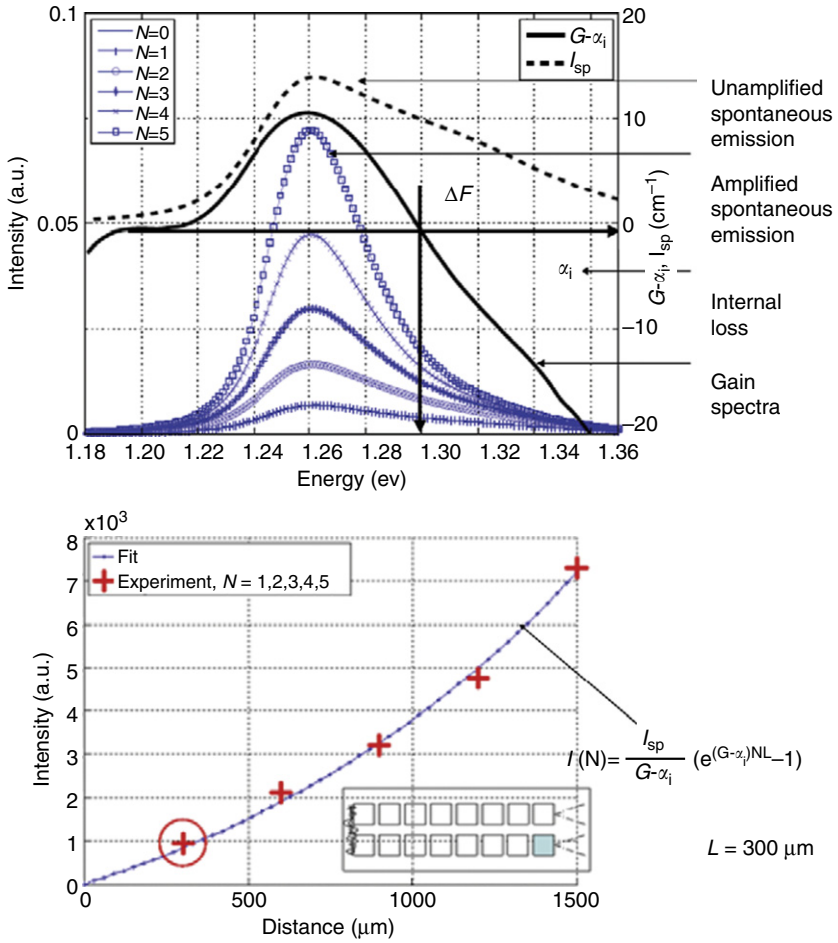

Figure 11 ASE measurement for a five-segment InGaAs quantum-well (QW) laser (Tsvid *et al.*, 2007).

The result of a typical ASE measurement at RT is shown in **Figure 11** for an InGaAs QW laser structure similar to that described by Mawst *et al.* (1996). The ASE spectra can be fitted to eqn [31] at each wavelength

$$I(L) = \frac{I_{sp}}{G - \alpha_i}\left(e^{(G-\alpha_i)L} - 1\right) \qquad [31]$$

This allows for extraction of the $g(h\nu) = G(h\nu) - \alpha_i$ and the $I_{sp}(h\nu)$ spectra as shown in **Figures 11(a)** and **11(b)**. $G(h\nu)$ is the modal gain (absorption) due to electron–hole pair recombination (generation) at the energy $G(h\nu)$ in tune with the mode, and $I_{sp}(h\nu)$ is the spontaneous emission intensity into the mode per unit path length. All optical losses are lumped into the value of α_i. The internal loss, α_i, is considered to be a function of current but not of wavelength.

The spontaneous emission, $I_{sp}(h\nu)$, is extracted from the fit in the units of arb cm^{-1} and can be calibrated in real units of cm^{-1} using fundamental relationship, eqn [32], between gain and spontaneous emission (Henry *et al.*, 1980):

$$R_{sp}(h\nu) = \frac{G_m(h\nu)}{\left[1 - \exp\left(\frac{h\nu - \Delta F}{kT}\right)\right]} \qquad [32]$$

The subscript, m, indicates that the gain is taken in the bulk material sense: $G_m(h\nu) = G(h\nu)/\Gamma$, where confinement factor Γ is calculated from refractive indexes and layer thicknesses. Extraction of the quasi-Fermi-level separation, ΔF, is shown in **Figure 12**, as the energy at which $G(h\nu) = 0$. T is the temperature and K is Boltzmann constant. Equation [32] is valid in the vicinity of the gain maximum. From the ASE fit to eqn [31], we know $R_{sp}(h\nu)$ within a constant factor. Thus, we use eqn [32] at the gain maximum to find the scaling factor and calibrated spontaneous emission $R_{sp}(h\nu)$ in units of cm^{-1} into the mode.

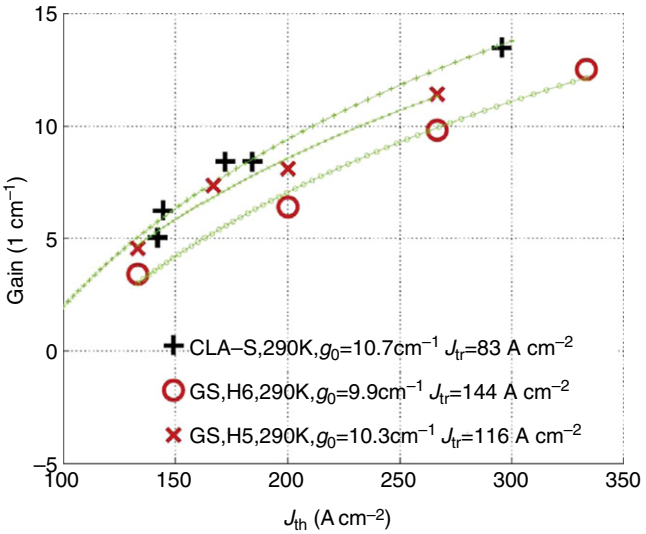

Figure 12 Comparison of peak optical gain vs. current density as determined from both conventional cavity-length analysis (CLA) and multisegment amplified spontaneous emission (ASE) gain-segmented (GS) measurements (Tsvid *et al.*, 2007).

To find the overall spontaneous emission current, $R_{sp}(h\nu)$ is multiplied by the density of modes and integrated over 4π solid angle and all frequencies, V, which gives

$$\mathcal{F}_{sp} = \int \frac{eR_{sp}(h\nu)L_z 8\pi n^2 d\nu}{\lambda^2} (\text{A cm}^{-2}) \quad [33]$$

Here e is electron charge, L_z is active media thickness, and n is the active medium refractive index. Note that the nonradiative current is simply the difference between the total current density measured at the contact and the overall spontaneous current, $\mathcal{F}_{tot} - \mathcal{F}_{sp}$. Defined as such, nonradiative current is a quantity directly accessible by the experiment, although it is a property not only of material but also of the laser structure (i.e., injection efficiency). Finally, the ASE measurement and extraction of all quantities can be repeated for several current densities to extract gain–current relationship.

2.5.3 Experimental gain studies of strained InGaAs QWs

Single-pass gain and radiative efficiency studies on InGaAs QW lasers with varying QW strain reveal insight into the radiative processes in the frequently used material systems. As a baseline, consider the conventional 0.98-μm-emitting aluminum-free laser structures that employ a single 8.5-nm-thick $In_{0.2}Ga_{0.8}As$ QW with 1.62-eV InGaAsP barriers and waveguide and InGaP cladding layers, similar to that described by Mawst *et al.* (1996). From the measured gain spectra, the peak gain as a function of current density can be compared with the values extracted from a conventional CLA. These gain–current curves are fitted to a phenomenological dependence:

$$G_{m,max} = g_0 \ln(\mathcal{F}_{tot}/\mathcal{F}_{tr}) \quad [34]$$

$G_{m,max}$ denotes material gain spectra maximum (DeTemple and Herzinger, 1993; McIlroy *et al.*, 1985; Whiteaway *et al.*, 1991), and comparison in terms of parameters g_0 and $\mathcal{F}_{tr}$ is shown in **Figure 12**. From this comparison, we see that CLA measurements on segmented lasers yield g_0 and $\mathcal{F}_{tr}$ values in reasonable agreement (within $\sim$20%) with the ASE measurements.

The properties of the 0.98-μm-emitting InGaAs QW can be compared with those of a higher strain 1.2-μm-emitting InGaAs QW (Tansu *et al.*, 2001) with an active region that consists of a 6-nm-thick $In_{0.4}Ga_{0.6}As$ QW ($\Delta a/a \sim 2.5\%$) with a GaAs waveguide and $Al_{0.7}Ga_{0.3}As$ cladding layers. The prominent differences of the highly strained QW material are a larger gain parameter, J_0, and a lower transparency current density, J_{tr}, as shown in **Figure 13**. The lower transparency current density is attributed to the beneficial effect of strain on the energy bandstructure, through equalization of conduction and valence band DOS (Adams, 1986; Yablonovitch and Kane, 1986; Coldren, 1995). The CS reduces the DOS, which is expected to lead to a reduction in the J_0 value. However, other factors, such as differences in QW width and emission wavelength, also influence the value of J_0, as discussed for the gain maximum in Section 2.1, and may account for the increase observed in the 1.2 – μm θ emitting InGaAs QW (d_{QW}=6 nm) compared with that of the 0.98-μm θ emitting InGaAs QW (d_{QW}=8.5 nm).

Since the ASE measurement allows us to extract the spontaneous emission spectra, which can then be integrated to obtain the radiative current density, the peak material gain can also be plotted against the radiative current density, as shown in **Figure 14**.

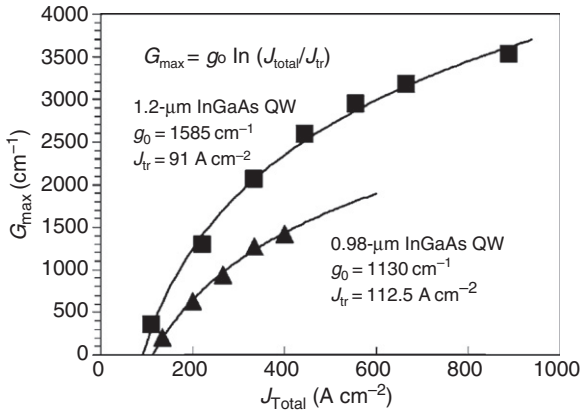

Figure 13 Comparison of peak optical gain (from amplified spontaneous emission (ASE) measurements) vs, total injection current for $In_xGa_{1-x}As$ quantum-well (QW) lasers emitting at 1.2 and 0.98 μm (x=0.4 and 0.2, respectively) (Tsvid *et al.*, 2007).

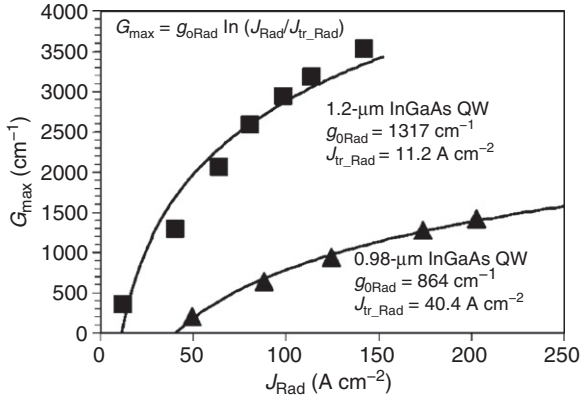

Figure 14 Comparison of peak optical gain (from amplified spontaneous emission (ASE) measurements) vs. radiative current for $In_xGa_{1-x}As$ quantum-well (QW) lasers emitting at 1.2 and 0.98 μm (x=0.4 and 0.2, respectively) (Tsvid *et al.*, 2007).

Note that the radiative transparency current density for the highly strained InGaAs QW is extremely low, $J_{tr\_rad} = 11.2\ A\ cm^{-2}$, indicating that significant improvement in device performance is possible if nonradiative recombination can be further reduced. Comparing the radiative current density to the total current density, the ratio yields the radiative efficiency of the structure, as shown in **Figure 15**, for the two InGaAs QWs. Interestingly, the radiative efficiency of the 0.98-μm-emitting QW is near 50%, indicating that a relatively large fraction of the injected current does not contribute to optical gain (Tsvid *et al.*, 2007).

Note that to obtain information on the radiative efficiency or internal spontaneous radiative efficiency of the QW, we must take into account that a fraction of the injected current may not recombine within the QW (i.e., the current injection efficiency is <1). If the current injection efficiency below-laser threshold is $\eta_{injbelow}$, then the spontaneous radiative efficiency per injected electron is greater than the ratio of the internal radiative current to the total external injected current obtained directly from the ASE experiments by the factor of $1/\eta_{injbelow}$. Note that the value of η_{inj_below} is structure dependent and, in general, difficult to determine.

2.6 Device Temperature Sensitivity

The temperature dependence of the threshold current density (defined by T_0) and the external DQE (defined by T_1) empirically follows the known eqns [35] and [36]:

$$\mathcal{F}_{th}(T) = \mathcal{F}_{tho} e^{(T/T_0)} \quad [35]$$

$$\eta_d(T) = \eta_{do} e^{-(T/T_1)} \quad [36]$$

Since eqns [35] and [36] are empirical, many physical mechanisms contribute to the device temperature sensitivity and play a role in determining the T_0 and T_1 values. In order to help elucidate the dominant physical mechanisms that impact the

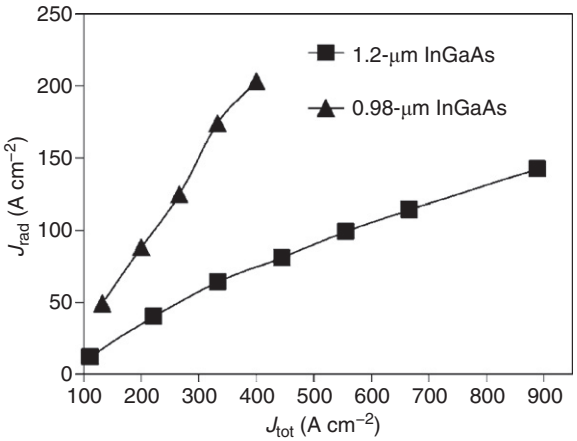

Figure 15 Radiative current density, extracted from amplified spontaneous emission (ASE) measurements, vs. total injection current for $In_xGa_{1-x}As$ quantum-well (QW) lasers emitting at 1.2 and 0.98 μm (x=0.4 and 0.2, respectively). The slope of each line corresponds to the radiative efficiency (Tsvid *et al.*, 2007).

temperature sensitivity of a QW laser, the temperature dependence of the transparency current density, J_{tr}, the above-threshold current injection efficiency, η_{inj}, the internal loss, α_i, and the material gain parameter, $g_{0\,J}$, can be extracted from a series of temperature-dependent CLA (L). By deducing the slope and intercept of the $1/\eta_d$ versus L data line, one can calculate the laser intrinsic parameters, α_i and η_{inj}

$$\eta_d = \eta_{inj}\frac{\alpha_m(L)}{\alpha_i + \alpha_m(L)} \quad [37]$$

where $\alpha_m(L) = (1/L) \times \ln(1/R)$ is the mirror loss and R is the facet reflectivity. Moreover, from the logarithmic relation of the optical gain to current density (eqn [34]) and the definition of threshold gain (eqn [38]), $g_{0\,J}$ and J_{tr} can be extracted, assuming the values of α_i, η_{inj}, and α_m to be known quantities

$$g_{th} = g_{oJ}\ln\left(\frac{\eta_{inj}\mathcal{F}_{th}}{\mathcal{F}_{tr}}\right) = \alpha_i + \alpha_m \quad [38]$$

Note that the η_{inj} value in eqn [37] corresponds to the above-threshold value of the injection efficiency, while the η_{inj} value in eqn [38] corresponds to the at-threshold value. However, in practice, the above-threshold current injection efficiency is generally used in eqn [38], since this value can be easily extracted from measurement.

To gain insight into what physical mechanisms have a significant contribution to the T_0 and T_1 values of a specific device structure, the characteristic temperature coefficients, T_0 and T_1, can be expressed in terms of the temperature dependence of the intrinsic device parameters J_{tr}, η_{inj}, g_o, and α_i (DeTemple and Herzinger, 1993; Tansu *et al.*, 2002a). The expansions of T_0 and T_1 given by eqns [39] and [40] are derived by assuming that J_{th}, the transparent current density (J_{tr}), and the internal loss (α_i) all exponentially increase with temperature and can be expressed as functions which follow $T_X = (1/X)(dX/dT)$. The external DQE (η_d), the current injection efficiency (η_{inj}), and the material gain parameter ($g_{0\,J}$) all are assumed to decrease exponentially with temperature and can be expressed as functions which follow $T_X = -(1/X)(dX/dT)$. Thus, the temperature dependence of J_{th}, η_d, J_{tr}, η_{inj}, g_o, and α_i is quantified by defining characteristic temperature coefficients T_0, T_1, T_{tr}, $T_{\eta inj}$, T_{go}, and $T_{\alpha i}$, respectively. The characteristic temperature coefficients for each device parameter are determined from the measured device performance as a function of cavity length and temperature, under the assumption that the below-threshold current injection efficiency is approximately equal to the above-threshold current injection efficiency

$$\frac{1}{T_0(L)} = \frac{1}{T_{tr}} + \frac{1}{T_{\eta inj}} + \frac{\alpha_i + \alpha_m(L)}{\Gamma_{goJ}}\frac{1}{T_{goJ}} + \frac{\alpha_i}{\Gamma_{goJ}}\frac{1}{T_{\alpha i}} \quad [39]$$

$$\frac{1}{T_1(L)} = \frac{1}{T_{\eta inj}} + \frac{\alpha_i}{\alpha_i + \alpha_m(L)}\frac{1}{T_{\alpha i}} \quad [40]$$

Note that since the mirror loss is a function of cavity length, the T_0 and T_1 values are also functions of cavity length. These equations accurately predict the experimentally observed behavior of T_0 and T_1, which is that while T_0 increases for longer cavity devices, T_1 decreases for longer cavity devices (Mawst *et al.*, 1995). Note that the values of $T_{\eta inj}$ which appear in eqns [39] and [40]

can, in general, be distinctly different. The $T_{\eta inj}$ value in eqn [39] represents the temperature dependence of the below-threshold current injection efficiency and the $T_{\eta inj}$ value in eqn [40] represents the temperature dependence of the above-threshold current injection efficiency. Thus, the individual terms in eqn [39] can only be determined experimentally under the approximation that the $T_{\eta inj}$ value in eqns [39] and [40] is equal.

A comparison of the cavity-length dependence of T_o and T_1 for an $In_{0.4}Ga_{0.6}As$ and $In_{0.4}Ga_{0.6}$ $As_{0.995}N_{0.005}$ QW active laser is shown in **Figure 18**, with the corresponding experimentally determined values of T_{tr}, $T_{\eta inj}$, T_{go}, and $T_{\alpha i}$, utilized in eqns [39] and [40] indicated as the solid lines (**Figure 16**).

The T_0 and T_1 values of InGaAsN QW lasers are significantly lower than those of InGaAs QW lasers. From an analysis based on eqns [39] and [40], the primary mechanisms for these lower values are due to a higher temperature sensitivity of the current injection efficiency, η_i ($T_{\eta i}$), and the material gain coefficient g_o (T_{go}) for InGaAsN lasers. For long-cavity lengths ($L=2$ mm), the primary term affecting the T_0 value stems from the low value of $T_{\eta i}$. Despite the deeper QW in the InGaAsN structure, the experimentally measured current injection efficiency (η_{inj}) of the InGaAsN QW laser reduces more rapidly with temperature compared to that of the 1200-nm InGaAs QW laser. The reduction in η_{inj} can result from active-layer carrier leakage. The carrier leakage process in InGaAsN QW lasers has been attributed to heavy-hole leakage due to poor active-layer hole confinement (Tansu, 2003b).

The underlying physical mechanisms responsible for the temperature dependence of the J_{tr}, η_{inj}, g_o, and α_i, have been discussed by Tansu and Mawst (2002) for InGaAs QW lasers. However, in general, the combined influence of many different physical mechanisms, such as carrier leakage, Auger recombination, and intervalence band absorption, plays a role in determining the values of T_{tr}, $T_{\eta inj}$, T_{go}, and $T_{\alpha i}$. Note that from eqn [39] the values of T_{tr}, $T_{\eta inj}$, T_{go}, and $T_{\alpha i}$ all play a role in determining the T_0 value; however, the smallest value temperature coefficient will have a dominant impact on T_0. By contrast, the T_1 values, given by eqn [40], are dependent only on the values of $T_{\eta inj}$ and $T_{\alpha i}$. The value of $T_{\eta inj}$ is primarily influenced by active-layer carrier leakage, while $T_{\alpha i}$ is believed to depend on both carrier leakage and intervalence band absorption. Experimental studies (Tansu, 2003a) have confirmed that the increased QW barrier heights in InGaAsN-active devices lead to improved $T_{\eta inj}$ and higher T_1 values. Typically, both $T_{\eta inj}$ and $T_{\alpha i}$ values can be quite high ($\sim$500–1000 K) for near-IR InGaAs/GaAs QW lasers with strong carrier confinement. By contrast, $T_{\eta inj}$ and $T_{\alpha i}$ values are generally quite low ($<$100 K) for longer wavelength ($\sim$1.3 μm) InP-based lasers.

The value of T_{tr} depends on which physical process dominates the recombination (i.e., A, B, or C recombination coefficients), since the temperature dependence of J_{tr} ultimately depends on both the temperature dependence of the transparency carrier density (n_{tr}) and that of the recombination coefficients ($A(T)$, $B(T)$, and $C(T)$). The expected range of values for T_{tr} is illustrated in **Figure 17**. The underlying mechanisms, which influence the value of T_{go}, are less well understood, but they are expected to be

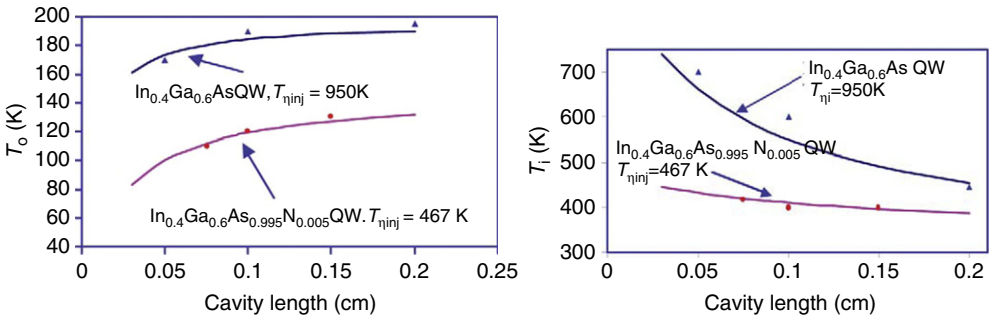

Figure 16 Measured cavity length dependence of T_0 and T_1 for $In_{0.4}Ga_{0.6}As_{0.995}N_{0.005}$ and $In_{0.4}Ga_{0.6}As$ quantum-well (QW) lasers.

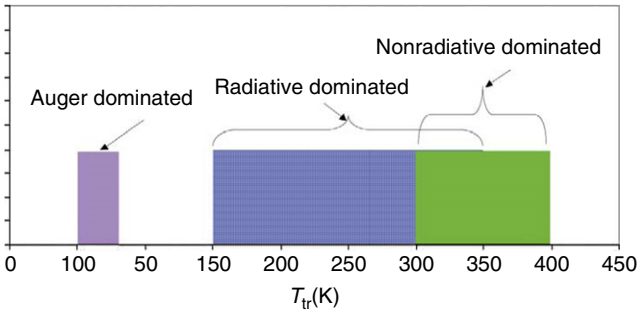

Figure 17 Expected values for the characteristics temperature coefficient for the transparency current density, T_{tr}, for different dominate physical mechanisms (Tansu *et al.*, 2002a).

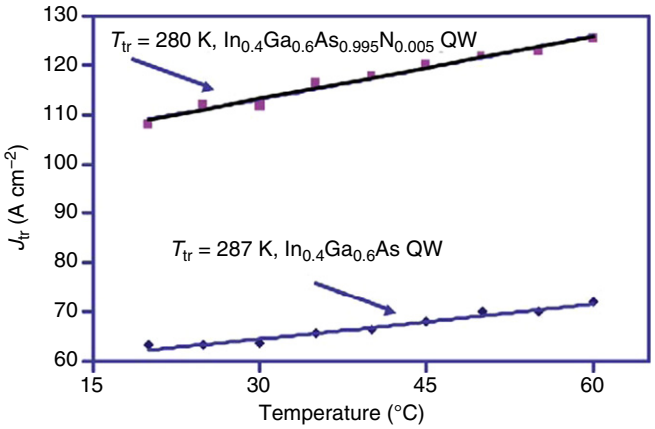

Figure 18 Measured values of the temperature dependence of the transparency current density and corresponding T_{tr} values of $In_{0.4}Ga_{0.6}As_{0.995}N_{0.005}$ and $In_{0.4}Ga_{0.6}As$ quantum-well (QW) lasers. The large T_{tr} value for the $In_{0.4}Ga_{0.6}As_{0.995}N_{0.005}$ QW laser originates from the large monomolecular recombination present in these materials.

influenced by nonradiative recombination. The temperature dependence of the (differential) gain has been implicated as a primary cause for the low T_0 values observed in long-wavelength InP-based lasers (Zou *et al.*, 1993).

The maximum theoretical value of T_0 is predicted to be $T_{0\,max} \sim 300$ K at RT, assuming only radiative recombination in the QW. This value is dictated by the temperature dependence of the radiative recombination, resulting from a temperature-dependent Boltzmann distribution of carriers in the bands (O'Reilly and Silver, 1993). Measurements of the integrated spontaneous emission as a function of temperature confirm these predictions (Braithwaite *et al.*, 1995). However, other more temperature-sensitive physical processes, such as nonradiative recombination or carrier leakage, tend to place a practical upper limit on the T_0 value in actual devices. Near-IR ($\lambda \sim 980$ nm) InGaAs/InGaAsP/GaAs QW lasers generally have strong carrier confinement to the QW and minimal Auger recombination, resulting in T_0 values as large as 250 K (Mawst *et al.*, 1996). By contrast, in longer wavelength ($\lambda \sim 1.3$–1.5 μm) InGaAsP/InP QW lasers, T_0 values are generally much lower ($\sim$40–60 K), which has been attributed to weak carrier confinement (Belenky *et al.*, 1997, 1999), Auger recombination (Braithwaite *et al.*, 1995), and the temperature dependence of the differential gain (Zou *et al.*, 1993). Interestingly, high T_0 values (>200 K) can also occur as a result of temperature-dependent lateral carrier diffusion in narrow ridge-waveguide devices (Adolfsson *et al.*, 2008). For this reason, T_0 values should be evaluated and comparisons are made only from wide-stripe lasers, where current spreading effects are negligible. Furthermore, a large temperature-insensitive defect recombination (i.e., monomolecular nonradiative recombination) can also lead to unusually high T_0 values (Tansu *et al.*, 2002a). This high T_0 reflects the weak temperature dependence of the transparency current density, as shown in **Figure 18**.

3 QW Material Properties

Studies relating the QW interface structure to photoluminescence (PL) spectral characteristics have been reported for GaAs/AlGaAs QWs (Ikuta *et al.*, 1995), InGaAs/GaAs QWs (Hiramoto *et al.*, 1994), and InGaAs/InGaAsP QWs on GaAs (Bhattacharya *et al.*, 1996; Sharma *et al.*, 2002), as well as for InP (Epler *et al.*, 1994) substrates. Interface studies by atomic force microscopy on metal-organic phase epitaxy (MOVPE)-grown InGaAs QW materials have mainly focused on growth mechanisms and few studies have correlated the QW interface structure with semiconductor laser device performance. However, the substrate orientation can play a significant role on the optical characteristics of strained InGaAs QWs, since step bunching can occur on misoriented substrates. SQW-strained InGaAs QWs on Al-free InGaAsP waveguide regions, shown in **Figure 19**, exhibit smooth 2D island growth on nearly exact (100) GaAs substrates (**Figure 20(a)**). By contrast, identical QW structures grown on substrates cut 2° off toward [110] exhibit increased high-frequency surface roughness (**Figure 20(b)**). This surface roughness correlates with increased low temperature (LT) PL linewidth, as well as increased device temperature sensitivity (Mawst *et al.*, 1995). Thus, device structures employing a strained-layer InGaAs QW generally benefit from growth on nearly exact (100) GaAs substrates.

To extend the emission wavelength of the strained $In_xGa_{1-x}As$ QW beyond 1 μm on GaAs substrates, high-indium-content ($x > 0.2$) QWs are necessary. Ultimately, the longest emission wavelength achievable from an InGaAs QW grown on a GaAs substrate is limited by the strain relaxation from the lattice mismatch between the QW layer and the substrate. Larger strain values can be used by reducing the thickness of the QW to avoid strain relaxation. However, quantum size effects in the thinner QW will blue-shift the emission wavelength. Studies have shown improvement in the optical luminescence of the materials grown at reduced temperature, attributed to the reduced strain-induced misfit dislocation of the materials grown at low temperature (Tsao, 1993; Choi *et al.*, 1999). By growing the InGaAs QW at a reduced temperature, the surface energy during the growth is also

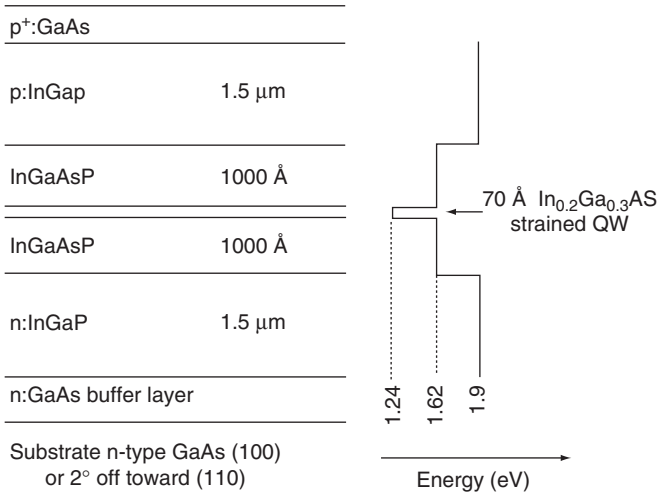

Figure 19 Schematic diagram of the Al-free laser structure with a strained InGaAs quantum-well (QW) employed for QW atomic force microscopy (AFM) and photoluminescence (PL) characterization (Bhattacharya *et al.*, 1996).

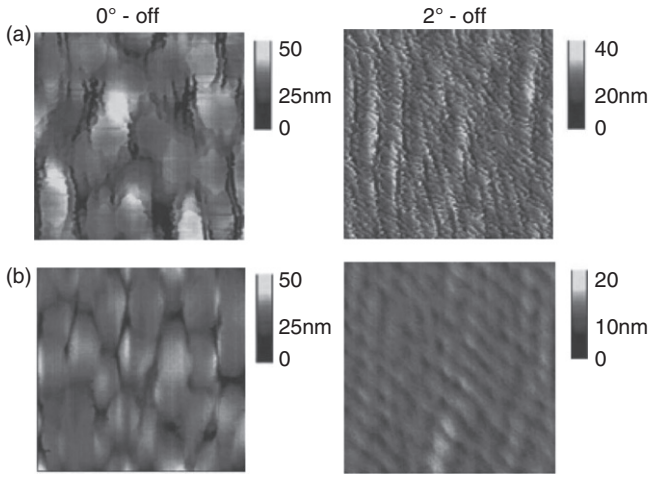

Figure 20 Atomic force microscopy (AFM) images of (a) InGaAs quantum-well (QW) surface and (b) InGaAsP waveguide surface for structures grown on exact (100) GaAs substrates and 2° off toward [110] (Bhattacharya *et al.*, 1996).

lowered compared to the energy to form strain dislocations, which will in turn increase the effective critical thickness of the materials (Ekenstedt *et al.*, 1995; Kim and Lee 1995). The temperature-dependent critical thickness, h_c expressed in Å, as a function of In mole fraction (x) and growth temperature (T), as shown by Ekenstedt *et al.* (1995), for $In_xGa_{1-x}As$ can be expressed as

$$h_c(x,T) = 3.5[x + 7.94 \times 10^{-5}(T - T_r)]^{-2.57} \quad [41]$$

In eqn [41], T_r and T represent the room and substrate temperatures. From eqn [41], we can observe that as the substrate growth temperature decreases, the effective critical thickness of the InGaAs QW increases. By using eqn [41], the calculated predicted critical thickness of an InGaAs QW with 35% In content at a growth temperature of 510 °C is approximately 12–15% larger than that of the InGaAs QW grown at 725–750 °C, which is the typical MOCVD growth temperature for InGaAs QWs. Although the critical thickness value of the InGaAs QW, from eqn [41], is not quantitatively accurate, the equation predicts the trend that by growing the InGaAs QW at a reduced temperature, the critical thickness of the InGaAs QW can be increased. Experimentally, it has also been shown by Ekenstedt *et al.* (1995) that the effective critical thickness of the InGaAs on GaAs is a strong function of substrate temperature during the growth, with lower substrate temperature resulting in larger effective critical thickness. Other techniques to calculate the critical thickness have also been proposed by Schlenker *et al.* (2000). Based on the Schlenker *et al.* (2000) model, for a $In_{0.35}Ga_{0.65}As$ QW, the critical thickness is approximately 83 Å, which is slightly higher than the critical thickness calculated with the People and Bean (1985) model (70 Å).

Another technique to improve the properties of highly strained InGaAs QWs is by the implementation of strain compensation. With the use of tensile-strained GaAsP barriers surrounding the InGaAs QW (Choi *et al.*, 1999; Tansu and Mawst, 2001), we can anticipate two benefits for the QW. The first benefit is associated with the strain compensation, so that the total strain force of the QW and the barriers surrounding the QW will be lowered due to the existence of the tensile barriers. The reduced total strain of the QW and the barriers will lead to an increased effective critical thickness of the InGaAs QW. Strain compensation is particularly important when growing multiple highly strained QWs. The second benefit from strain compensation through the use of $GaAs_yP_{1-y}$ tensile barriers is the higher potential barrier that can be provided by the $GaAs_yP_{1-y}$ barrier to the $In_xGa_{1-x}As$ QW. The larger band offset between the barrier and the QW will lead to reduced carrier leakage out of the QW. Stronger carrier confinement in the QW will also lead to lower temperature sensitivity of the threshold current density and also the external differential efficiency of the diode lasers. For example, strain compensation of a highly strained $In_{0.35}Ga_{0.65}As$ QW grown at low temperature (530 °C) is achieved by having $GaAs_{0.85}P_{0.15}$ tensile ($\Delta a/a = -0.6\%$) barriers surrounding the QW. High-resolution transmission electron microscopy (HR-TEM) measurements allow for a measurement of the thickness of the InGaAs QW and indicate that minimal line dislocations are present. The approximate thickness of the $In_{0.35}Ga_{0.65}As$ QW is 80 Å and agrees well with that expected based on growth rates. The atomic level HR-TEM image, as shown in **Figure 21**, appears to be compositionally more abrupt at the leading edge of the QW compared to the trailing edge. There also appears to be a very slight rotation of the [111] planes in the QW with respect to the surrounding GaAs. This slight rotation may suggest a very small strain accompanying the GaAs in accommodating the highly strained InGaAs lattice. From the HR-TEM studies on such highly strained $In_{0.35}Ga_{0.65}As$ QW, no existence of line dislocations on the $In_{0.35}Ga_{0.65}As$ QW can be identified.

In general, the indium content of the $In_xGa_{1-x}As$ material can be calibrated using HR-X-ray diffraction (XRD) experiments on either a thick relaxed InGaAs layer, as shown in **Figure 22(a)**, or an InGaAs/GaAs SL structure. The composition of the bulk $In_xGa_{1-x}As$ layer is approximately 40% In content, which corresponds to approximately 2.8% CS. By comparison, the InGaAs/GaAs SL structure (shown in **Figure 22(b)**) indicates that the In composition of the QW structure is the same as achieved for bulk material. Thus, lattice-latching effects are not observed for In contents in the 40% composition range.

The typical peak wavelengths of the measured PL spectra of an 80-Å $In_{035}Ga_{0.65}As$ QW and the 60-Å $In_{04}Ga_{0.6}As$ QW, as shown in **Figure 23**, are approximately 1.165 and 1.21 μm, respectively. A reduction of approximately 50% in the peak intensity of the PL of the $In_{0.4}Ga_{0.6}As$ QW, in comparison to that of the $In_{0.35}Ga_{0.65}As$ QW, is also observed. The reduction in the optical luminescence of the higher In content (40%) InGaAs QW may be due to the larger lattice mismatch with the GaAs, compared to that of

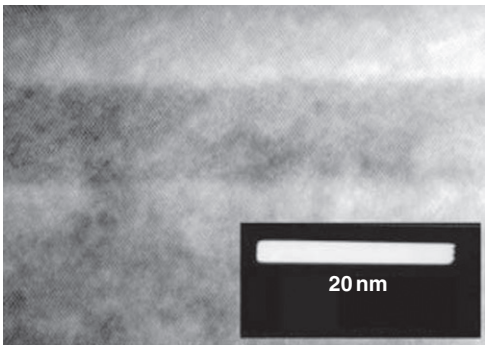

Figure 21 High-resolution transmission electron microscope image of an 80-Å $In_{0.35}Ga_{0.65}As$ QW.

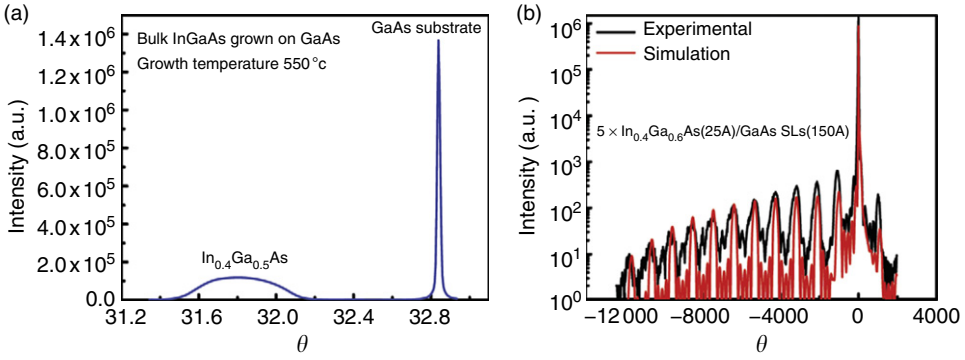

Figure 22 High-resolution (400) X-ray diffraction measurements of low-temperature-grown $In_{0.40}Ga_{0.60}As$: (a) bulk relaxed films and (b) InGaAs/GaAs SL.

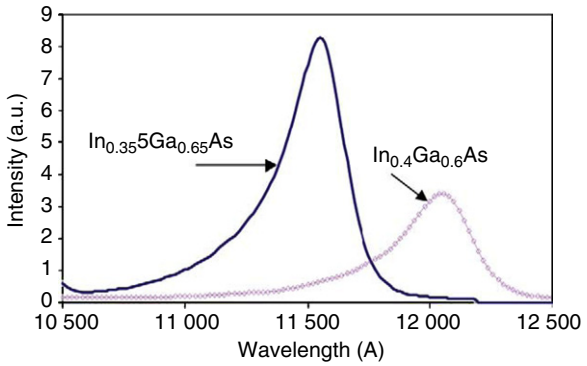

Figure 23 Room temperature photoluminescence of $In_{0.35}Ga_{0.65}As$ quantum-well (QW) and $In_{0.4}Ga_{0.6}As$ QW.

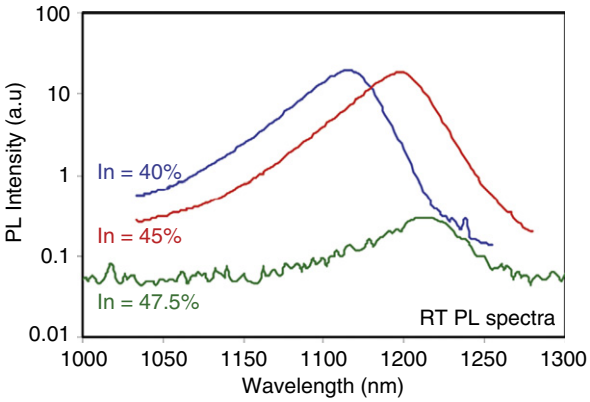

Figure 24 Room temperature photoluminescence (RT PL) emission spectra from InGaAs/GaAs quantum-wells (QWs) as a function of gas-phase In/As ratio.

the 35% In content InGaAs and, possibly, indicates some degree of relaxation. Increasing the In content further leads to a dramatic reduction in PL intensity, presumably due to exceeding the critical thickness. This effect is illustrated in **Figure 24**, where the PL spectra for InGaAs/GaAs QWs are shown as a function of gas-phase In/As ratio.

4 High-Power Near-IR QW Lasers

4.1 High-Power Laser Design Considerations

Single-stripe (100-μm-wide) diode lasers are capable of providing CW spatially incoherent (i.e., multispatial mode) output powers in the 10–25 W range in the near-IR wavelength region (Al-Muhanna *et al.*, 1998; Crump *et al.*, 2009; Gapontsev *et al.*, 2005; Pawlik *et al.*, 2004; Peters *et al.*, 2007; Petrescu-Prahova *et al.*, 2008). However, careful structure design is needed for maintaining reliable operation with high-output-power conversion efficiency. Low power consumption, weak device temperature sensitivity, and reduced facet power density are critical to achieve highest performance under high CW output power operation.

The value of the characteristic temperature coefficient of the external DQE, T_1, has a strong influence on the CW output power and power conversion efficiency (Botez, 1999). The output power is given by

$$P_{\text{out}} = \eta_{\text{d}} \frac{\text{hv}}{q} e^{-\frac{\Delta T_{\text{j}}}{T_1}} (I - I_{\text{th}}) \qquad [42]$$

where η_{d} is the external DQE evaluated at the heatsink temperature, hv/q is the photon energy in electron volts, I_{th} is the threshold current, and ΔT_{j} is the junction temperature rise above the heatsink temperature given by

$$\Delta T_{\text{j}} \approx R_{\text{th}} (\text{IV} - P_{\text{out}}) \qquad [43]$$

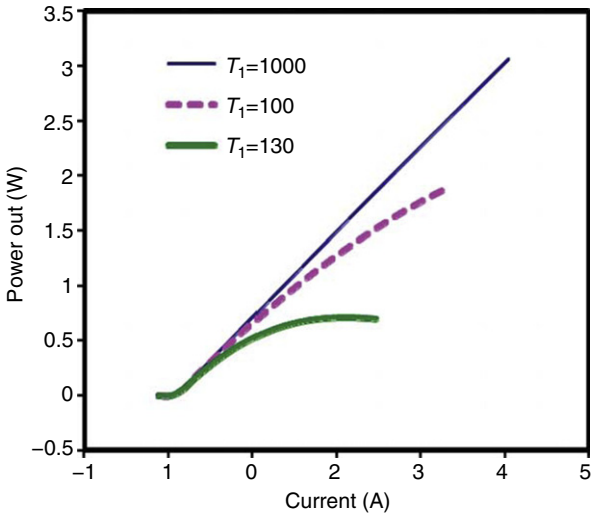

Figure 25 Simulated *P–I* characteristics using eqns [42] and [43] for varying values of T_1.

where R_{th} is the thermal resistance of the diode package and V is the diode operating voltage, which depends on the junction built-in voltage and the series resistance of the device. Since R_{th} is one of the dominant contributors, very low thermal resistance packages are going to be indispensable to test the ultimate output power limits of diode lasers.

At current levels high above laser threshold, the value of I_{th} can be neglected in eqn [42], which indicates that the T_0 value plays a lesser role at high output powers. By contrast, the T_1 value directly impacts the output power and junction temperature rise. A high value of T_1 (>1000 K) is indicative of a very small decrease of η_d with increasing temperature. The impact of T_1 on the CW *P–I* characteristics is illustrated in **Figure 25** using eqns [42] and [43]. Here, a low T_1 value (<100 K) leads to severe output power rollover and high drive currents.

The CW diode laser output power is limited by either the catastrophic optical mirror damage (COMD) or thermal power rollover, depending on which occurs first. Thermally limited power saturation can be avoided by optimizing the laser structure for high power conversion efficiency and weak temperature sensitivity of the threshold current and external DQE (i.e., high T_0 and T_1 values). The internal power density at the laser facet is given by

$$\overline{P}_{int} = \frac{P_{int}\Gamma}{W\,d} = \frac{P_{int}}{W\left(\frac{d}{\Gamma}\right)} \qquad [44]$$

where P_{int} is the internal power at the laser facet, Γ is the transverse optical confinement factor, W is the stripe width, and d is the QW thickness. The value of $\overline{P}_{int}$ at which COMD occurs, referred to as $\overline{P}_{COMD}$, is dependent on the surface recombination velocity of the QW material as well as the local junction temperature rise. The maximum output power density at COMD (Wade *et al.*, 1998) is given by

$$P_{max,cw} = W\left(\frac{d}{\Gamma}\right)\overline{P}_{COMD}\left(\frac{1-R}{1+R}\right) \qquad [45]$$

Note that while $\overline{P}_{COMD}$values are a function of the active layer material (i.e., surface recombination velocity) (Yoo *et al.*, 1991a, b) and facet passivation, they also depend on the other factors which may influence the junction temperature rise, such as diode packaging and heatsinking. Thus, $\overline{P}_{COMD}$values are quite different for devices measured under CW or pulsed conditions. The high surface recombination velocity of AlGaAs leads to low values of $\overline{P}_{COMD}$under CW operation. For example, GaAs-and $Al_xGa_{1-x}As$ ($x=0.07$–0.1) active devices with conventional dielectric facet coatings have been reported with $\overline{P}_{COMD}$ values of 11 and 8–5 MW cm^{-2}, respectively (Garbuzov *et al.*, 1996; Shigihara *et al.*, 1991), under CW conditions. Higher Al content in the active region is expected to further reduce $\overline{P}_{COMD}$ values. The introduction of indium into the active region reduces the surface recombination velocity and improves $\overline{P}_{COMD}$ values. InGaAs QW active lasers exhibit CW $\overline{P}_{COMD}$ values in the range of 20–30 MW cm^{-2}, depending on the efficiency of heat removal (i.e., packaging dependent) (Al-Muhanna *et al.*, 1998; Livshits *et al.*, 2000a, 2000b). In fact, the values of $\overline{P}_{COMD}$ for InGaAs QWs have been reported as high as 40 MW cm^{-2} by the use of active cooling to keep the junction temperature nearly constant over a range of CW operation (Livshits *et al.*, 2000a, b). The use of a nonabsorbing mirror (NAM) increases $\overline{P}_{COMD}$ such that in certain device structures thermal rollover occurs prior to COMD.

Facet degradation in GaAs-based diode lasers remains the primary factor limiting the maximum output power at which reliable operation can be achieved (Henry *et al.*, 1979). Facet degradation is known to be a function of the optical power density at the

facet and the surface recombination velocity of the exposed active region (Yoo *et al.*, 1992). The strain of the active region may also play a role in facet failure, since strain relief at the semiconductor–air interface can lead to enhanced optical absorption at the facet (Valster *et al.*, 1997). Because of the low surface recombination velocity, InP-based devices do not reach COMD during CW operation, and thermal rollover occurs prior to COMD. However, for GaAs-based near-IR and visible emitting devices, COMD values can be rather low and severely impact the maximum CW output powers achievable. In order to reduce the optical power density, high-output-power lasers have been designed to have large optical spot size at the facet. These large-spot-size devices allow higher output power levels to be achieved prior to reaching the COMD power density. However, the complete elimination of facet degradation generally requires complex fabrication steps to produce a high-energy band-gap widow region at the facets, so-called NAMs (Botez and Connolly, 1984; Walker *et al.*, 2002). Other facet passivation methods include using chemical treatments (Yoo *et al.*, 1991a), *in situ* cleave and coat procedures (Chand *et al.*, 1996), deposition of ZnSe on the facet of *ex situ* cleaved devices (Syrbu *et al.*, 1996), or hydrogen irradiation followed by ZnSe passivation (Ressel *et al.*, 2005).

The temperature rise at the facet of a diode laser is generally higher than the temperature rise in the bulk of the diode laser due to the high surface recombination at the semiconductor–air interface. This nonradiative recombination initiates local heating at the facet, leading to a reduction in the energy band gap of the active region at the facet, which in turn results in increased optical absorption near the facet. This feedback cycle leads to a so-called thermal runaway or COMD and, ultimately, melting of the facet near 1240 °C for GaAs (Yoo *et al.*, 1992). Previous studies on facet temperature measurements have found that a critical temperature rise (ΔT_{cr}) occurs at the facet just prior to COMD (Epperlein *et al.*, 1992; Hayakawa *et al.*, 1999a, 1999b). Measurements on AlGaInP-based visible lasers reveal local facet temperature rises of ~120 K prior to COMD. However, the values of ΔT_{cr} exhibit a wide range of values, depending on the materials utilized in the laser structure.

Most studies of COMD have been conducted on narrow-stripe lasers, which generally exhibit a stable spatial distribution of the optical power density across the laser facet. Furthermore, since lateral heat removal is more efficient in a narrow-stripe device (stripe width ~5–10 μm), COMD values are generally much higher compared with wider stripe devices (Hayakawa, 1999b). Multispatial mode, wide-stripe (i.e., broad-area) devices are of interest for many applications needing high output powers (>1-W CW) without a high-beam-quality requirement. However, the facet degradation behavior of CW-operating broad-area lasers is far more complex compared to that of narrow-stripe devices, due to spatial instabilities (i.e., filamentation) of the optical mode. Optical filaments correspond to micron-sized regions of high-power density and lead to localized facet heating (i.e., hot spots) (Lang *et al.*, 1993). Furthermore, the filament formation is generally uncontrollable and may result from nonuniformities within the device itself or at the device heatsink/bonded interface.

The total power conversion efficiency of a diode laser is the ratio of the light output power to the input electrical power and is given by

$$\eta_p = \frac{P_{out}}{IV} \qquad [46]$$

Achieving high power conversion efficiency (η_p) diodes, at high CW output powers, with emission wavelengths >1.3 μm remains a challenge. However, significant progress has been made in realizing high η_p diodes in the near-IR 1-μm wavelength region. A simplified expression for maximum power conversion efficiency, $\eta_{p,\,max}$, of a diode laser is given by (Bour and Rosen, 1989; Botez *et al.*, 1996)

$$\eta_{p,max} \cong \eta_d \frac{V_F}{V_0}\left(1 - 2\sqrt{R_S I_{th}/V_0}\right) \qquad [47]$$

where η_d is the external DQE, V_F is the quasi-Fermi-level difference, V_0 is the overall built-in voltage extrapolated from the high-current regime (where it is approximately linear) back to $I=0$ on the I–V plot, R_s is the series resistance, and I_{th} is the threshold current. Equation [47] is a good approximation as long as $R_s I_{th}/V_0 < 0.02$, which is usually the case. It is apparent from eqn [47] that the key means for improving $\eta_{p,max}$ are maximizing η_{ext}, minimizing V_0, minimizing R_s, and minimizing I_{th}. Through optimization of the carrier leakage, heterojunction voltage deficit, internal losses, and series resistance, InGaAs QW active lasers ($\lambda \sim 980$ nm) have demonstrated $\eta_{p,max}$ values of >70% from both single-element wide-stripe devices and laser bars (Erbert *et al.*, 2006; Kanskar *et al.*, 2005; Knigge *et al.*, 2005; Pikhtin *et al.*, 2004; Pawlik *et al.*, 2007). A 50-W laser bar characteristics exhibiting $\eta_{p,max}=73\%$ is shown in **Figure 26** (Kanskar *et al.*, 2005).

It is important to realize that if η_{ext} is highly temperature dependent, the $\eta_{p,max}$ value will be reduced due to junction heating. Maximizing the value of η_{ext} requires having an injection efficiency near unity and a very low internal loss (α_i). One successful approach for high-power laser structure design has been the broad waveguide (BW) (Al-Muhanna *et al.*, 1998; Garbuzov *et al.*, 1996). An Al-free InGaAs/InGaAsP/InGaP BW structure on GaAs substrate designed for laser emission near 980 nm is shown in **Figure 27**. This BW design has been utilized to achieve CW output powers (~11 W) from broad-stripe 100-μm-wide Al-free diode lasers (Al-Muhanna *et al.*, 1998).

The BW provides for a large value of d/Γ, which is important for reducing the internal optical power density at the laser facet. In addition, such structures generally have very low internal losses ($\alpha_i < 1$ cm^{-1}) since the optical field has very small overlap with the

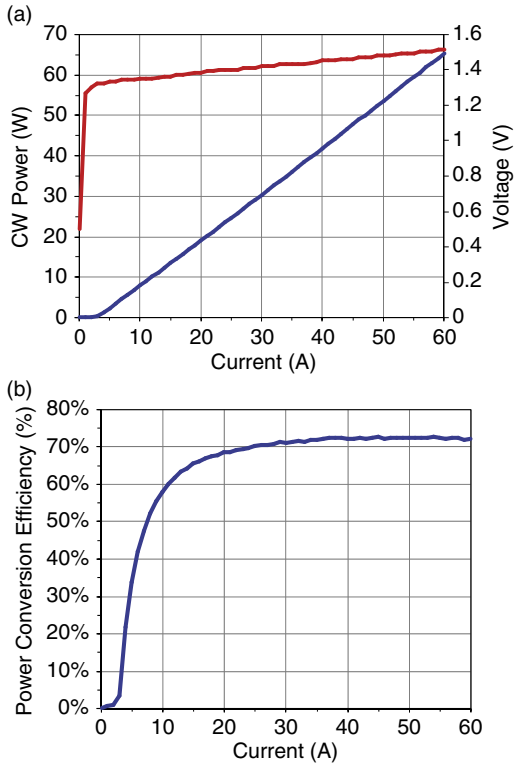

Figure 26 Electrical and optical characteristics of a high-efficiency 980-nm InGaAs quantum-well (QW) diode laser (Kanskar *et al.*, 2005).

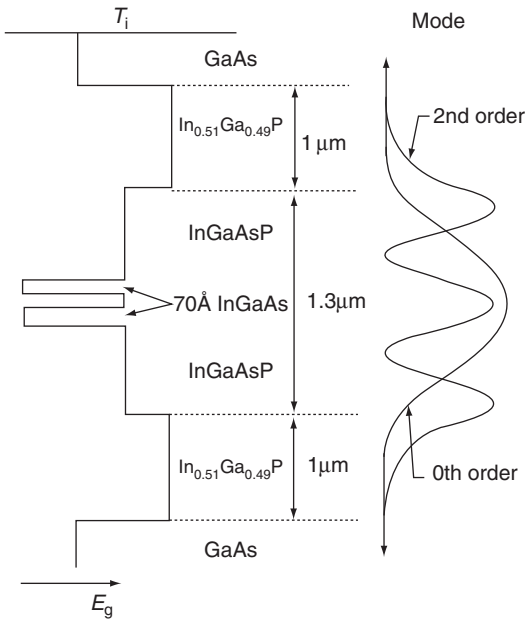

Figure 27 InGaAs quantum-well (QW) broad waveguide laser structure for 980-nm emission (Al-Muhanna *et al.*, 1998).

p- and n-type-doped cladding layers. The variation of d/Γ with waveguide width, W, is shown in **Figure 28**. The lowest threshold current design is indicated by the smallest value of d/Γ, although this corresponds to the smallest equivalent spot size and the highest optical power density. Large W values result in large d/Γ values, that is, the BW design, which leads to lower optical power density.

The small field penetration into the doped cladding layers, as shown **Figure 29(a)**, leads to low internal loss as a result of reduced free carrier absorption. Note that large d/Γ can also be achieved with very small values of W, that is, the narrow waveguide

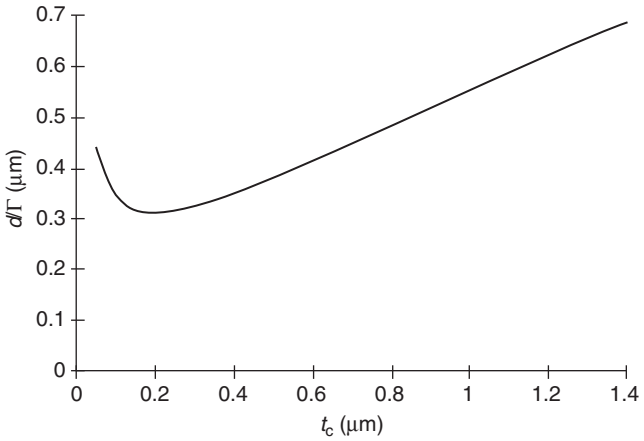

Figure 28 Computed d/Γ values as a function of waveguide width, t_c. Large values of d/Γ correspond to the broad waveguide design and small values of d/Γ correspond to the narrow waveguide design.

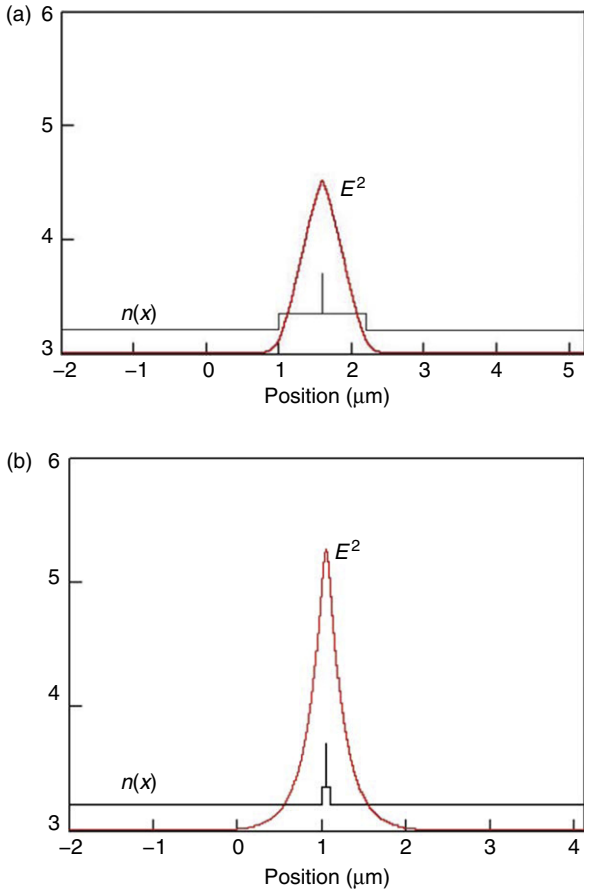

Figure 29 Calculated optical mode intensity for a separate-confining-heterostructure (SCH) waveguide laser structure, similar to that shown in Figure 28, for (a) a broad waveguide (BW) width structure and (b) a narrow waveguide width structure.

design, although the design tolerance is quite small, as can be seen from Figure 28 in the small 'W' regime. Furthermore, in a narrow waveguide design (Figure 29(b)), the optical field penetrates strongly into the doped cladding layers and care must be taken to reduce internal losses through proper grading of the doping profile. Increasing W also leads to the onset of higher order transverse modes supported by the BW structure. However, careful design of metal losses due to optical field penetration into the Au contact regions can be used to suppress lasing of these higher order modes (Al-Muhanna *et al.*, 1998). Another issue that occurs

in BW structures is the impact of carrier leakage on the current injection efficiency. A large d/Γ value will lead to increased carrier leakage, since this is usually achieved using a low Γ value which leads to a higher threshold current density. Multiple QWs can be utilized to offset this and reduce the threshold carrier density per QW. Low injection efficiency ($\eta_{inj} \sim 70\%$) has been observed for very large waveguide $W \sim 2$-μm BW structures (Erbert *et al.*, 2001). Carrier transport in the BW region can also impact the η_{inj} value, particularly in asymmetric waveguide structures (Lee *et al.*, 2003) or InGaAsN QW structures (Yeh *et al.*, 2005) where hole transport plays an important role in determining the carrier collection in the QW. In the case of an asymmetric BW structure, light doping of the waveguide was found to be effective to improve the value of η_{inj} and reduce its temperature dependence (i.e., higher T_1). Another successful approach to produce a large transverse spot size (i.e. large d/Γ) device involves the insertion of a high-index optical trap on the n-side of the structure (Petrescu-Prahova *et al.*, 2008). Such devices have produced 25 W CW output power at 940 nm wavelengths from 100 μm aperture lasers.

4.2 InGaAs QW Lasers (0.88–1.24 μm)

Diode lasers employing compressively strained $In_xGa_{1-x}As$ QWs on GaAs substrates span the wavelength range from $\lambda \sim 0.88$ μm ($x=0$) to approximately $\lambda \sim 1.24$ μm ($x \sim 0.4$). High-power pump laser sources for Er-doped fiber amplifiers and fiber lasers have driven the development of high-performance diode laser sources in the 940–980-nm wavelength region. The benchmark for assessing the high-power performance of these InGaAs QW lasers has been the wide-stripe (usually 100-μm-wide) broad-area device. The optical mode spot size and the device temperature sensitivity play a key role in the high-output-performance properties, as discussed in Section 4.1. BW structures are effective in producing large transverse spot size devices for low optical power density at the laser facet, also discussed in Section 4.1. Both the InGaAs/AlGaAs QW and the Al-free InGaAs/InGaAsP/GaAs QW lasers have achieved CW output powers from single-stripe broad-area lasers in excess of 10 W, with record CW output powers in the 19–21-W range recently reported (Pawlik *et al.*, 2004; Peters *et al.*, 2007). Early studies on Al-free InGaAs QW lasers grown by MOVPE were reported by Ijichi *et al.* (1990) and Groves (1992), and demonstrated the advantages of an Al-free material system for the fabrication of complex index-guided devices (Liau *et al.*, 1992). High-energy band-gap barriers surrounding the QW are effective in reducing active-layer carrier leakage, leading to reduced device temperature sensitivity. The AlGaAs-based material system has great flexibility in choosing barrier materials for optimization of QW carrier confinement. By contrast, the Al-free InGaAsP-based material system is more challenging, since lattice-matched alloys with band-gap energies in the range of $E_g \sim 1.65$–1.75 eV fall within a compositional miscibility gap. The use of GaAs waveguide structures in InGaAs QW lasers emitting in the 940–980-nm wavelength region leads to strong device temperature sensitivity (Gokhale *et al.*, 1997). Therefore, the use of a quaternary InGaAsP material ($E_g \sim 1.5$–1.6 eV) is typically utilized to improve device temperature sensitivity. Studies reported by Hayakawa (1999) demonstrate that the larger bandgap and tensile-strained GaAsP barriers are effective in Al-free lasers (with InGaAsP waveguide layers, $E_g = 1.5$ eV) for reducing QW carrier loss, and this approach has resulted in nearly temperature-independent external DQEs. High-performance InGaAs QW lasers with 1.62-eV InGaAsP/InGaP BW structures demonstrated high output powers, 11-W CW (Al-Muhanna *et al.*, 1998), and high wallplug efficiency, 66% (Botez *et al.*, 1996).

High-performance $In_xGa_{1-x}As$ QW lasers with an emission wavelength near 1200 nm are possible by employing indium contents of $x \sim 0.4$ (Tansu *et al.*, 2003b). A schematic energy band diagram of a 1200-nm laser structure is shown in **Figure 30**, which employs high Al-content $Al_xGa_{1-x}As$ cladding layers. The active region consists of a 60-Å $In_{0.4}Ga_{0.6}As$ QW, sandwiched by barrier regions of 100-Å GaAs on each side. Strain compensation of the active region is provided by the 75-Å $GaAs_{0.85}P_{0.15}$ tensile barriers, which are grown before and after the GaAs barrier regions. The optical confinement factor for the InGaAs QW is calculated as approximately 1.7%. The growths of the active region and the optical confinement regions utilize $[AsH_3]$/III ratio in excess of 100, at a reactor temperature of approximately 530 °C. The n- and p-cladding layers are based on $Al_{0.74}Ga_{0.26}As$ material system, grown at 775 and 640 °C, respectively. Both cladding layers are designed with doping level of approximately

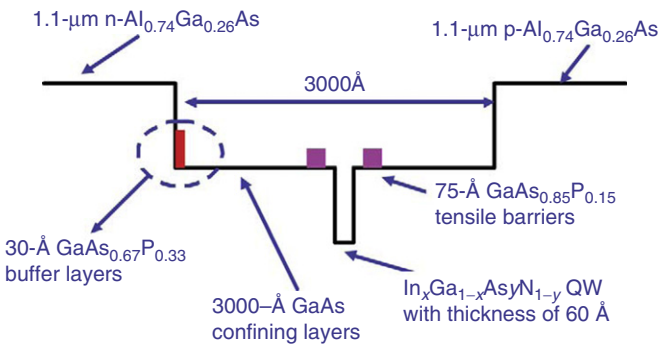

Figure 30 Schematic energy band diagram of an single quantum-well highly strained InGaAs(N) laser structure.

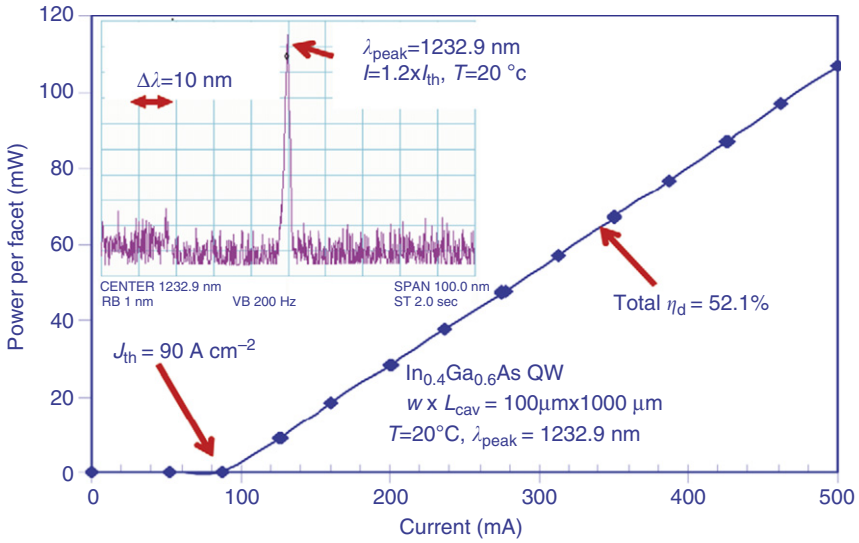

Figure 31 Spectral and output power characteristics of a highly strained InGaAs QW laser (Tansu *et al.*, 2003b).

1×10^{18} cm^{-3}. The tensile buffer layer consists of a 30-Å $GaAs_{0.67}P_{0.33}$, which was found to be crucial for the growth of the highly strained InGaAs(N) QW material system on top of a high Al-content lower cladding layer (Tansu, 2003b).

The pulsed operation RT ($T=20$ °C) lasing characteristics for the 60-Å $In_{0.4}Ga_{0.6}As$ QW broad-area devices (stripe width = 100 μm) with cavity length of 1000 μm are shown in **Figure 31**. The lasing emission wavelengths range from 1216 to 1233 nm, with little variation in threshold current densities (J_{th}). The threshold current densities of these $In_{0.4}Ga_{0.6}As$ QW lasers are found to be 90–92 A cm^{-2} for measurements at a heatsink temperature of 20 °C. The total external DQE (η_d) of the devices is measured as approximately 52%. In the temperature range of 10–50 °C, the slope efficiency (η_d) hardly decreases with temperature, resulting in a T_1 value ($1/T_1 = (-1/\eta_d)d\eta_d/dT$) of approximately 1250 K. The T_0 value ($1/T_0 = (1/J_{th})\,dJ_{th}/dT$) is 140 K. These reasonably high T_0 and T_1 values for $In_{0.4}Ga_{0.6}As$ QW lasers that result in very low-threshold current densities of only 160 and 190 A cm^{-2} are achieved for devices with cavity length of 1000 μm at temperatures of 85 and 100 °C, respectively.

RT threshold current densities of 65 and 100 A cm^{-2} have been reported for $In_{0.35}Ga_{0.65}As$ QW lasers with emission wavelengths of 1170 and 1190 nm, respectively (Tansu *et al.*, 2004). The transparency current densities for the 1170-nm and 1190-nm InGaAs QW lasers were reported as 30 and 58 A cm^{-2}, respectively, at RT (Tansu *et al.*, 2004). A material gain parameter (g_{oJ}) of 1600–1900 cm^{-1} was extracted from CLA for these InGaAs QW lasers (Tansu *et al.*, 2004).

The comparison of the threshold current density (J_{th}) of any QW laser is challenging and at times could be deceptive when comparing various laser structures. The threshold current density of a QW laser depends on many factors, ranging from the quality of the QW active material, the gain properties of the QW, the design of the SCH region, the choice of the compositions and doping levels of the cladding layers, and the modal threshold gain. Nevertheless, the comparison of the device performance in terms of threshold current density is still of importance, as this is generally the parameter of practical interest for laser diodes.

A comparison of the threshold current density for InGaAs QW lasers as a function of wavelength (Sato *et al.*, 1999b; Kondo *et al.*, 2000; Bugge *et al.*, 2001; Tansu *et al.*, 2001, 2004; Mogg *et al.*, 2002; Takeuchi *et al.*, 2002) is shown in **Figure 32**. It is interesting to note that J_{tr} and J_{th} of approximately 30 and 65 A cm^{-2} for the 1170-nm $In_{0.35}Ga_{0.65}As$ QW lasers are comparable with some of the best-reported results realized by quantum-dot (QD) active lasers in this wavelength regime. More recently, low J_{tr} (37 A cm^{-2}) (Chen *et al.*, 2008) and J_{th} values as low as 70 A cm^{-2} (Sundgren *et al.*, 2005) were reported from highly strained InGaAs QW lasers emitting near 1.22 and 1.24 μm, respectively. By comparison, QD lasers with an emission wavelength of 1.15 μm exhibit a J_{th} and J_{tr} of approximately 100 and 20 A cm^{-2}, respectively (Sellin *et al.*, 2001). The transparency current density in QD lasers is smaller as a result of the smaller active volume of the QDs. Although J_{tr} is smaller, the threshold current density of the QD lasers is not significantly lower than that of the QW laser, from the fact that the QD active materials have a low material gain parameter. The relatively low g_o values of the QD active material result from ground-state gain saturation and lead to a modal material gain parameter (Γg_o) of approximately 4.5–9 cm^{-1} per QD stage (Stintz *et al.*, 2000; Smowton *et al.*, 2001), which is significantly lower than that of the typical Γg_o value for an InGaAs QW laser ($\Gamma g_o = 30$–45 cm^{-1} for an InGaAs QW). However, employing long cavity lengths (i.e. low mirror loss), single layer QD active region devices grown by MBE have demonstrated ultra-low threshold current densities at wavelengths near 1.2 μm (Deppe *et al.*, 2009).

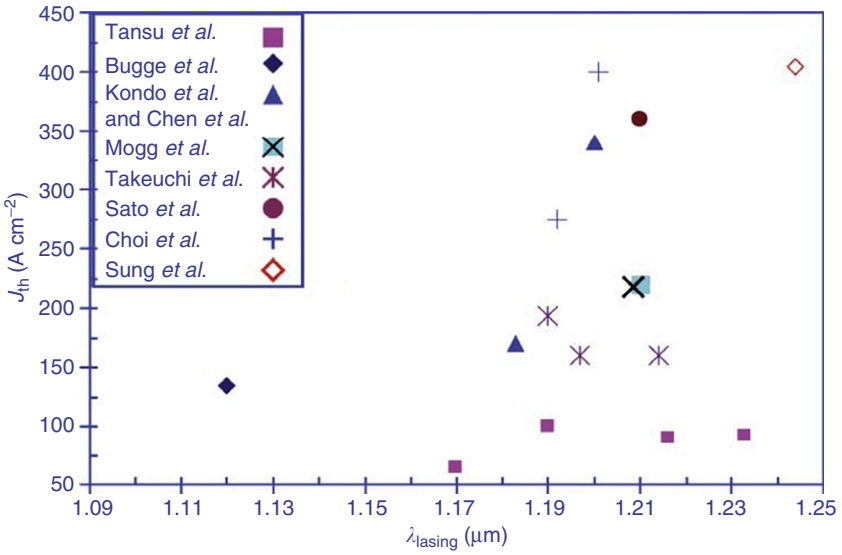

Figure 32 Comparison of threshold current densities as a function of emission wavelength for highly strained quantum-well (QW) lasers.

4.3 Al-Free QW Lasers, GaAsP, InGaAsP QWs ($\lambda \sim 0.7$–$0.85\ \mu m$)

Semiconductor diode lasers with emission wavelengths in the range 700–850 nm, which can operate reliably at high output power levels (multiwatt range), are needed in many applications, such as pump sources for solid-state lasers, sources for high-speed, high-resolution printing, and sources for medical therapy and procedures. Over the past 25 years, significant advances have been made in the development of AlGaAs/GaAs-based lasers operating in the 800-nm-wavelength region. However, the reliability of AlGaAs active layer devices was found to be extremely sensitive to fabrication-induced defects (Waters *et al.*, 1990), bulk defects (Oosenbrug and Latta, 1994) or oxygen impurities introduced during growth (Roberts *et al.*, 1997), and facet passivation (Yonezu *et al.*, 1979). Defects, unintentionally introduced during the fabrication process, propagate to the active region resulting in sudden failures. For reliability at high output powers, sophisticated NAM technology to provide complete facet passivation is required, since the AlGaAs QW active region has a high surface recombination velocity.

Even with complete facet passivation, bulk degradation remains an underlying issue. Bulk degradation can occur due to the motion of crystalline defects into the active region during current injection or from impurities (nonradiative recombination centers) such as oxygen present in the active-layer material. Elimination of the highly reactive aluminum (Al)-containing compounds from the active region (i.e., Al-free active regions) and lattice hardening through the introduction of indium have been effective methods to reduce bulk degradation. Al-free (InGaAsP) active lasers in the near-IR ($\lambda \sim 0.7$–$0.83\ \mu m$) are now in widespread commercial use, primarily due to the high reliability and reduced sensitivity to facet degradation (Diaz *et al.*, 1997).

The use of the InGaAsP/GaAs material system has shown great promise to produce diode lasers in the 700–850-nm-wavelength region without the difficulties associated with the AlGaAs-based devices. Experimental observations of a greatly reduced facet temperature rise for the Al-free structures compared with AlGaAs-based lasers hold promise for improved reliability at high output powers (Garbuzov *et al.*, 1991). Presumably, the lower facet temperature rise is a result of the lower surface recombination velocity and higher thermal conductivity of InGaP compared with AlGaAs. The use of InGaAsP for the QW material, as opposed to AlGaAs, allows for the possibility of introducing strained-layer active regions as a means to reduce threshold currents. In addition, the use of indium in the active region impedes the propagation of dark-line defects (DLDs), thereby eliminating sudden failure (Yellen *et al.*, 1992). Finally, advanced single-mode, index-guided, laser structures generally require multiple growth steps, making the AlGaAs-based material system difficult to use because of the high oxidation rate of AlGaAs (York *et al.*, 1992; Mawst *et al.*, 1998).

InGaAsP QW lasers emitting in the 800-nm region were originally fabricated using liquid-phase epitaxy (LPE) growth (Antonishkis *et al.*, 1988; Garbuzov *et al.*, 1991) and later demonstrated by MOCVD growth (Diaz *et al.*, 1994). These early laser structures demonstrated high output powers for long-cavity-length lasers. However, measurements of threshold current density and DQE as a function of laser cavity length revealed excessive carrier leakage from the active layer, which inhibits achieving performance comparable to AlGaAs-based laser structures. Carrier spillover from the active layer results in large absorption loss ($\alpha_i > 10\ cm^{-1}$) in the optical confinement regions, reducing the efficiency of the device. In order to reduce carrier leakage in such structures, devices have been restricted to long cavity lengths ($L > 1.5$ mm) so as to lower the carrier density at threshold. In addition, relatively large QW widths (15–30 nm) must be utilized so as to minimize the carrier density at lasing threshold. The excessive carrier leakage in the Al-free InGaAsP/GaAs laser structure is a result of the small potential barrier height for electrons ($\Delta E_c = 30 - 50$ meV) between the InGaAsP optical confinement layers and the InGaP cladding layers. By comparison, in

$Al_xGa_{1-x}As$-based laser structures, high-aluminum composition ($x=0.70$) cladding layers provide a large potential barrier for electrons ($\Delta E_c=350$ meV), and carrier leakage becomes significant only in devices with very short-cavity-length devices (i.e., $L<300$ μm). To fully exploit the advantages of the Al-free InGaAsP/GaAs material system for high-power diode lasers, structures that introduce Al-containing compounds (i.e., AlGaAs or AlGaInP) into the SCH regions are required to circumvent carrier leakage problems. Another approach to minimize carrier leakage is to utilize strained-layer InGaAsP QWs to reduce threshold currents, thereby lowering the threshold carrier density.

The growth of InGaAsP lattice-matched to GaAs throughout the band-gap range $E_g=1.42$–1.9 eV is difficult because of the existence of a miscibility gap occurring at typical growth temperatures (650–700 °C), for compositions that fall within the mid-energy gap region (i.e., $E_g=1.65$–1.7 eV) (Onabe, 1982). The existence of a miscibility gap in LPE-grown InGaAsP films has been experimentally verified by low-temperature PL and XRD (Tanaka *et al.*, 1986). Phase separation resulting from the immiscibility is believed to be the cause of significant broadening of the XRD spectra, broadening of the RT PL with a low-energy peak appearing in the low-temperature PL, and poor surface morphology. Similar behavior has been observed in InGaAsP layers grown by MOCVD in the temperature range 650–680 °C, with some improvement in luminescent properties occurring for higher temperature growths (700 °C) (Ohkubo *et al.*, 1994). Furthermore, the extent of immiscibility in strained-layer InGaAsP is unknown at present. Another issue in the growth of InGaAsP is the extent of ordering and its dependence on MOCVD growth conditions. Initial investigations into Al-free InGaAsP/GaAs-based laser structures were carried out by LPE (Brunemeir *et al.*, 1985). A modified sliding boat technique, originally reported by Brunemeir *et al.* (1985), was used to fabricate InGaAsP/GaAs heterojunctions with interface abruptness on the order of the lattice constant.

The use of MOCVD for the growth of Al-free QW laser structures offers the potential for high uniformity over a large substrate area, which is not possible with the LPE growth technique. Al-free 808-nm laser diodes grown by low-pressure MOCVD were first demonstrated by Diaz *et al.* (1994). Laser structures similar to those previously demonstrated by LPE growth were studied. These initial results demonstrated MOCVD as a viable technique for growth of Al-free 808-nm lasers. Later studies demonstrated device performance comparable to that achieved using LPE growth and reported record low electrical (0.03 Ω) and thermal resistance (1 °C W^{-1}). As a result, high-output-power CW operation has been achieved: 1.25 W per facet for long-cavity-length ($L=2.2$ mm) devices with 200-μm emitting apertures (Diaz *et al.*, 1997). However, studies of laser performance as a function of cavity length exhibit similar behavior to that found in earlier LPE-grown devices. Rapid increases in threshold current density and reductions in DQE occur as the cavity lengths are reduced below 1 mm, indicating that severe carrier leakage occurs. Even for cavity lengths of $L=1.2$ mm, threshold current densities are 400 A cm^{-2}, a factor of 1.5–2.0 higher than typical AlGaAs-based devices. These results emphasize the need for improved laser structures with reduced carrier leakage. By employing strained-layer QW active layers and higher bandgap cladding layers, performance competitive with conventional AlGaAs-based laser structures can be obtained with the reliability advantages of the Al-free active material system.

Laser structures employing a lattice-matched InGaAsP QW ($\lambda\sim808$ nm) and AlGaAs (Hayakawa, 1999; Oster *et al.*, 1999) or AlInGaP (Wade *et al.*, 1997) cladding layers have been effective in reducing carrier leakage and reducing device temperature sensitivity. Optimized BW laser structures (Wade *et al.*, 1998) with AlGaInP cladding and InGaP waveguide regions (**Figure 33**) have demonstrated 8.8-W CW from 100-μm-wide stripes with external DQEs of 72%, as shown in **Figure 34**. Structures with $d/\Gamma=0.43$ μm exhibit threshold current densities of 310 A cm^{-2} ($L=1$ mm) and $T_0=120$ K, $T_1=500$ K. COMD power densities of 18 MW cm^{-2} were measured, which is similar to that of InGaAs QW active devices with 980-nm emission.

Tensile-strained InGaAsP or GaAsP QWs can be utilized to access the 0.7–0.8-μm wavelength region (Bour *et al.*, 1994; Sebastian *et al.*, 2001) with TM emission. Large optical cavity (LOC) designs ($d/\Gamma\sim0.8$ μm), employing $Al_xGa_{1-x}As$ (x 0.65) SCH and ($x=0.7$) cladding layers, have demonstrated high CW output powers (8.9 W) from 100-μm wide-stripe devices (Sebastian *et al.*, 2001) emitting at $\lambda\sim0.808$ μm. The high Al-content AlGaAs SCH structure provides good carrier confinement at $\lambda\sim0.808$-μm wavelengths, resulting in T_0, T_1 values of 120 and 746 K, respectively. Higher P-content GaAsP QW active layers (i.e., higher tensile strain) result in emission wavelength as short as 0.715 μm (Erbert *et al.*, 1999). However, poor (hole) carrier confinement leads to excessive carrier leakage at the emission wavelength with T_0 and T_1 values of 60 and 110 K,

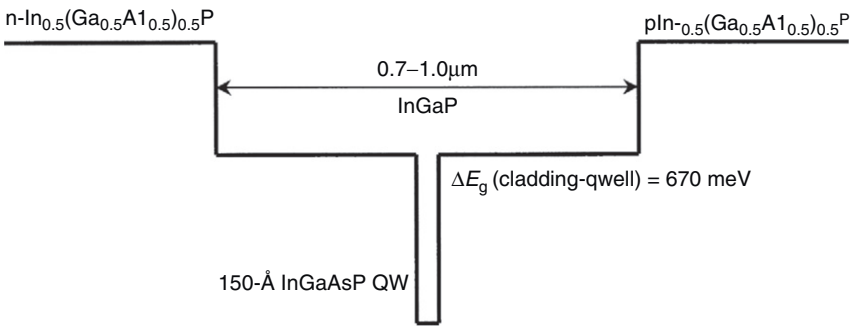

Figure 33 Schematic conduction band diagram of an Al-free active region laser structure emitting near 808 nm.

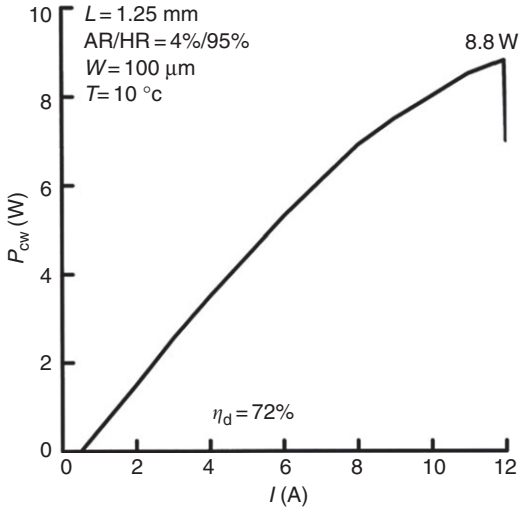

Figure 34 Continuous wave (CW) output power characteristics of a lattice-matched InGaAsP quantum-well (QW) laser emitting near 808-nm wavelength. The device width is 100 μm and the cavity length is 1.25 mm (Wade *et al.*, 1998).

respectively, near $\lambda = 0.735$ μm. However, reliable RT operation at 2-W CW was demonstrated from these Al-free active structures (Sumpf *et al.*, 2001).

Compressively strained InGaAsP QWs with laser emission in the 0.73–0.85-μm-wavelength range have been reported for high-output-power applications. BW designs with $Al_xGa_{1-x}As$ SCH structures have been reported by Oster *et al.* (1999) using a compressively strained ($\Delta a/a \sim 0.5\%$) InGaAsP QW emitting near $\lambda \sim 0.8$ μm. However, a relatively small reduction in threshold current density (5–10%) compared with a lattice-matched InGaAsP QW was observed. Further studies are needed on higher strain values to understand if the benefits of strain can be exploited in this QW material system.

The conventional active region for 850-nm laser diodes is based on the binary (i.e., lattice-matched) GaAs QW active region on a GaAs substrate. The energy band gap of bulk GaAs material system is approximately 1.424 eV, which corresponds to an emission wavelength of approximately 870 nm. By reducing the dimensionality of the GaAs layer to create a GaAs QW structure, emission wavelengths in the 700-nm $< \lambda <$ 870-nm range can be achieved.

For high-modulation-speed (10 Gb s^{-1}) edge-emitting lasers or vertical-cavity surface-emitting lasers (VCSELs), the low differential gain (dg/dn) of the GaAs QW active region results in the requirement to operate at very high injection current, because the square of the modulation bandwidth for QW lasers is proportional to the differential gain and injection current above threshold. Therefore, high-output-power VCSELs, which can maintain single-mode reliable operation, are required for enabling modulation speed well beyond 10 Gb s^{-1}. Unfortunately, the requirement for operating the 850-nm GaAs QW VCSELs devices at high current density to achieve 10 Gb s^{-1} may lead degradation in the long-term reliability issues. Since the coupling of the optical field in VCSELs and the optical gain is dominant only for the TE mode, the VCSEL active region should be designed to have a dominant gain for TE-like polarization. Compressively strained QW active regions are an excellent choice, since the dominant optical gain has TE-like polarization. Comprehensive theoretical analysis by Sale *et al.* (1997) has shown that the use of a compressively strained InGaAsP or InAlGaAs QW active region in VCSELs ($\lambda = 850$ nm) will result in a reduction of the transparency current density and an increase in differential gain compared to those obtainable from lattice-matched GaAs QW VCSELs.

Several methods can be pursued to incorporate CS into the QW active regions at 850 nm. One approach is to utilize narrow, compressively strained ternary InGaAs QWs (Aggerstam *et al.*, 2002). Although the addition of the indium into the QW will decrease the energy band gap of the material, the quantum confinement effect will increase the transitional energy levels in the subbands of the QWs. Some of the advantages of this narrow InGaAs QW approach are the ease in growing the QW, high reliability of this QW, and the ability to incorporate reasonably large strain in the QW. However, the use of narrow QWs results in large carrier leakage from the QW and poor carrier capture efficiency of the QW, leading to highly temperature-sensitive diode lasers.

Another method to achieve compressively strained QWs with an emission wavelength of 850 nm is by using InAlGaAs QWs (Ko *et al.*, 1997). The addition of In decreases the band gap and introduces the compressive strain to the QW. In contrast, the addition of Al will increase the band gap, but keep the lattice constant relatively unchanged. Promising results on 850-nm-VCSELs with compressively strained ($\Delta a/a = 1.5\%$) $In_{0.22}Al_{0.12}Ga_{0.66}As$ QWs have been demonstrated by Ko *et al.* (1997). Although the existence of indium within the InAlGaAs QWs will eliminate DLD propagation, studies on edge-emitting diode lasers have shown the existence of even relatively small Al content ($> 10\%$) in the active regions can potentially lead to bulk degradation (Yellen *et al.*, 1993; Roberts *et al.*, 1998).

An alternate approach is the use of the compressively strained Al-free quaternary InGaAsP QW active region. Studies on InGaAsP active edge-emitting diode lasers have shown them to be highly reliable (Mawst *et al.*, 1999). Lattice-matched InGaAsP

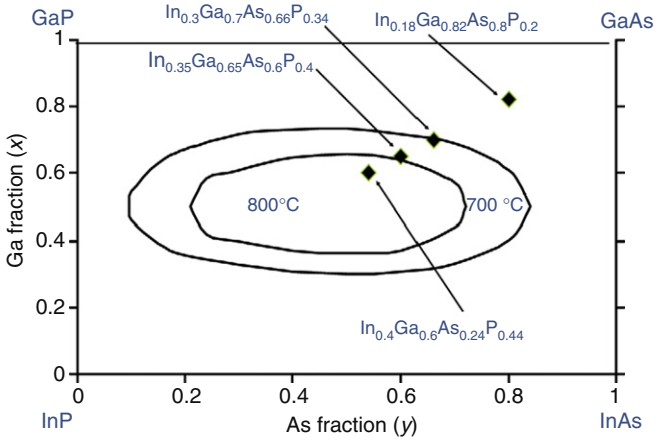

Figure 35 Compositional phase diagram of InGaAsP material systems grown by metal-organic chemical vapor deposition (MOCVD).

active VCSELs emitting at 780 nm have been demonstrated by Schneider and Hagerott-Crawford (1995). The use of an Al-free InGaAsP-based active region is an attractive alternative to the conventional (Al)GaAs active region for IR VCSELs. The InGaAsP material can be engineered for compressively strained QWs with interband transition energies that correspond to an emission wavelength of 850 nm. It has been theoretically predicted by Sale *et al.* (1997) that the use of the compressively strained InGaAsP QWs, with 1.7% CS, in VCSELs (at $\lambda \sim 850$ nm) will result in a reduction of transparency current density and an increase in differential gain compared to the those of conventional GaAs QW VCSELs.

One of the concerns related to the growth of InGaAsP QW material system is related to the existence of the compositional miscibility gap, as shown in **Figure 35**. Quaternary material systems, grown with composition inside the miscibility gap (Stringfellow, 1989), result in phase separation, which in turn will lead to compositional variation across the 2D thin film. As shown in **Figure 35**, the composition of an 850-nm emitting CS $In_{0.18}Ga_{0.82}As_{0.8}P_{0.2}$ QW is located clearly outside of the miscibility gap region for growth temperature of 700 °C, which is a good indication that the QW will exhibit minimal phase separation. The corresponding CS of the $In_{0.18}Ga_{0.82}As_{0.8}P_{0.2}$ QW with respect to the GaAs substrate is approximately 0.6%. An increase in the growth temperature (from 700 to 800 °C) will allow the strain to be increased up to 1.2% CS ($In_{0.35}Ga_{0.65}As_{0.6}P_{0.4}$) and remain outside of miscibility gap, as shown in **Figure 35**.

In order to assess the Al-free CS, 0.85-μm-emitting, active region for high-power applications, an optimized edge-emitting laser structure was reported using the BW design. The strain-compensated active region consists of four pairs of 80-Å compressively strained $In_{0.18}Ga_{0.82}As_{0.8}P_{0.2}$ QW sandwiched by tensile barriers of 100-Å $In_{0.44}Ga_{0.56}P$ barrier layers. Threshold current density of only 255 A cm^{-2} was achieved for devices with cavity length of 2000 μm. High external DQEs, in excess of 61–66%, are achieved for all cavity-length devices. Although a low internal loss is observed ($\alpha_i = 1$ cm^{-1}), the relatively low internal quantum efficiency ($\eta_i = 0.72$) is believed to reflect the interfacial quality of the InGaP/InGaAsP active region. Previously reported threshold current density (J_{th}) and external differential efficiency (η_d) for ($\lambda = 830$ nm) InGaAsP lattice-matched active diode lasers with a BW structure are about 365 A cm^{-2} and 77% (Tansu *et al.*, 2000b).

Proton-implanted CS InGaAsP QW active VCSELs, as shown in **Figure 36**, were also reported with $\lambda = 0.85$-μm emission. The 850-nm Al-free active VCSEL structure consists of InGaAsP active region with AlGaAs-based λ-cavity and conventional n- and p-AlGaAs/AlAs-based distributed Bragg reflectors (DBRs). The bottom mirror is composed of 40 pairs of Si-doped AlAs/$Al_{0.16}Ga_{0.84}As$ n-DBRs, grown at 800 °C. The top reflector consists of 22 pairs of 750 °C-grown C-doped AlAs/$Al_{0.16}Ga_{0.84}As$ DBRs. The undoped λ-cavity (grown at 700 °C) consists of three compressively strained 75-Å $In_{0.82}Ga_{0.18}As_{0.8}P_{0.2}$ ($\Delta a/a = 0.6\%$) QWs sandwiched by barriers and confining layers of $Al_{0.25}Ga_{0.75}As$.

CW lasing of the VCSELs, with emission wavelength of 845 nm, was reported by Tansu *et al.* (2000b), with threshold currents of 2.5 and 5.3 mA for devices with diameters of 15 and 20 μm, respectively. RT threshold current density of only 1.4 kA cm^{-2} was achieved for the proton-implanted 850-nm compressively strained InGaAsP QW VCSELs, with diameter of 20 μm; this threshold current density ($J_{th} = 1.4$ kA cm^{-2} for 20-μm-diameter devices) is quite low, in comparison to that ($J_{th} = 2.5$ kA cm^{-2} for 20-μm-diameter devices) of the typical proton implanted 850-nm GaAs QW VCSELs (Wilmsen *et al.*, 1999). The external differential efficiency of the VCSELs ranges from 20% to 25% for 20-μm-diameter devices, which is typical for proton-implanted devices. Optimization of the CS value in the active layer and implementation of strain-compensated InGaAsP/GaAsP/AlGaAs-active regions are expected to further improve device performance. Recently, Chang *et al.* (2004) have also implemented the strain-compensated $In_{0.18}Ga_{0.82}As_{0.8}P_{0.2}$ QW with tensile barriers of 100-Å $In_{0.4}Ga_{0.6}P$ into active regions for VCSELs with improved reliability, high-speed performance, and threshold characteristics.

At shorter emission wavelengths ($0.7\ \mu m < \lambda < 0.8\ \mu m$), the reliability benefits over conventional AlGaAs-active lasers can be substantial. Higher Al-content $Al_xGa_{1-x}As$ QWs lead to lower COMD and hence lower reliable operating output powers. However,

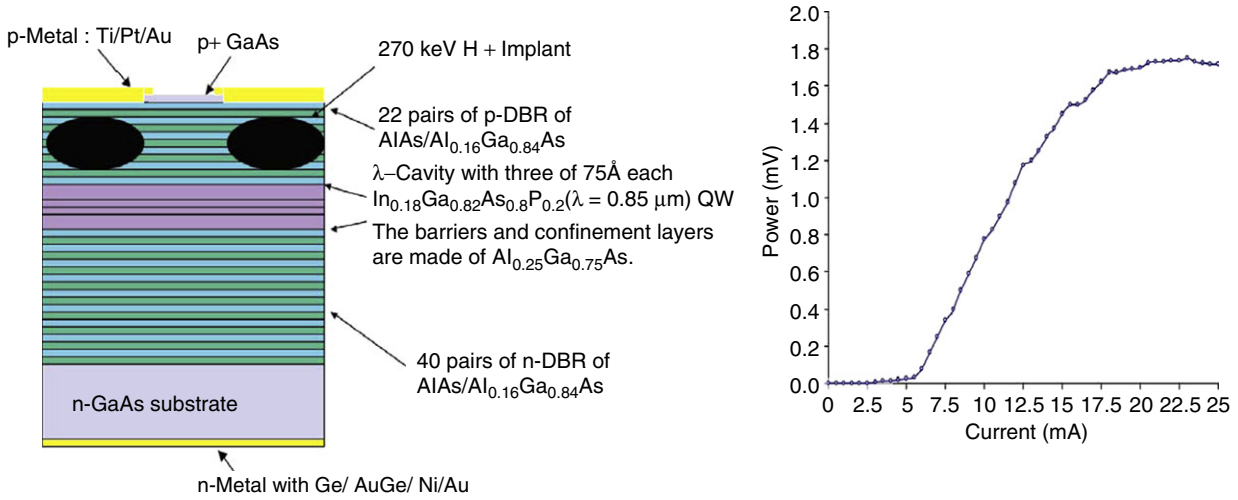

Figure 36 (a) Schematic of an 850-nm compressively strained InGaAsP quantum-well (QW) vertical-cavity surface-emitting lasers (VCSEL). (b) Room-temperature CW L-I curve of 850-nm CS-InGaAsP QW VCSELs, with $d = 20$ μm (Tansu *et al.*, 2000a).

employing a compressively strained InGaAsP QW in this wavelength region is challenging due to the existence of a compositional miscibility gap.

InGaAsP QWs with high CS ($\Delta a/a \sim 1.65\%$) have been reported for emission in the 0.73-μm-wavelength region (Mawst *et al.*, 1999). The solid-phase composition of the 15-nm-thick QW was estimated to be $In_{0.48}Ga_{0.52}As_{0.4}P_{0.6}$. Note that this composition falls within the known miscibility gap of the quaternary material. A BW design was reported with $In_{0.48}(Ga_{0.5}Al_{0.5})_{0.52}P$ cladding layers and an $In_{0.48}Ga_{0.52}P$ lattice-matched (0.8-μm-wide) SCH region. Tensile-strained ($\Delta a/a \sim -0.75\%$) 10-nm InGaP QW barrier layers were utilized to improve carrier confinement and provide partial strain compensation. The use of the higher band-gap $In_{0.48}(Ga_{0.5}Al_{0.5})_{0.52}P$ provides strong carrier confinement and results in relatively large T_0, T_1 values of 115 and 285 K, respectively. Highest device performance was reported on structures grown on substrates with a misorientation of 10° toward ⟨111⟩A. The substrate misorientation provides completely alloy disordered InGaAlP and increases the energy band gap by ~70 meV. In addition, improved PL was obtained from the CS InGaAsP QW, possibly due to improved miscibility of the quaternary material when grown on the misoriented substrate. Burn-in characteristics of such lasers demonstrated 1-W CW operation with minimal degradation (Rusli *et al.*, 2000). Similar CS QW laser structures with single-mode output power have recently been reported by Nomoto *et al.* (2008).

5 Long-Wavelength QW Lasers ($\lambda \sim 1.3$–1.5 μm)

5.1 Challenges for Long-Wavelength Sources

In-plane (edge-emitting) lasers of 1.3 μm or VCSELs operating at a modulation bandwidth of 10 Gb s^{-1}, for the metro application using single-mode fiber, will allow data transmission up to a distance of 20–30 km. Ideally, devices should operate with high performance up to high temperatures (85 °C) in an uncooled environment. Long-haul transmission requires the use of 1.55-μm sources, encouraging the development of low-cost 1.55 $-\mu$m VCSELs. However, conventional InP-based long-wavelength diode lasers, at $\lambda = 1.3$–1.55 μm, are inherently highly temperature sensitive. As a result, additional electronics are needed to maintain the operational temperature of the lasers. This additional temperature controller leads to a significant increase in the laser packaging cost. Furthermore, for high-output-power applications, the low T_0, T_1 values for long-wavelength sources result in thermal rollover at significantly lower CW output powers compared to that achieved with near-IR GaAs-based sources. While much attention has been given to optimizing the heterostructure design of QW lasers in the 980-nm-wavelength region to improve wall plug efficiency, little progress has been made on longer wavelength InP-based devices.

High-output-power lasers in the $\lambda = 1.4$–1.5-μm-wavelength region are needed for fiber pump sources in next-generation Raman-based amplifiers. Longer wavelength, $\lambda > 1.5$ μm, (eye safe) high-power sources are also needed for laser-based radar and free-space optical links. To minimize atmospheric disturbances, these applications prefer sources in the mid-IR (3–5 μm) wavelength region. Efficient, RT operating mid-IR sources are also needed for the development of compact chemical sensing systems, and for IR countermeasures against heat-seeking missiles that threaten both military and commercial airliners. However, the strong temperature sensitivity and radiative inefficiency of conventional long-wavelength InP-, InAs-, and GaSb-based lasers severely impact their CW performance. While InP-based quantum cascade (QC) lasers are available for wavelengths >4 μm, these devices have relatively low power conversion efficiencies at and above RT ($\eta_p < 9\%$) (Evans *et al.*, 2007). Efficient mid-IR (2–5 μm) sources

produced on conventional GaAs or InP substrates would represent a major technological breakthrough over existing type-I and type-II QW lasers that utilize GaSb or InAs substrates. In addition, immature GaSb-based growth and processing technology have hindered the progress of this technology. On the other hand, InP offers many advantages over GaSb, such as better thermal conductivity and the ability to utilize a buried heterostructure. These factors are important for achieving high-output-power, high-efficiency designs. The use of a transparent InP substrate also allows for optical pumping capability of interband devices with high-efficiency near-IR diode lasers (i.e., $\lambda = 980$ nm). For this reason, much effort has been devoted to developing new QW materials that are capable of long-wavelength emission on GaAs or InP substrates.

The strong temperature sensitivity of conventional type-I QW long-wavelength diode lasers stems from various physical mechanisms, including Auger recombination, large carrier leakage from the active layer, intervalence band absorption, and a strongly temperature-dependent material gain parameter (Phillips *et al.*, 1999). Typical values for the conduction band offset for $1.3-\mu$m InGaAsP active lasers on InP-substrate lasers are ≈ 200 meV (Namegaya *et al.*, 1994), which is too low to prevent severe carrier leakage from the QWs as well as increased Auger-assisted carrier leakage (Casey, 1984). Contrary to InP-based lasers, very large conduction band offset (470 meV) (Kondow *et al.*, 1997) can be achieved for a 1.3-μm emitting QW active with GaAs confinement layers. The large band offset helps to suppress thermally induced carrier leakage out of the QW to the confining region and also the Auger-assisted carrier leakage.

Due to the potential advantages offered from 1.3 to 1.55-μm GaAs-based lasers, there have been many efforts directed toward achieving 1.3–1.55-μm emission using various types of active material on GaAs substrates. In(Ga)As QDs have been pursued by many different groups with considerable successes in the 1.3-μm region (Bimberg *et al.*, 1997; Huffaker *et al.*, 1998; Mukai *et al.*, 1999; Bhattacharya *et al.*, 2000; Stintz *et al.*, 2000). QD active lasers exhibit extremely low transparency current densities because of the small active volume. However, low modal gain, high temperature sensitivity, and poor modulation response are still issues under development by many groups. Higher optical gain from the QD active region can be achieved by stacking the QD layers, although this also scales the transparency current density. Also, the use of p-doped QDs and tunneling injection into the QDs has resulted in significantly improved laser small signal modulation bandwidths, 25 GHz at $\lambda \sim 1.1$ μm and 11 GHz at $\lambda \sim 1.3$ μm, as well as reduced device temperature sensitivity (Fathpour *et al.*, 2005). P-doping of the QD active region has also led to improvement in the peak gain and produced low temperature sensitivity QD lasers (Shchekin *et al.*, 2002). Other promising alternatives for 1.3–1.55-μm emission active regions include the use of GaAsSb-active materials (Anan *et al.*, 1998; Ryu and Dapkus, 1999; Blum and Klem, 2000).

An attractive approach for achieving long-wavelength laser emission on GaAs substrates is the use of highly strained InGaAs or InGaAsN QWs. The use of highly strained InGaAs QW active lasers to extend the emission wavelength to 1.20 μm was pioneered by Sato and Satoh (1999a, 1999b) and Koyama *et al.* (1999). More recently, GaAsP tensile barriers have also been implemented to strain compensate the InGaAs QWs (Choi *et al.*, 1999; Tansu and Mawst, 2001). The reduction in the band gap of the InGaAsN materials, pioneered by Kondow *et al.* (1997), due to the presence of the N, is also followed by reduction in the CS of the material due to the smaller native lattice constant of InGaN compound.

5.2 MOCVD-Grown InGaAs(N) Laser Structures

Some of the highest performing InGaAsN-based lasers were initially demonstrated using MBE growth (2000). However, for manufacturing considerations such as high throughput, MOCVD growth is desirable. The optimization of MOCVD-grown InGaAsN materials and an understanding of growth limitations are essential to achieve this goal.

Nitrogen is usually incorporated into the InGaAs QW using low-temperature MOCVD growth with dimethylhydrazine as the nitrogen source. Early studies of InGaAsN active lasers were disappointing in that nitrogen concentrations of 2–3% resulted in poor RT PL intensity and very high-threshold current density lasers (Sato, 2000). More recently, lower MOCVD growth temperatures have been utilized to achieve higher indium incorporation, without strain relaxation, thereby requiring smaller amounts nitrogen to achieve 1.3-μm emission (Kawaguchi *et al.*, 2001; Takeuchi *et al.*, 2001; Tansu *et al.*, 2002a). The smaller nitrogen content ($<0.5\%$) in the InGaAsN active region results in significantly improved PL intensity and reduced threshold current densities (0.225 kA cm^{-2}) (Tansu *et al.*, 2002a, 2003a).

One of the challenges in growing InGaAsN QW lasers by MOCVD is the difficulty of incorporating N into the InGaAs QW, while maintaining a high optical quality film. The low purity of the N precursor used in MOCVD (U-DMHy) is also suspected as a possible reason for the low optical quality of MOCVD-grown InGaAsN QWs. In order to incorporate sufficient N into the InGaAsN QW, very large [DMHy]/V (as high as 0.961) is required. Due to the high cost and the low purity of the DMHy precursor, lowering the [AsH_3]/III to achieve large [DMHy]/V would be the preferable option to increase the DMHy flow. As a result, a large [DMHy]/V ratio requires the [AsH_3]/III ratio to be rather low. Takeuchi *et al.* (2002) demonstrated that the growth of InGaAs QW ($\lambda = 1200$ nm) with the very low [AsH_3]/III ratio is significantly more challenging compared to the case in which tertiarybutylarsine (TBA) is utilized as the As precursor. As the [AsH_3]/III ratio is reduced, the luminescence of the InGaAs QW reduces rapidly for low [AsH_3]/III (below 15–20), which is however required for achieving sufficiently large [DMHy]/V. These challenges have resulted in difficulties in realizing high-performance MOCVD-InGaAsN QW lasers with AsH_3 as the As-precursor until recently. In the work by Tansu and Mawst (2002), the design of the active region is based on strain-compensated InGaAsN QW, with very high In content

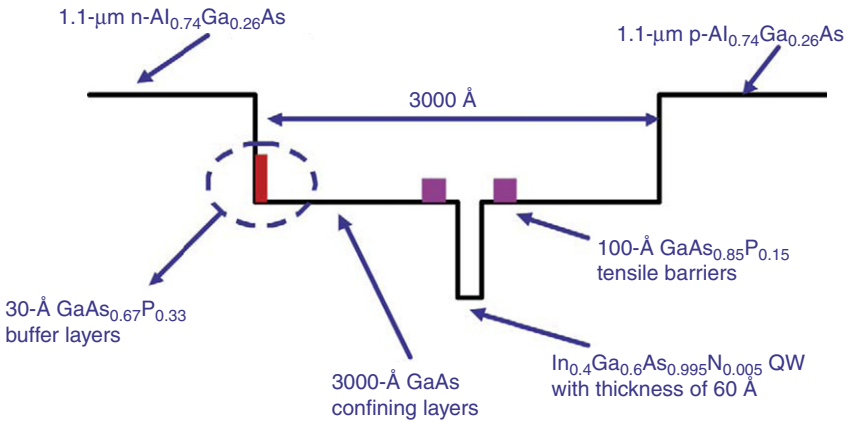

Figure 37 Schematic condition band diagram of InGaAsN quantum-well (QW) ($\lambda \sim 1.30$ μm) laser structure.

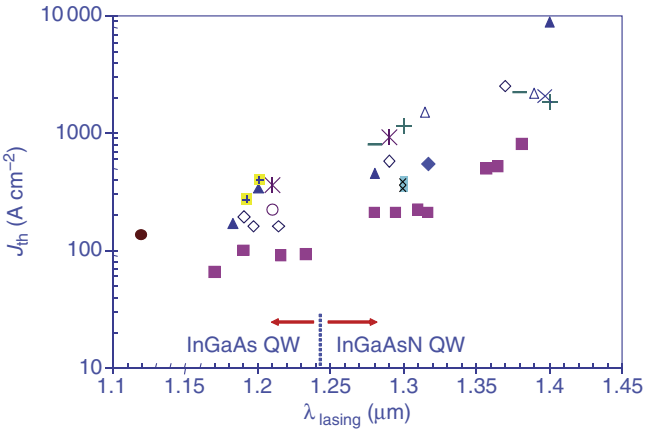

Figure 38 Comparison of threshold current density of InGaAs(N) lasers as a function of emission wavelength (Tansu *et al.*, 2004).

(In ~40%) and minimum N content (N ~ 0.5%), to achieve 1300-nm emission (**Figure 37**). Minimum N content in the InGaAsN QW allowed for growth of the active region with an optimized AsH_3/III ratio. Through MOCVD growth optimization, InGaAsN lasers were reported up to 1.38 μm (Tansu *et al.*, 2004) (**Figure 38**). However, there is a clear trend of increasing threshold current density with increasing nitrogen incorporation (i.e. longer emission wavelengths). Nevertheless, relatively low threshold current densities, as low as 780 A/cm^2, were reported from MBE grown devices emitting near 1510 nm (Jaschke *et al.*, 2005).

While VCSELs are of high commercial interest, the study of edge-emitting lasers is a convenient means to quantify specific material-dependent device performance. Multilength studies of wide-stripe edge-emitting lasers allow extraction of many temperature-dependent device parameters. In addition, comparative studies with state-of-the-art InP-based lasers allow us to clarify the advantages of the InGaAsN-based lasers.

To compare the lasing performance of the 1300-nm InGaAsN QW lasers with those of the conventional InP technology, the published results that represent among the best performance 1300-nm diode lasers based on conventional InP technology (InGaAsP-QW (Belenky *et al.*, 1999) and InGaAlAs-QW (Savolainen *et al.*, 1999)) are shown in **Figure 39**. Due to the low material gain parameter, carrier leakage, and Auger recombination, typically 1300-nm InGaAsP-InP QW lasers require multiple QWs, ranging from 9 to 14 QWs. The 1300-nm InGaAlAs QW requires approximately four to six QWs for optimized structures.

For optimized 1300-nm InGaAsP-QW structures, the threshold current densities of approximately 1650–1700 A cm^{-2} were achieved for devices with cavity length of 500 μm at an operation temperature of 80 °C, as reported by Belenky *et al.* (1999). The threshold current density of the 1300-nm diode lasers based on the InGaAlAs QW on InP, with cavity length of 1000 μm, has been reported as approximately 1350 A cm^{-2} at a temperature of 80 °C (Savolainen *et al.*, 1999). By contrast, the InGaAsN QW lasers require only an SQW active region for high-temperature operation, owing to the larger material gain parameter and better electron confinement in the QW. For example, the 1300-nm InGaAsN SQW as-cleaved diode lasers, with cavity lengths of 500 and 1000 μm, have threshold current densities of only 940 and 490 A cm^{-2}, respectively, at a heatsink temperature of 80 °C (**Figure 39**).

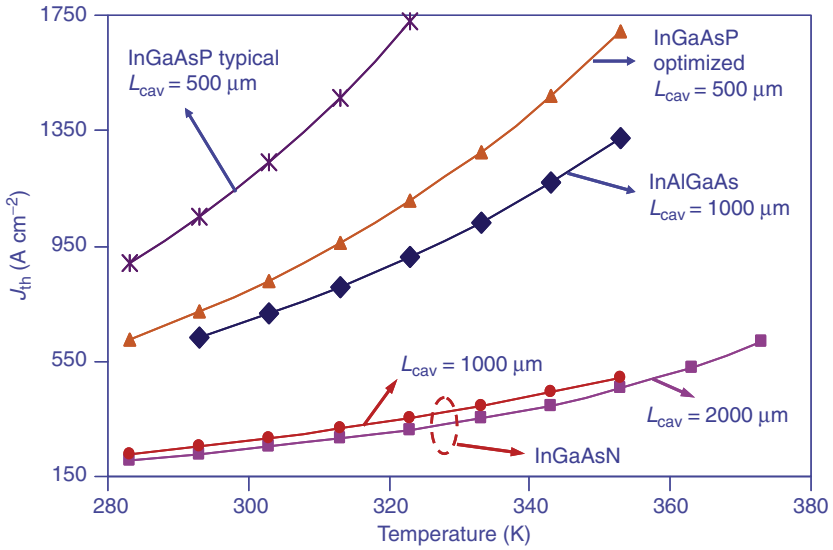

Figure 39 Comparison of J_{th} for InGaAsN, AlGaInAs, and InGaAsP active lasers as a function of temperature (Tansu *et al.*, 2003a).

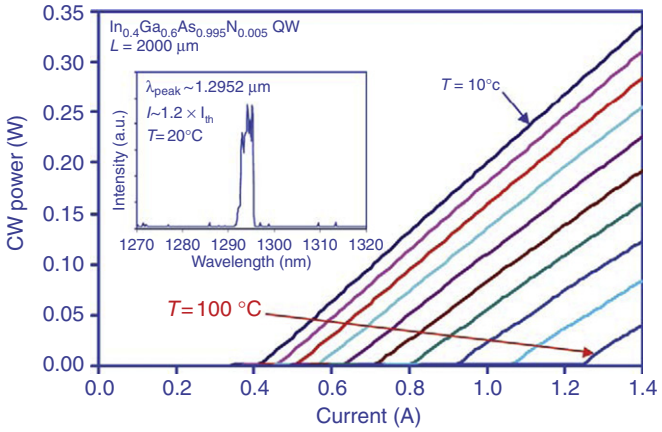

Figure 40 High-temperature continuous-wave (CW) operation of metal-organic chemical vapor deposition (MOCVD)-grown InGaAsN lasers (Tansu *et al.*, 2003a).

The low temperature sensitivity of InGaAsN lasers allows low-threshold current density CW operation at high temperature (**Figure 40**) and high CW output powers (1.8 W). At elevated temperatures of 80 and 100 °C, the threshold current densities of the high reflective/antireflective (HR/AR)-coated (L_{cav}=2000 μm) lasers are measured as only 455 and 615 A cm^{-2}, respectively, under CW operation (Tansu *et al.*, 2003a).

While high-performance 1300-nm QW lasers have now been demonstrated by both MBE and MOCVD, a decrease in the threshold current density (J_{th}) of the InGaAsN QW laser is typically accompanied with a decrease in the T_0 value. There are several possible factors underlying the lower T_0 values of high-performance 1300-nm InGaAsN QW lasers. Carrier recombination mechanism studies, based on the *Z*-factor analysis, have attributed Auger recombination as the primary factor that leads to the lower T_0 values of the high-performance InGaAsN QW lasers. However, since these studies do not account for the possibility of carrier leakage, the Auger recombination coefficients may be overestimated. Other studies (Tansu and Mawst, 2003b), which indicate that the current injection efficiency is a strong function of temperature, have suggested carrier leakage as well as temperature-sensitive material gain in InGaAsN QW lasers as major contributing factors leading to the lower T_0 values of InGaAsN QW lasers. At present, a complete understanding of recombination mechanisms, temperature dependence of the material gain, and carrier leakage in this material system is lacking. However, the combined effect of the various temperature-sensitive mechanisms is likely responsible for the low T_0, T_1 values observed in dilute nitride lasers.

Extending the emission wavelength of InGaAsN active lasers to 1.55 μm and beyond remains a considerable challenge, requiring new active layer materials or new structure designs. There have been several efforts in extending the wavelength on GaAs,

by utilizing highly strained InGaAsN or InGaAsN(Sb) QWs (Bank *et al.*, 2007) or InGaAs-GaAsSb type-II QWs (Dowd *et al.*, 1999). While initial results appear promising, poorer performance, compared with conventional InP-based lasers, remains an issue. The use of InGaAsN(Sb) has allowed emission wavelengths out to 1.55 μm, with very low-threshold current density, 318 A cm^{-2} (Bank *et al.*, 2007). However, device temperature sensitivity is still an underlying issue. Furthermore, extending the emission wavelengths beyond 1.5 μm with this technology is unlikely due to the high strain of the QW employed. New dilute-nitride-based active layer materials are needed to enable device performance surpassing conventional InP- and GaSb-based lasers with long-wavelength emission.

As discussed above, a key attribute of GaAs-based long-wavelength lasers is the lower temperature sensitivity they exhibit compared with conventional InP-based lasers. Yet, a detailed understanding of the mechanisms involved and their control is lacking. Several experimental results have demonstrated low temperature sensitivity for InGaAsN QW lasers in the wavelength regime of 1.25–1.3 μm. Although high values of the characteristic temperature coefficient for threshold current density ($T_0 = (1/J_{th})\, dJ_{th}/dT$) have been demonstrated by several groups, there has been no consensus on how to interpret the T_0 values in terms of fundamental device performance. The T_0 value, which is a figure of merit for temperature insensitivity of the threshold current density, depends strongly on the various physical device parameters and their temperature dependence. In addition, the T_0 values of lasers with high-threshold current densities can be anomalously high due to large defect-induced monomolecular recombination (Tansu *et al.*, 2002a).

As shown in **Figure 41** the reduction of carrier leakage from the InGaAsN QW with GaAsP direct barriers has resulted in a significant lowering of the threshold current density for the InGaAsN QW lasers at elevated temperatures, in comparison to InGaAsN QW lasers with GaAs direct barriers. The increases in the T_0 and T_1 values have been observed for all cavity lengths of the InGaAsN QW lasers with GaAsP direct barriers, which confirm the reduction of carrier leakage (Tansu *et al.*, 2003c).

However, the utilization of a high band-gap material as the barrier may incur a stronger quantum confinement effect and emission wavelength blue-shift. Therefore, it motives the idea of employing smaller band-gap material for the purpose of realizing longer wavelength lasing devices, at the possible expense of reduced carrier confinement. Appropriate comparison studies with identical laser structures except for the barrier materials are needed to fully identify the impact of barrier material on device performance. Tansu *et al.* (2003c) reported 1317-nm emitting InGaAsN–GaAsN lasers with improved threshold current density and T_0 compared with GaAs barrier structures. Other reports, using MBE-grown material, by Egorov and coworkers also demonstrated improved threshold current, but degraded T_0 values for their SQW InGaAsN–GaAsN lasers. We see that the emission wavelength is extended by employing GaAsN barrier materials, however, possibly at the expense of electron confinement. By contrast, employing GaAsP barriers leads to a blue-shift and stronger electron confinement. The $k \cdot p$ simulated emission wavelength for various barrier materials is shown in **Figure 42**.

In order to conclusively determine the role of nonradiative recombination in InGaAsN lasers, the radiative efficiency can be estimated from multisegment ASE measurements as described in Section 2. Comparison studies of the optical gain, radiative efficiency, and carrier lifetime between highly strained InGaAs and InGaAsN QW lasers were reported previously (Palmer *et al.*, 2005a, 2005b). The addition of nitrogen into the QW active region was found to reduce the radiative efficiency to $<10\%$ at RT, as well as increase the temperature sensitivity of the radiative efficiency. From small signal frequency response measurements and using an analysis that separates the contribution of electrical parasitic, the differential carrier lifetime and its dependence on carrier density in InGaAs and InGaAsN QW laser diodes was reported by Anton *et al.* (2005a, 2005b). These results show that the incorporation of nitrogen significantly reduces the differential carrier lifetime. This is mainly due to an almost fourfold increase in the monomolecular recombination term, presumably due to increased defect recombination in the nitrogen-containing alloy.

The QW material and structure design also determine the modulation speed characteristics. The electron–photon resonance frequency is independent on the carrier lifetime since the QW concentration is pinned at threshold and determined by the device

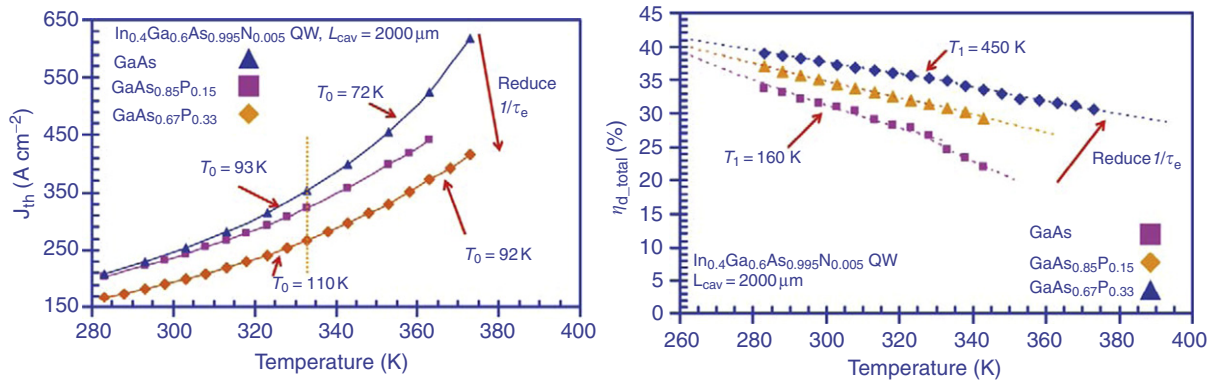

Figure 41 Measured temperature-dependent (a) threshold current density and (b) differential quantum efficiency (DQE) for 60-Å $In_{0.4}Ga_{0.6}As_{0.995}N_{0.005}$ quantum-well (QW) lasers with GaAs and GaAsP direct barriers.

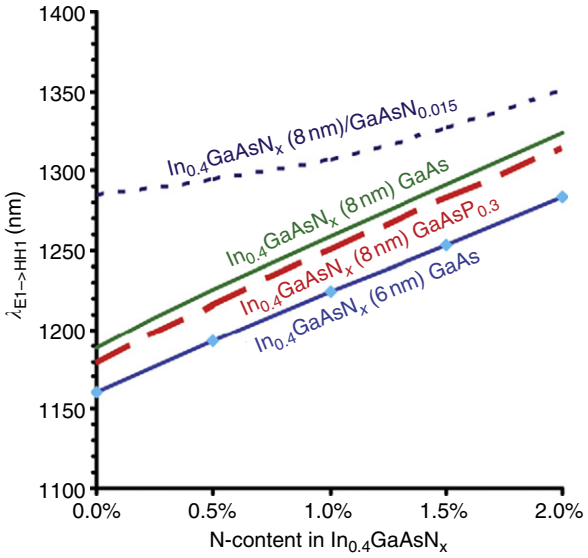

Figure 42 A 10-band $k \cdot p$ simulation study of InGaAs(N) quantum-well (QW) emission wavelength as a function of barrier material and N-content.

differential gain with respect to the carrier concentration and the number of photons in the cavity, that is, device output power. The approximate expression for the electron–photon resonance frequency is given by Fukushima *et al.* (1993):

$$f_R^2 = \frac{1}{4\pi^2}\frac{1}{V}\frac{1}{h\nu}\frac{c}{N_{eff}}\frac{a_m + a_i}{a_m}\Gamma\frac{\partial G}{\partial n}\left(1 + \frac{\tau_{DC}}{\tau_E}\right)^{-1} P_0 \qquad [48]$$

where V is an active region volume, $h\nu$ is photon energy quantum, c is velocity of light in vacuum, N_{eff} is modal refractive index, Γ is optical confinement factor, dG/dn is material differential gain with respect to carrier concentration, τ_{DC} is capture time of the carrier into QW, including diffusion time, and τ_E is escape time from QW into waveguide. The below- and above-threshold frequency responses of InGaAsN QW lasers with different nitrogen content in the QW were reported in Anton *et al.* (2005a, b). The below-threshold analysis revealed the increased contribution of monomolecular recombination in shaping the carrier recombination of InGaAsN lasers even at biases near threshold. From the above-threshold frequency response measurements, an SQW InGaAsN laser demonstrated –3-dB bandwidths of ~6 GHz at moderate powers (2.5 mW). From the slope of the frequency response versus output power, the effective differential gain, $a_{eff} = a/(1+R)$, where $R = \tau_{cap}/\tau_{esc}$, is extracted from experiment. Note that it is not possible to experimentally separate the true differential gain 'a' from the measured effective differential gain, a_{eff}. Thus, the carrier escape time, τ_{esc}, which is strongly dependent on carrier leakage, can have a significant impact on the frequency response. In fact, the value of a_{eff} for InGaAsN QW lasers was found to be reduced by a factor of 2–3 over that from InGaAs QW lasers at high temperature (80 °C) (Anton *et al.*, 2006). Relative intensity noise (RIN) spectra measurements also indicate a decrease by factor of 2 in the effective differential gain compared with similar N-free InGaAs QWs (Shterengas *et al.*, 2004). More recently, optimized dilute-nitride (1.3 μm) QW lasers employing a double quantum-well active region and a ridge waveguide design have demonstrated small signal 3 dB modulation bandwidths of 17 GHz at 25 C near (Wang *et al.*, 2009).

Spectra of the α-factor for multimode InGaAsN QW devices with 0, 0.5, and 0.8% nitrogen in the QW were reported by Shterengas *et al.* (2005) using the spectral dependence of the modal refractive index, differential gain, and differential index with respect to current. No dependence of the α-factor on nitride composition of QW can be observed within experimental error, with values in the range of 1.7–2.5. This is an important finding, since it indicated that frequency chirp in dilute nitride transmitter sources should not be strongly influenced by the nitrogen content in the active region.

6 InGaN/GaN QW Active Regions

6.1 Introduction to Nitride Semiconductor Lasers and Light-Emitting Diodes

High-performance and high-efficiency III-nitride light-emitting diodes (LEDs) and laser diodes are of great interest for many applications in traffic and automobile display, medical therapy and diagnostic, military applications, full color display, liquid-crystal display (LCD) backlighting, digital video disks (DVDs), and solid-state lighting sources (Schubert, 2006). Visible

(blue and green) and ultraviolet (UV) diode lasers play a very important role in medical, military, and ultrahigh-density DVD. At this point, III-nitride diode lasers (Nakamura *et al.*, 2000) have been utilized primarily for DVD applications. High-performance diode lasers emitting in the blue and green regimes find many potential applications for medical fields, such as lasers for eye surgery and glaucoma therapy (trabeculoplasty procedure), photodynamic therapy for noninvasive cancer treatment, esthetic laser technology, and others.

The advancement of group III-nitride semiconductor materials and devices has advanced rapidly during the past 10 years, primarily driven by the explosion in the visible LED applications for signage and display applications. Theoretically, the highest-efficiency, white-light solid-state source can be achieved by generating blue, green, and red emissions directly from independent LEDs. While InGaN QW LEDs emitting in the blue regime have been realized with acceptable performance, the green and red LEDs utilizing the same QW materials have proven to be challenging. Group III-nitride LEDs emitting in the green regime ($\lambda \sim 520$–540 nm) can be achieved by increasing the In content in the $In_xGa_{1-x}N$ QW to $\sim 24\%$ (with thickness of ~ 25–30 Å), albeit with low efficiency due to the phase separation in the materials. The high QW strain in the InGaN QW (with 24% In content or above) also leads to additional challenges to grow high-quality 2D InGaN QW materials for green emission and beyond with low dislocation density. Group III-nitride LEDs emitting in the red regime ($\lambda \sim 630$–650 nm) requires the capability to grow high-quality InGaN materials with In content above ~ 35–40% for QW materials. For achieving low-cost and high-efficiency monolithic nitride-based white-light solid-state sources, InGaN-based QW active regions with large spontaneous radiative recombination rate emitting in the blue, green, and red regimes are required.

The first pioneering nitride diode laser was realized by Nakamura *et al.* (1996) at Nichia Chemicals. The device utilized an InGaN multi-QW (MQW) active region, emitting at 417-nm under pulsed operation at RT. Demonstration of RT CW operation of MQW InGaN laser diodes emitting at 406 nm with a lifetime of 27 h (Nakamura *et al.*, 1997a, b, c) and at 416.3 nm with 300 h (Nakamura *et al.*, 1997b) quickly followed. Implementation of new growth method, such as epitaxially laterally overgrown GaN technique, reduced defect density and improved the lifetime of MQW InGaN laser diodes (~ 401.5 nm) to an estimated 10 000 h for RT CW operation (Nakamura *et al.*, 1997b). High-power violet laser diodes with an output power ~ 30 mW have now become commercially available for high-density optical disk light source (Nagahama *et al.*, 2000, 2005). The availability of high-performance compact diode lasers emitting in the blue- and green-wavelength regimes allows the low-cost implementation for many medical therapy and diagnostic applications, military applications, and optical storage applications.

6.2 Current Status of Conventional Type-I InGaN QW Lasers

Conventional III-nitride gain media for laser diode emitting in the 420–482-nm regime are based on type-I InGaN QW active region. Type-I InGaN QWs have been implemented as an active region for LED structures covering emission wavelengths ranging from 420 to 650 nm (Xiao *et al.*, 2004). Two major challenges associated with the conventional type-I InGaN QW active region for achieving high-performance LEDs/lasers are related to (1) the high defect density and phase separation in the high-In-content InGaN QW (Nagahama *et al.*, 2000, 2005) and (2) the existence of the polarization electrostatic field in InGaN QW (Xiao *et al.*, 2004).

The first issue is related to the high defect density in nitride material systems, which can be attributed to the large lattice mismatch strain (between III-nitride compound and sapphire substrate) and less-mature epitaxy of III-nitride materials (in comparison to that of GaAs and InP materials), leading to very high-threading dislocation density and resulting in low radiative efficiency of the devices. In particular, for devices utilizing conventional InGaN QW, the strain-induced defects caused by lattice mismatch between InGaN QW and GaN layer compromise the crystal quality of the active region. On average, the InGaN active layer (Nagahama *et al.*, 2005) contains a large number of threading dislocations (10^8–10^{12} cm^{-2}) originating from GaN–sapphire interface, which is typically 4 orders of magnitude larger than that in GaAs material systems. Although nitride devices are found to be less sensitive to dislocations than other III–V devices, high dislocation densities lead to an increase in defect-monomolecular recombination rate, reduction in radiative efficiency, and reduction in device reliability. Significant progresses have also been accomplished on the development of GaN substrates; however, the high cost associated with the substrate still remains an important challenge that needs to be addressed.

The second major issue is the inherent polarization electric field, which is mainly related to the crystal structure and the crystallographic growth orientation of the materials. The existence of polarization field in III-nitride materials is a result of the nonideal internal cell parameters (c/a) of the wurtzite-based III-N materials with [0001] orientation, resulting in the nonzero spontaneous polarization (P_{spon}). The strain in the InGaN QW grown on GaN also results in the nonzero piezoelectric polarization (P_{piezo}). The existence of spontaneous and piezoelectric polarization results in conduction and valence energy band bending, thus leading toward significant reduction of the electron and hole wave function overlap (Γ_{e_hh}). The reduced Γ_{e_hh} overlap in turn will lead to reduced transition matrix element and optical gain of the QW.

The implication of the polarization effect and high defect density in III-N materials leads to high threshold current density ($J_{th} \sim 1.5$ kA cm^{-2} for $\lambda \sim 425$ nm, and $J_{th} \sim 6$ kA cm^{-2} for $\lambda \sim 482$ nm) (Nagahama *et al.*, 2005) in the state-of-the-art type-I InGaN QW lasers for the record lasing performances from Nichia Chemicals, as shown in **Figure 43**. The high-threshold current density in

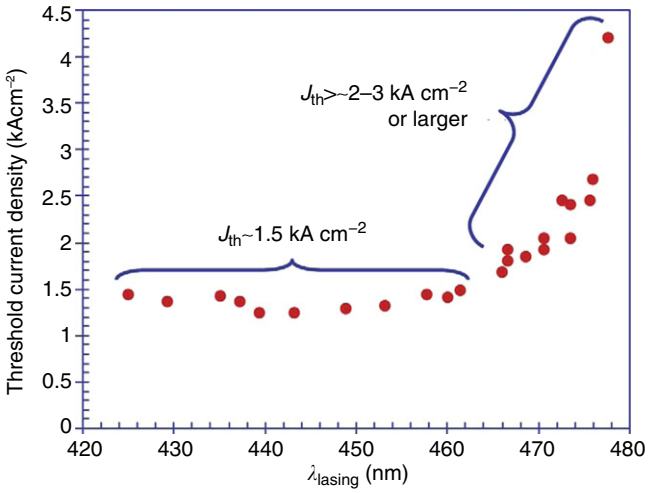

Figure 43 Threshold current density of state-of-the-art InGaN QW lasers for $\lambda \sim 420$–480 nm. Adapted from Nagahama, S., Sugimoto, Y., Kozaki, T., Mukai, T, 2005. Recent progress of AlInGaN laser diodes. Proceedings of SPIE Photonics West, San Jose, CA, USA.

InGaN QW lasers corresponds to approximately an order of magnitude higher than that ($J_{th} \sim 65$–200 A cm^{-2}) of the state-of-the-art GaAs-based lasers. The Γ_{e_hh} for a typical blue-emitting InGaN QW (with 15% In content and thickness of 25 Å) is approximately 35–38%, while the typical Γ_{e_hh} for GaAs-based QW lasers (i.e., InGaAs QW or InGaAsN QW) approaches unity. As the In content in InGaN QW is increased beyond 25–30% for extending its emission wavelength range up to $\lambda > \sim 500$–550 nm, the polarization effect in InGaN QW is enhanced, thus leading to significantly reduced overlap ($\Gamma_{e\_hh} < 20$–25%). Till 2005, InGaN QW lasers was realized only up to emission wavelength of $\lambda \sim 482$ nm (Nagahama *et al.*, 2005), and the challenges of achieving InGaN QW lasers in the $\lambda \sim 500$–550 nm can be attributed to much lower optical gain (due to lower $\Gamma_{e\_hh} < 20$–25%) as well as the phase separation for high-In-content InGaN QW. Good number of efforts has been taken to overcome this challenge by development of the InGaN-based green LDs on the semipolar $(20\bar{2}1)$ GaN substrates (Adachi 2014). Lower threshold current, higher output powers of over 100 mW in the spectral region beyond 530 nm, and higher wall plug efficiencies as high as 7.0–8.9% in the wavelength range of 525–532 nm make the InGaN based LDs on the semipolar $(20\bar{2}1)$ planes promising candidate for application in the green region.

6.3 Impact of Polarization Fields on Optical Matrix Overlap in InGaN QWs

One of the detrimental impacts of the polarization fields in InGaN/GaN QW system is the reduction of its transition matrix element (Arif *et al.*, 2008a). The theory of radiative recombination and optical gain can be understood from the Fermi's golden rule for transition. According to Fermi's golden rule, electronic transition from $|2\rangle$ to $|1\rangle$ is governed by transition matrix element via the perturbation Hamiltonian $\hat{H}'_{21}$[12], resulting in quantum mechanical transition rate as follows:

$$W_{2\to1} = \underline{2\pi}|\hat{H}'_{21}|^2 \rho_f (E_1 - E_2 - \hbar\omega_0) \qquad [49]$$

where ρ_f is the density of the final states and $\hat{H}'_{21}$can be expressed in terms of transition matrix element and envelope function overlap. In semiconductor, the transitions occur between states in the conduction band and valence band, resulting in the following perturbation Hamiltonian

$$|H'_{21}|^2 \propto |\langle u_c|\hat{e}\cdot\bar{p}|u_v\rangle|^2 |\langle F_2|F_1\rangle|^2 \qquad [50]$$

which depends on the square of the transition matrix element $|M_T|^2 = |\langle u_c|\hat{e}\cdot\bar{p}|u_v\rangle|^2$and the square of the envelope electron–hole wave function overlap$|\Gamma_{e_{hh}}|^2 = |\langle F_2|F_1\rangle|^2$. The $|u_c\rangle$ and $|u_v\rangle$ refer to the conduction and valence band Bloch functions, respectively, while the $|f_2\rangle$ and $|f_1\rangle$ are the envelope electron and hole wavefunctions, respectively. The strength of the electric field and electron interaction is indicated by the dot product of the electric field polarization $\hat{e}$ and the electron momentum $\bar{p}$. For the case of spontaneous recombination, the transition matrix element term reduces to $|\langle u_c|u_v\rangle|^2$since the emission is not initiated by the presence of existing photons, but energy fluctuations in the vacuum state instead. Both the spontaneous radiative recombination rate ($W_{Spontaneous}$) and the stimulated emission rate ($W_{Stimulated}$) are then proportional to the square

of the envelope electron and hole wavefunction overlap $|\Gamma_{e_{hh}}|^2$, as follows:

$$W_{\text{Spontaneous}} \sim |\langle u_c|u_v\rangle|^2 |\Gamma_{e_{hh}}|^2 \quad [51]$$

$$W_{\text{Stimulated}} \sim |u_c|\hat{e}\cdot\overline{p}|u_v\rangle|^2 |\Gamma_{e_{hh}}|^2 \quad [52]$$

Therefore, radiative recombination rate and optical gain of III-nitride active regions can be enhanced by engineering the nanostructures with improved overlap.

In III-nitride material systems, the existence of the spontaneous and piezoelectric polarization field inside the materials results in significantly reduced electron–hole wave function overlap Γ_{e_hh} of only $\sim$34% for the case of 30-Å-thick $In_{0.15}Ga_{0.85}N$ QW sandwiched by GaN barriers (as shown in **Figure 44**), emitting in the blue regime ($\lambda \sim 450$ nm). In the absence of polarization effect, the Γ_{e_hh} is computed as $\sim$97% for the case of 30-Å-thick $In_{0.15}Ga_{0.85}N$ QW with GaN barriers.

Notice that as the In content in 25-Å $In_xGa_{1-x}N$ QW is increased to extend the emission wavelength, the overlap Γ_{e_hh} will be severely reduced to only $< \sim$25% for emission wavelength of $\lambda \sim 550$-nm (green regime), as shown in **Figure 45**. It is important to note that the spontaneous radiative recombination rate and the optical gain are directly proportional to the square of the electron–hole wavefunction overlap ($|\Gamma_{e_{hh}}|^2$); thus, the reduced Γ_{e_hh} due to polarization field effect in nitride material systems is very detrimental to achieving low-threshold current density laser diodes and high-efficiency nitride LEDs.

The optical gain of conventional 24-Å $In_{0.28}Ga_{0.72}N$–GaN QW active region is calculated by using self-consistent six-band $k\cdot p$ model (Chuang and Chang, 1996, 1997; Zhao *et al.*, 2009b), taking into account the valence band mixing polarization fields, strain effects, and carrier screening. In **Figure 46**, the gain of an InGaN–GaN QW emitting in the wavelength regime of 480 nm is relatively low, in comparison to a typical gain value for an InGaAs–GaAs QW. The transparency carrier density for an InGaN–GaN QW is approximately 1.5×10^{19} cm^{-3}. By assuming the threshold gain of 1345 cm^{-1}, the predicted threshold carrier density is in

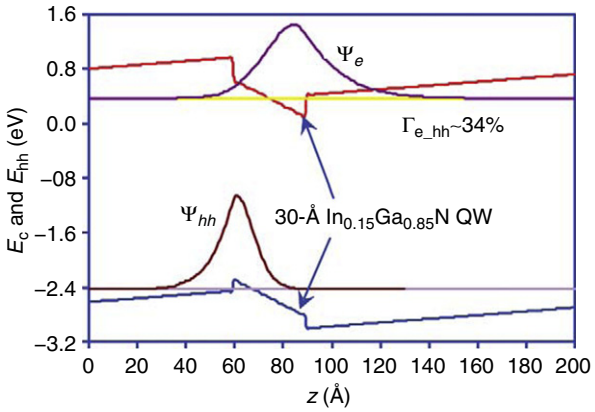

Figure 44 Band lineup for InGaN quantum-well (QW) with polarization field effect, with its corresponding wave functions. Reproduced with permission from Arif, R.A., Zhao, H., Ee, Y.K., Tansu, N., 2008a. Spontaneous emission and characteristics of staggered InGaN quantum wells light emitting diodes. IEEE Journal of Quantum Electronics 44, 573–580.

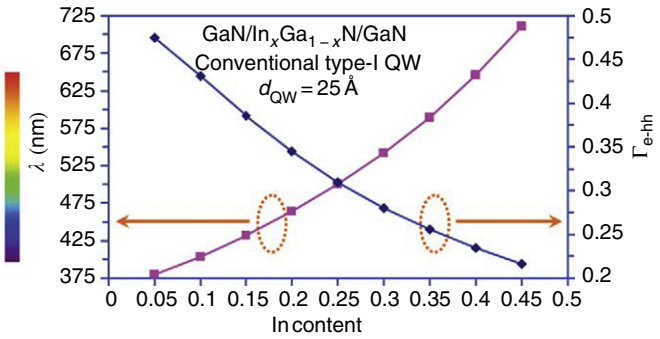

Figure 45 The transition wavelength and Γ_{e_hh} for 2.5-nm-thick InGaN quantum-well (QW) as functions of In content inside the QW. Reproduced with permission from Arif, R.A., Zhao, H., Ee, Y.K., Tansu, N, 2008a. Spontaneous emission and characteristics of staggered InGaN quantum wells light emitting diodes. IEEE Journal of Quantum Electronics 44, 573–580.

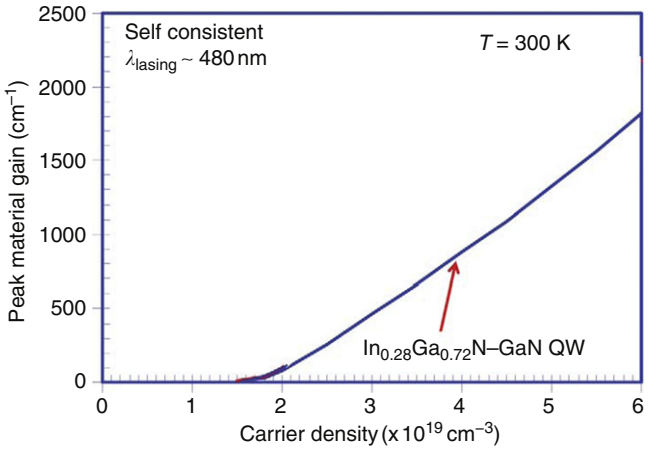

Figure 46 The optical gain of 24-Å InGaN–GaN quantum-well QW calculated using self-consistent six-band $k \cdot p$ model, taking into consideration valence band mixing, polarization effects, strain effects, and carrier screening. Reproduced with permission from Zhao, H., Arif, R.A., Ee, Y.K., Tansu, N., 2009a. Self-consistent analysis of strain-compensated InGaN–AlGaN quantum wells for lasers and light-emitting diodes. IEEE Journal of Quantum Electronics 44, 66–78.

the range of 5.1×10^{19} cm^{-3}. The large threshold carrier density required to achieve lasing is detrimental for laser operation, as the high carrier density will lead to large nonradiative recombination rate in the QW.

6.4 Approaches to Minimize Impact of Polarization Field by Other Groups

Several approaches have been attempted to improve the gain in the nitride-based QW system. In this section, we only focus on several approaches, primarily based on (1) nonpolar InGaN QW approach and (2) nanostructure engineering of InGaN QW structure for improved matrix element. In Section 6.4.1, the nonpolar InGaN QW lasers are discussed. Section 6.4.2 focuses on the use of novel QW active region on *c*-plane GaN that leads to improved matrix element.

6.4.1 Nonpolar III-nitride materials

Efforts to minimize the detrimental impact of polarization field have been and are still being actively pursued by many groups. To minimize electrostatic field, materials growth along nonpolar orientations have been attempted. Starting with growing nonpolar *m*-plane materials on lithium aluminate substrate (Waltereit *et al.*, 2000) and *a*-plane GaN on *r*-plane sapphire (Ng, 2002), more significant successes have been achieved in the recent years. Peak wavelength blue-shift with increasing driving current is typically observed in polar nitride devices due to electric field screening by free carriers. This behavior is not seen in nonpolar InGaN/GaN-based LEDs and lasers, where the peak wavelength stays constant with increasing injection. This clearly indicates the absence of polarization field in the nonpolar *a*-plane InGaN QW.

More recently, nonpolar InGaN/GaN QW lasers emitting at 404 nm grown on nonpolar GaN *m*-substrates in August 2007 have been realized (Farrell *et al.*, 2007). The corresponding *L–I* and *I–V* curve and emission spectra for the nonpolar InGaN/GaN QW lasers are shown in **Figures 47(a)** and **47(b)**, respectively (Farrell *et al.*, 2007). The preliminary nonpolar laser diodes have threshold current density of 6.8 kA cm^{-2}; the devices operate under CW condition at RT for up to 15 h. More recently, nonpolar, *m*-plane InGaN laser emitting at $\lambda = 481$ nm has also been realized (Okamoto *et al.*, 2008), with a high slope efficiency of 0.49 W A^{-1} (Okamoto *et al.*, 2009). Unfortunately, the epitaxy and quality of current nonpolar materials is usually still inferior to the more established *c*-plane (0001) GaN, where nonpolar GaN films are found to contain high concentration of stacking faults and threading dislocations. Note that the quality of III-nitride materials grown on *c*-plane substrates is typically relatively poor with dislocation density in the range of 10^7–10^8 cm^{-2}, as compared with those in GaAs/InP materials system with defect density below $< 10^2$ cm^{-2}. Thus, the higher dislocation density of nonpolar InGaN/GaN materials still requires further improvement in its material quality for realizing high-performance and reliable devices. However, the progress in the nonpolar InGaN–GaN QW active region is very promising, and it is expected that the nonpolar nitride materials and devices would have tremendous impacts in the field of diode lasers and solid-state lighting.

6.4.2 Polarization Field Engineering in InGaN QW

In contrast to the approach to grow on nonpolar GaN substrate, several approaches have also been proposed to suppress the charge separation effect in InGaN QW active region, as follows:

(1) the use of δ-AlGaN layer in InGaN QW (Park and Kawakami, 2006),
(2) staggered InGaN QW (Arif *et al.*, 2007, 2008b),

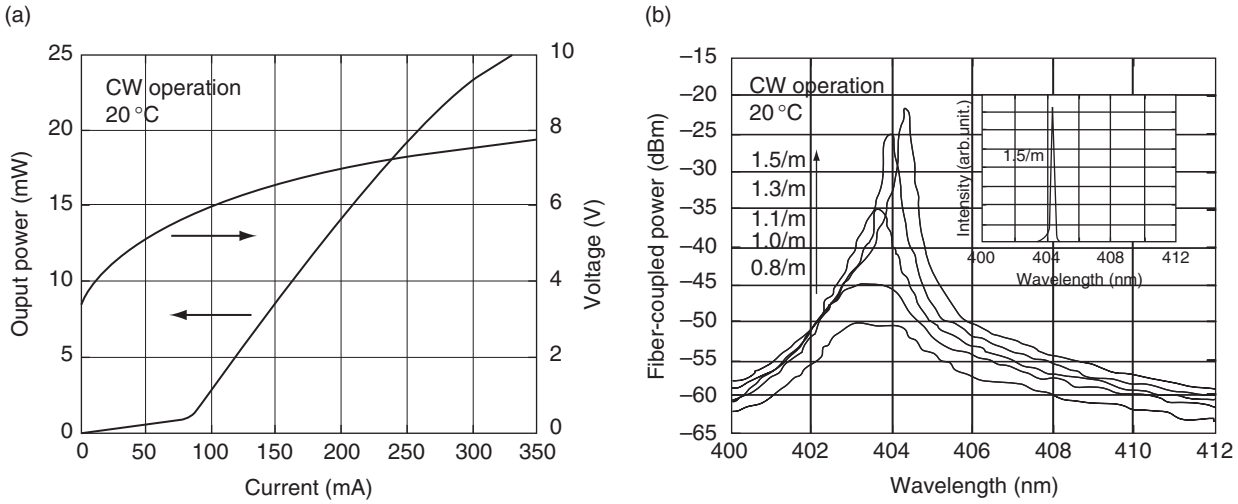

Figure 47 Plots of (a) output power, operating voltage vs. current and (b) continuous-wave (CW) spectra of nonpolar InGaN/GaN quantum-well (QW) lasers grown on *m*-plane substrates. Reproduced with permission from Farrell RM, Feezell DF, Schmidt MC, *et al.* (2007) Continuous-wave operation of AlGaN-cladding-free nonpolar m-plane InGaN/GaN laser diodes. Japanese Journal of Applied Physics 46: L761–L763.

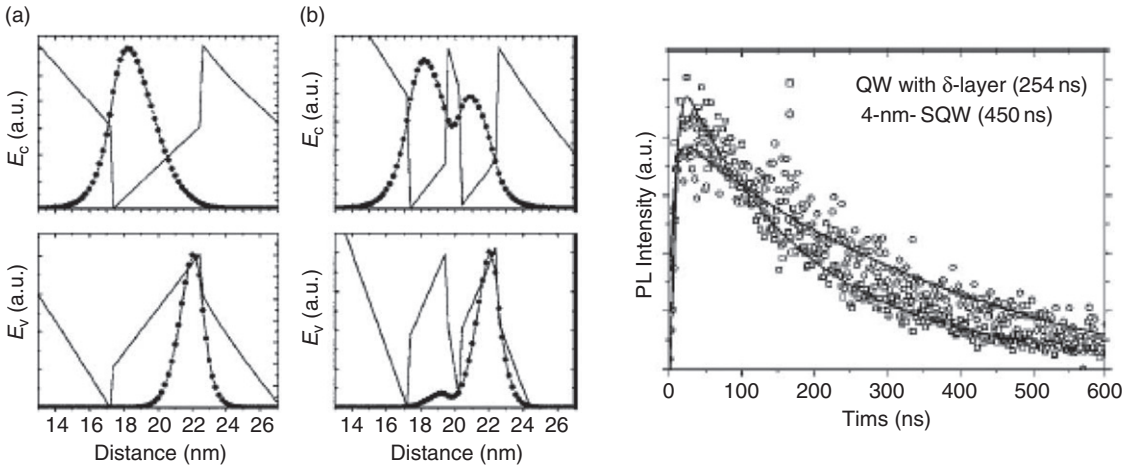

Figure 48 (a) Energy band lineup with the corresponding electron and hole wavefunctions and (b) time-resolved spectroscopy measurement of conventional InGaN quantum-well (QW) and InGaN-δ AlGaN QW structure. Reproduced with permission from Park, J., Kawakami, Y., 2006. Photoluminescence property of InGaN single quantum well with embedded AlGaN δ layer. Applied Physics Letters 88, 202107.

(3) type-II InGaN–GaNAs QW (Arif *et al.*, 2007; Zhao *et al.*, 2008), and
(4) strain-compensated InGaN–AlGaN QW (Zhao *et al.*, 2009b).

6.4.2.(i) InGaN QW with delta layer of AlGaN

In a distinct approach to minimize the impact of polarization field, a thin (1 nm) AlGaN layer (also called *δ*-AlGaN) inserted into thick InGaN QW (4 nm) has been proposed by the group in Kyoto University (Park and Kawakami, 2006). As calculated from the energy band lineup of the QW structure shown in **Figure 48(a)**, an improvement in the electron–hole wave function overlap can be achieved. Time-resolved photoluminescence spectroscopy performed on the samples (**Figure 48(b)**) also shows reduction in the carrier radiative lifetime over the SQW structure, indicating increased spontaneous recombination rate in the InGaN-*δ* AlGaN QW structure.

Optical gain analysis of InGaN-*δ* AlGaN QW was also performed (Park *et al.*, 2007). At a particular carrier density, InGaN-*δ* AlGaN QW offers a much higher optical gain, as compared with that of the conventional InGaN QW. The increase in the optical gain observed in InGaN-*δ* AlGaN QW can be attributed to the increase in its optical matrix element, in comparison to that of a conventional InGaN–GaN QW. Attributing to the increased electron–hole wavefunction overlap in InGaN-*δ* AlGaN QW, increased radiative efficiency in nitride-based LEDs has been reported (Park and Kawakami, 2006). However, the use of AlGaN has several

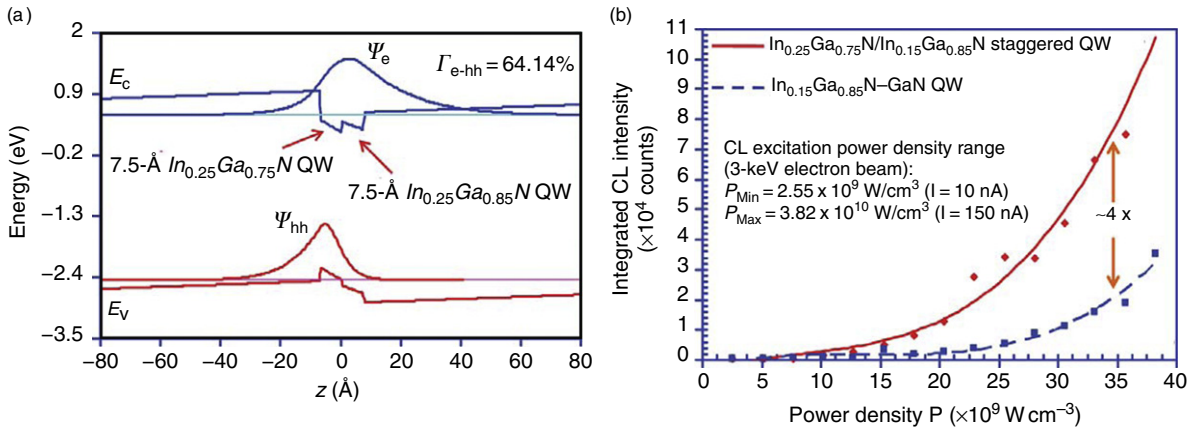

Figure 49 (a) Schematics of staggered InGaN quantum-well (QW) active region with improved electron–hole wavefunction overlap (Γ_{e_hh}). The corresponding electron and hole wavefunctions are also plotted. Reproduced with permission from Arif, R.A., Ee Y.K., Tansu, N., 2007. Polarization engineering via staggered InGaN quantum wells for radiative efficiency enhancement of light emitting diodes. Applied Physics Letters 91, 091110. (b) The comparison of integrated luminescence intensity of staggered InGaN QW and conventional InGaN QW-active regions, in agreement with predicted theory. Reproduced with permission from Arif, R.A., Zhao, H.P., Ee, Y.K., *et al.*, 2008. Spontaneous recombination rate and luminescence efficiency of staggered InGaN quantum wells light emitting diodes. Proceedings of the IEEE/OSA Conference on Lasers and Electro-Optics (CLEO) 2008, San Jose, CA, May 2008, paper CMAA2.

limitations for the growth of InGaN QW, in particular as the optimum growth temperature for AlGaN is typically 300 °C much higher than that of an InGaN QW. Another disadvantage of this approach is that the QW thickness is limited to thick QWs only (>4 nm thick), which inherently has a very low wavefunction overlap. A more typical InGaN QW thickness employed in visible-emitting LEDs and lasers ranges from 2 up to 2.5 nm.

6.4.2.(ii) Staggered InGaN QW Active Region

The use of staggered InGaN QW with step-function-like In contents in the QW results in polarization band engineering (as shown in **Figure 49(a)**), which can be utilized to increase the electron–hole wave function overlap (Arif *et al.*, 2007, 2008a; Zhao *et al.*, 2009b). The novel staggered InGaN QWs can be designed to suppress the charge separation effect by a factor of 2, which translates to approximately a factor of 4× improvement in radiative recombination rate and efficiency of the LEDs. In the conventional InGaN–GaN QW, the active region is composed by InGaN QW with a particular In content sandwiched by GaN barriers. However, as the active region is designed by staggering the InGaN layers with high and low In contents, as shown in **Figure 49(a)**, a significant enhancement in the electron–hole wavefunction overlap can be achieved leading to active region with improved gain and radiative recombination rate.

The PL and cathodoluminescence (CL) measurements conducted on both QW samples (blue and green emission) indicated improvement of the peak intensities for the staggered InGaN QWs up to ~3.6–4.2 times (**Figure 49(b)**), in comparison to that of the conventional approach. Utilizing the same concept, the staggered InGaN QW LEDs exhibited a significant improvement in output power and efficiency, in comparison to that of conventional type-I InGaN QW. Comprehensive simulation and experimental studies have also been carried out on staggered InGaN QWs. Currently, research works on staggered InGaN QW LEDs have been geared toward optimization for high radiative efficiency green LEDs, and potentially the high optical gain design could lead to sufficient gain for lasing in the green emission spectral regime.

6.4.2.(iii) Type-II InGaN–GaNAs QW active region

In contrast to the approach utilizing staggered InGaN QW and strain-compensated InGaN–AlGaN QW, one of the interesting large optical gain active regions can be realized by employing type-II InGaN–GaNAs QW active region (see **Figure 50(a)**) for lasers and LEDs (Arif *et al.*, 2008b; Zhao *et al.*, 2008). The concept of type-II 'W' QW active region was first proposed and demonstrated by Meyer and coworkers in the GaSb material system for mid-IR lasers (Meyer *et al.*, 1995; Vurgaftman *et al.*, 2001), and currently state-of-the-art GaSb-based type-II QW lasers have been demonstrated as among the leading diode lasers in the mid-IR regimes. Recently, dilute nitride type-II 'W' QW active regions have also been proposed and demonstrated for laser applications in the 1550-nm (Tansu, 2003b; Vurgaftman and Meyer, 2003a) and $3-5\ \mu$m (Vurgaftman and Meyer, 2003a) regimes on GaAs and InP substrates, respectively.

The use of dilute As GaNAs layer with As contents of 2–6% results in type-II band alignment in the InGaN–GaNAs–InGaN heterostructure, thus allowing type-II QW design with significantly larger wavefunction overlap (Γ_{e_hh}=65–70%), in comparison to that (Γ_{e_hh}=25–30%) of the conventional InGaN QW. It is important to note that the proposed type-II QW structure employs thin (1-nm) GaNAs layer with low As content (As <5%). The growth of single-phase wurtzite GaNAs alloy had been recently

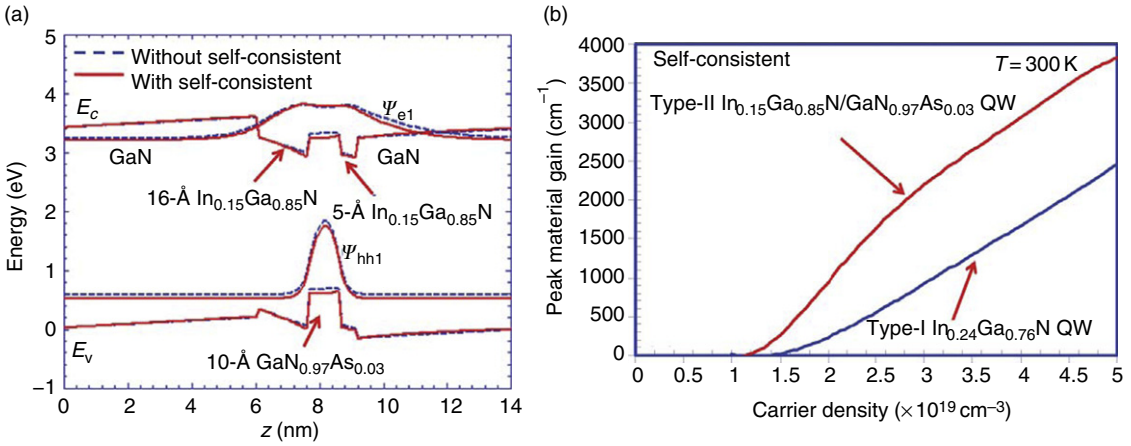

Figure 50 (a) Schematics of type-II InGaN–GaNAs quantum-well (QW) active region with its corresponding electron and hole wave functions calculated under self-consistent method and (b) the comparison of peak gain vs. carrier density for type-II InGaN–GaNAs QW and type-I InGaN QW (Zhao *et al.*, 2008).

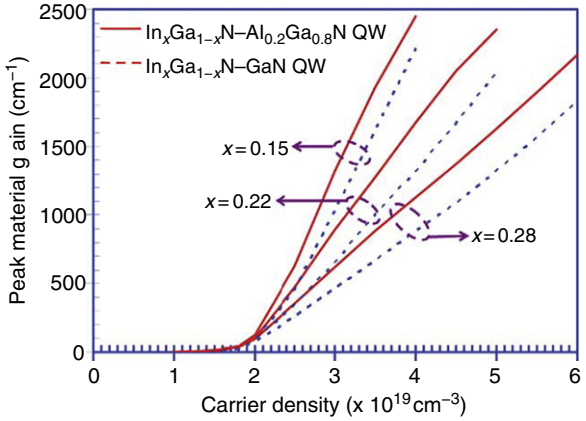

Figure 51 Peak material gain for strain-compensated InGaN–AlGaN quantum-well (QW) and conventional InGaN–GaN QW as function of carrier density at temperature of 300 K for different indium contents (15, 22, 28%) (Zhao *et al.*, 2009a).

demonstrated by MOCVD (Kimura *et al.*, 2004). Recent studies (Wu *et al.*, 2004) showed that incorporation of dilute-As into the GaN alloy shows hybridization of the localized As states and the GaN valence band. The valence band hybridization in GaNAs leads to formation of a new valence band with transitional gap of the N-rich GaNAs lying between 2.5 and 2.7 eV (Wu *et al.*, 2004), which also in turn leads to increase in the valence band offset in dilute As GaNAs/GaN heterojunction (Wu *et al.*, 2004).

Self-consistent analysis for the type-II QW active region was developed based on six-band $k \cdot p$ band-structure model for wurtzite III-nitride semiconductors, and the analysis indicated that the optical gain (as shown in **Figure 50(b)**) and radiative recombination rates were increased by ~2 times and ~3–4 times, respectively. The use of type-II InGaN–GaNAs QW has the potential for achieving high radiative efficiency LEDs and low-threshold current density lasers in the green spectral regime.

6.4.2.(iv) Strain-compensated InGaN–AlGaN QW active region

In addition to the use of staggered InGaN QW and type-II InGaN–GaNAs QW, another nitride-based active region design with improved gain can be achieved by employing strain-compensated InGaN–AlGaN QW active region for LEDs and lasers (Zhao *et al.*, 2009a). In strain-compensated InGaN–AlGaN QW, the use of tensile AlGaN barriers to surround the compressively strained InGaN QW leads to reduced total strain in the QW+ barrier system. The use of strain-compensated InGaN–AlGaN QW also results in 50–80% improvement in the radiative recombination rate, and the optical gain is expected to improve by 25% over the conventional InGaN–GaN QW (as shown in **Figure 51**). **Figure 51** shows that the improved gain characteristics of strain-compensated InGaN–AlGaN QW lead to the possibility of reducing the threshold carrier density in InGaN–AlGaN QW lasers, which will in turn lead to suppression of nonradiative components of the threshold current density for nitride lasers.

6.5 Summary on InGaN–GaN QW Lasers

The pursuit of high-performance and low-threshold InGaN QW lasers is important for many applications in biomedical and display areas, and the progress in this area will be strongly correlated to the progress in the solid-state lighting area. The performance of nitride-based diode lasers has progressed very significantly in the past several years. It is expected that the progress of future generation nitride lasers will focus on reducing the threshold current density, improving the wall plug efficiency, and pushing the emission wavelength to green wavelength regime. The pursuit of nitride-based green diode lasers has been very challenging, primarily limited by the poor gain of the conventional active region. It is expected that the green nitride lasers will be realized by improving the optical gain of the QW active region by either nonpolar InGaN QW active region, or other novel QW design with improved electron–hole wave function overlap. The progress in the high-quality and low-cost GaN substrate is also crucial for nitride lasers, and it is expected that the cost of the substrate will decrease once the market for solid-state lighting increases significantly.

7 Conclusions

QW active regions have led to the highest performing semiconductor lasers, enabling devices with total power conversion efficiencies exceeding 70%. Emission wavelengths from the visible to the mid-IR are now commercially available. New QW materials development is paving the way for wavelength extension (dilute nitride materials) and improved device performance (Al-free materials). High-power device design optimization has led to RT CW output powers now exceeding 20 W from single-stripe, multispatial-mode devices. However, carrier recombination mechanisms, current injection efficiency (below and above threshold), and the radiative efficiency of the QW materials remain areas that need further study. A full understanding of how these mechanisms impact the device temperature sensitivity and maximum CW output power is still necessary. Other remaining challenges include stabilization of a single-spatial mode to high (multiwatt) CW output powers. While this subject was not discussed in this chapter, it remains an area of intense development for QW lasers. The application of QW active regions for visible lasers and LEDs was also discussed, particularly focusing on the use of polar InGaN–GaN QW lasers for blue and blue-green emission.

References

Adachi, M., 2014. InGaN based green laser diodes on semipolar GaN substrate. Japanese Journal of Applied Physics 53, 100207.

Adams, A.R., 1986. Band-structure engineering for low-threshold high-efficiency semiconductor lasers. Electronics Letters 22, 249–250.

Adolfsson, G., Wang, S., Sadeghi, M., *et al.*, 2008. Effects of lateral diffusion on the temperature sensitivity of the threshold current for 1.3-μm double quantum-well GaInNAs–GaAs lasers. IEEE Journal of Quantum Electronics 44, 607–615.

Aggerstam, T., von Wuertemberg, R., Runnstroem, C., Choumas, E., 2002. Large aperture 850-nm oxide-confined VCSELs for 10 Gb/s data communication. In: Proceedings of the SPIE Photonics West 2002, Vertical Cavity Surface Emitting Lasers VI, vol. 4649, pp. 19–24.

Al-Muhanna, A., Mawst, L.J., Botez, D., *et al.*, 1998. High-power (>10 W) continuous wave operations from 100 μm-aperture 0.97 μm emitting Al-free diode lasers. Applied Physics Letters 73, 1182–1184.

Anan, T., Nishi, K., Sugou, S., *et al.*, 1998. GaAsSb: a novel material for 1.3 μm VCSELs. Electronics Letters 34, 2127–2129.

Anton, O., Menoni, C.S., Yeh, J., Tansu, N., Mawst, L.J., 2005a. Increased monomolecular recombination in MOCVD grown InGaAs(N)/GaAsP/GaAs QW lasers from carrier lifetime measurements. IEEE Photonics Technology Letters 17, 953–955.

Anton, O., Xu, L.F., Patel, D., *et al.*, 2005b. Frequency response of strain compensated InGaAsN–GaAsP–GaAs SQW lasers. IEEE Journal of Selected Topics in Quantum Electronics: special issue on semiconductor lasers 11, 1079–1088.

Anton, O., Xu, L.F., Patel, D., *et al.*, 2006. The intrinsic frequency response of 1.3 μm InGaAsN lasers in the range $T=10$–80 °C. IEEE Photonics Technology Letters 18, 1774–1776.

Antonishkis, N.Y., Arsentyev, I.N., Garbuzov, D.Z., *et al.*, 1988. High power CW InGaAsP/GaAs heterostructure lasers with a dielectric mirror Soviet. Technical Physics Letters 14, 310–313.

Arif, R.A., Ee, Y.K., Tansu, N., 2007. Polarization engineering via staggered InGaN quantum wells for radiative efficiency enhancement of light emitting diodes. Applied Physics Letters 91, 091110.

Arif, R.A., Zhao, H., Ee, Y.K., Tansu, N., 2008a. Spontaneous emission and characteristics of staggered InGaN quantum wells light emitting diodes. IEEE Journal of Quantum Electronics 44, 573–580.

Arif, R.A., Zhao, H., Tansu, N., 2008b. Type-II InGaN–GaNAs quantum wells active regions for lasers applications. Applied Physics Letters 92, 011104.

Bakker, J., Acket, G.A., 1977. Single-pass gain measurements on optically pumped $Al_xGa_{(1-x)}As$-$Al_yGa_{(1-y)}As$ double-heterojunction laser structures at room-temperature. IEEE Journal of Quantum Electronics 13, 567–573.

Bank, S.R., Bae, H., Goddard, L.L., *et al.*, 2007. Recent progress on 1.55-μm dilute-nitride lasers. IEEE Journal of Quantum Electronics 43, 773–785.

Belenky, G.L., Donetsky, D.V., Reynolds Jr., C.L., *et al.*, 1997. Temperature performance of 1.3-μm InGaAsP–InP lasers with different profile of p-doping. IEEE Journal of Quantum Electronics 9, 1558–1560.

Belenky, G.L., Reynolds Jr., C.L., Donetsky, D.V., *et al.*, 1999. Role of p-doping profile and regrowth on the static characteristics of 1.3-μm MQW InGaAsP–InP lasers: Experiment and modeling. IEEE Journal of Quantum Electronics 35, 1515–1520.

Bhattacharya, A., Mawst, L.J., Nayak, S., Li, J., Kuech, T.F., 1996. Interface structures of InGaAs/InGaAsP/InGaP quantum well laser diodes grown by metalorganic chemical vapor deposition on GaAs substrates. Applied Physics Letters 68, 2240–2242.

Bhattacharya, P., Klotzkin, D., Qasaimeh, O., *et al.*, 2000. High-speed modulation and switching characteristics of In(Ga)As–Al(Ga)As self-organized quantum-dot lasers. IEEE Journal of Selected Topics in Quantum Electronics 6, 426–438.

Bimberg, D., Kirstaedter, N., Ledentsov, N.N., *et al.*, 1997. InGaAs–GaAs quantum dot lasers. IEEE Journal of Selected Topics in Quantum Electronics 3, 196.

Blum, O., Klem, J.F., 2000. Characteristics of GaAsSb single-quantum-well-lasers emitting near 1.3 μm. IEEE Photonics Technology Letters 12, 771–773.
Bossert, D., Gallant, D., 1996. Improved method for gain/index measurements of semiconductor lasers. Electronics Letters 32, 338–339.
Botez, D., 1999. Design considerations and analytical approximations for high continuous-wave power, broad-waveguide diode lasers. Applied Physics Letters 74, 3102–3104.
Botez, D., Connolly, J.C., 1984. Nonabsorbing-mirror (NAM) CDH–LOC diode lasers. Electronics Letters 20, 53–532.
Botez, D., Mawst, L.J., Bhattacharya, A., *et al*., 1996. 66% CW wallplug efficiency from Al-free 0.98 μm-emitting diode lasers. Electronics Letters 32, 2012–2014.
Bour, D.P., Rosen, A., 1989. Optimal cavity length for high conversion efficiency quantum well diode lasers. Journal of Applied Physics 66, 2813–2818.
Bour, D.P., Treat, D.W., Beernink, K.J., *et al*., 1994. Tensile-strained AlGaAsP and InGaAsP–$(AlGa)_{0.5}In_{0.5}P$ quantum well laser diodes for TM-mode emission in the wavelength range $650 < \lambda < 850$ nm. IEEE Photonics Technology Letters 6, 1283–1285.
Braithwaite, J., Silver, M., Wilkinson, V.A., O'Reilly, E.P., Adams, A.R., 1995. Role of radiative and nonradiative processes on the temperature sensitivity of strained and unstrained 1.5 μm InGaAs(P) quantum well lasers. Applied Physics Letters 67, 3546–3548.
Brunemeir, P.E., Hsieh, K.C., Deppe, D.G., Brown, J.M., Holonyak, J.N., 1985. Interface abruptness and dissolution-induced "damage" in LPE InGaAsP heterostructures. Journal of Crystal Growth 71, 705–710.
Bugge, F., Erbert, G., Fricke, J., *et al*., 2001. 12 W continuous-wave diode lasers at 1120 nm with InGaAs quantum wells. Applied Physics Letters 79, 1965–1967.
Casey Jr., H.C., 1984. Temperature dependence of threshold current density on InP–$Ga_{0.28}In_{0.72}As_{0.6}P_{0.4}$ (1.3 μm) double heterostructure lasers. Journal of Applied Physics 56, 1959–1964.
Cassidy, D.T., 1984. Technique for measurement of the gain spectra of semiconductor diode-lasers. Journal of Applied Physics 56, 3096–3099.
Chand, N., Hobson, W.S., de Jong, J.F., Parayanthal, P., Chakrabarti, U.K., 1996. ZnSe for mirror passivation of high power GaAs based lasers. Electronics Letters 32, 1595–1596.
Chang, Y.C., Kuo, H.C., Lai, F.I., *et al*., 2004. Fabrication and characteristics of high-speed oxide-confined VCSELs using InGaAsP–InGaP strain-compensated MQWs IEEE. Journal of Lightwave Technology 22, 2828–2833.
Chen, W.C., Su, Y.K., Chuang, R.W., *et al*., 2008. Highly strained 1.22-μm InGaAs lasers grown by MOVPE. IEEE Photonics Technology Letters 26, 264–266.
Choi, W., Dapkus, P.D., Jewell, J.J., 1999. 1.2-μm GaAsP/InGaAs strain compensated single-quantum well diode laser on GaAs using metal-organic chemical vapor deposition. IEEE Photonics Technology Letters 11, 1572–1574.
Chuang, S.L., 1995. Physics of Optoelectronic Devices. New York: Wiley.
Chuang, S.L., Chang, C.S., 1996. $K \cdot p$ method for strained wurtzite semiconductors. Physical Review B 54, 2491–2504.
Chuang, S.L., Chang, C.S., 1997. A band-structure model of strained quantum-well wurtzite semiconductors. Semiconductor Science and Technology 12, 252–263.
Coldren, L.A., Corzine, S.W., 1995. Diode Lasers and Photonics Integrated Circuits. New York: Wiley.
Corzine, S.W., Yan, R.H., Coldren, L.A., 1990. Theoretical gain in strained InGaAs/AlGaAs quantum wells including valence-band mixing effects. Applied Physics Letters 57, 2835–2837.
Crump, P., Blume, G., Paschke, K., *et al*., 2009. 20 W continuous wave reliable operation of 980 nm broad-area single emitter diode lasers with an aperture of 96 μm. In: Proceedings of the SPIE 7198, 719814.
Deppe, D.G., Shavritranuruk, K., Ozgur, G., Chen, H., Freisem, S., 2009. Quantum dot laser diode with low threshold and low internal loss. Electron Letters 45, 54.
DeTemple, T.A., Herzinger, C.M., 1993. On the semiconductor laser logarithmic gain-current density relation. IEEE Journal of Quantum Electronics 29, 1246.
Diaz, J., Eliashevich, I., Mobarhan, K., *et al*., 1994. InGaP/InGaAsP/GaAs 0.808 μm separate confinement laser diodes grown by metalorganic chemical vapor deposition. IEEE Photonics Technology Letters 6, 132–134.
Diaz, J., Yi, H.J., Razeghi, M., Burnham, G.T., 1997. Long-term reliability of Al-free InGaAsP/GaAs ($\lambda = 808$ nm) lasers at high-power high-temperature operation. Applied Physics Letters 71, 3042–3044.
Dingle, R., Wiegmann, W., Henry, C.H., 1974. Quantum states of confined carriers in very thin AlGaAs–GaAs–AlGaAs heterostructures. Physical Review Letters 33, 827–830.
Dowd, P., Braun, W., Smith, D.J., *et al*., 1999. Long wavelength (1.3 and 1.5 μm) photoluminescence from InGaAs/GaPAsSb quantum wells grown on GaAs. Applied Physics Letters 75, 1267–1269.
Dupuis, R.D., Dapkus, P.D., Holonyak Jr., N., Rezek, E.A., Chin, R., 1978. Room temperature operation of quantum well $Ga_{1-x}Al_xAs$–GaAs laser diodes grown by metalorganic chemical vapor deposition. Applied Physics Letters 32, 295–297.
Ekenstedt, M.J., Wang, S.M., Andersson, T.G., 1995. Temperature-dependent critical layer thickness for $In_{0.36}Ga_{0.64}As$/GaAs single quantum wells. Applied Physics Letters 58, 854–855.
Epler, J.E., Soechtig, J., Sigg, H.C., 1994. Evolution of surface topography during metalorganic vapor phase epitaxy of InP/InGaAs/InP quantum well heterostructures. Applied Physics Letters 65, 1949–1951.
Epperlein, P.W., Bona, G.L., Roentgen, P., 1992. Local mirror temperatures of red-emitting (Al)GaInP quantum-well laser diodes by Raman scattering and reflectance modulation measurements. Applied Physics Letters 60, 680–682.
Erbert, G., Beister, G., Hülsewede, R., *et al*., 2001. High-power highly reliable Al-free 940-nm diode lasers. IEEE Selected Topics in Quantum Electronics 7, 143–148.
Erbert, G., Bugge, F., Knauer, A., *et al*., 1999. High-power tensile-strained GaAsP–AlGaAs quantum-well lasers emitting between 715 nm and 790 nm. IEEE Journal of Selected Topics in Quantum Electronics 5, 780–784.
Erbert, G., Bugge, F., Knigge, A., *et al*., 2006. Highly reliable 75 W InGaAs/AlGaAs laser bars with over 70% conversion efficiency. Proceedings of the SPIE – The International Society for Optical Engineering 6133.61330B-1–61330B-13.
Evans, A., Darvish, S.R., Slivken, S., *et al*., 2007. Buried heterostructure quantum cascade lasers with high continuous-wave wall plug efficiency. Applied Physics Letters 91, 071101.
Farrell, R.M., Feezell, D.F., Schmidt, M.C., *et al*., 2007. Continuous-wave operation of AlGaN-cladding-free nonpolar m-plane InGaN/GaN laser diodes. Japanese Journal of Applied Physics 46, L761–L763.
Fathpour, S., Mi, Z., Bhattacharya, P., 2005. High-speed quantum dot lasers. Journal of Physics D: Applied Physics 38, 2103.
Fukushima, T., Nagarajan, R., Ishikava, M., Bowers, J.E., 1993. High-speed dynamics in InP based multiple quantum well lasers. Japanese Journal of Applied Physics 32, 70–83.
Gapontsev, V., Berishev, I., Ellis, G., *et al*., 2005. High-efficiency 970- nm multimode pumps. In: Proceedings of the SPIE 5711, 42.
Garbuzov, D.Z., Abeles, J.H., Morris, N.A., *et al*., 1996. High power separate confinement heterostructure AlGaAs/GaAs laser diodes with broadened waveguide. Proceedings of the SPIE 2682, 20–26.
Garbuzov, D.Z., Antonishkis, N.Y., Bondarev, A.D., *et al*., 1991. High-power 0.8 μm InGaAsP-GaAs SCH SQW lasers. IEEE Journal of Quantum Electronics 27, 1531.
Gokhale, M.R., Dries, J.C., Studenkov, P.V., Forrest, S.R., Garbuzov, D.Z., 1997. High-power high-efficiency 0.98-μm wavelength InGaAs–(In)GaAs(P)–InGaP broadened waveguide lasers grown by gas-source molecular beam epitaxy. IEEE Journal of Quantum Electronics 33, 2266–2276.
Groves, S.H., 1992. InGaAs/GaInAsP/GaInP strained-layer quantum well separate-confinement heterostructures grown by OMVPE. Journal of Crystal Growth 124, 747–750.
Hakki, B.W., Paoli, T.L., 1975. Gain spectra in GaAs double-heterostructure injection lasers. Journal of Applied Physics 46, 1299--1306.
Hayakawa, T., 1999. Facet temperature distribution in broad stripe high power laser diodes. Applied Physics Letters 75, 1467–1469.
Hayakawa, T., Asano, H., Wada, M., Fukunaga, T., 1999a. Almost temperature-insensitive characteristics in 1.06 μm InGaAs laser diodes with strain compensating electron-barrier layers. Proceedings of the SPIE – The International Society for Optical Engineering 3626, 109–114.
Hayakawa, T., Wada, M., Yamanaka, F., *et al*., 1999b. Effects of broad-waveguide structure in 0.8 μm high-power InGaAsP/InGaP/AlGaAs lasers. Applied Physics Letters 75, 1839–1841.

Henry, C.H., 1993. The origin of quantum wells and quantum well lasers. In: Zory, P.S. (Ed.), Quantum Well Lasers. New York: Academic Press. pp. 1–16.
Henry, C.H., Logan, R.A., Merritt, F.R., 1980. Measurement of gain and absorption spectra in AlGaAs buried heterostructure lasers. Journal of Applied Physics 51, 3042–3050.
Henry, C.H., Petroff, P.M., Logan, R.A., Merritt, F.R., 1979. Catastrophic damage of AlGaAs double-heterostructure laser materials. Journal of Applied Physics 50, 3721.
Hiramoto, K., Tsuchiya, T., Sagawa, M., Uomi, K., 1994. Multistep formation and lateral variation in the In composition in InGaAs layers grown by metalorganic vapor phase epitaxy on (001) vicinal GaAs substrates. Journal of Crystal Growth 145, 133–139.
Holonyak Jr., N., Kolbas, R.M., Dupuis, R.D., Dapkus, P.D., 1980. Quantum-well heterostructure lasers. IEEE Journal of Quantum Electronics QE-16, 170–186.
Huang, J.Y.T., Mawst, L.J., Kuech, T.F., *et al.*, 2009. Design and characterization of strained InGaAs/GaAsSb type-II 'W' quantum wells on InP substrates for mid-IR emission. Journal of Physics D: Applied Physics 42, 025108.
Huffaker, D.L., Park, G., Zou, Z., Shchekin, O.B., Deppe, D.G., 1998. 1.3 μm Room temperature GaAs-based quantum-dot laser. Applied Physics Letters 73, 2564–2566.
Ijichi, T., Ohkubo, M., Matsumoto, N., Okamoto, H., 1990. Conference Digest 12th IEEE International Semiconductor Laser Conference, Davos, Switzerland, paper D-2.
Ikuta, K., Shihonara, M., Inoue, N., 1995. Interface structures in AlGaAs/GaAs quantum wells grown by metalorganic chemical vapor deposition (MOCVD). Japanese Journal of Applied Physics 34, L220–L222.
Jaschke, G., Averbeck, R., Geelhaar, L., Riechert, H., 2005. Low threshold InGaAsN/GaAs lasers beyond 1500 nm. Journal of Crystal Growth 278, 224.
Kanskar, M., Botez, D., Earles, T., *et al.*, 2005. 73% CW power conversion efficiency at 50 W from 970 nm diode laser bar. Electronics Letters 41, 245–247.
Kawaguchi, M., Miyamoto, T., Gouardes, E., *et al.*, 2001. Lasing characteristics of low threshold GaInNAs lasers grown by metalorganic chemical vapor deposition. Japanese Journal of Applied Physics 40, L744–L746.
Kim, K., Lee, Y.H., 1995. Temperature-dependent critical thickness for strained-layer heterostructures. Applied Physics Letters 67, 2212–2214.
Kim, M., Canedy, C.L., Bewley, W.W., *et al.*, 2008. Interband cascade laser emitting at $\lambda = 3.75$ μm in continuous wave above room temperature. Applied Physics Letters 92, 191110.
Kimura, A., Paulson, C.A., Tang, H.F., Kuech, T.F., 2004. Epitaxial $GaN_{1-y}As_y$ layers with high As content grown by metalorganic vapor phase epitaxy and their band gap energy. Applied Physics Letters 84, 1489–1491.
Knauer, A., Erbert, G., Staske, R., *et al.*, 2005. High-power 808 nm lasers with a super-large optical cavity. Semiconductor Science and Technology 20, 621–624.
Knigge, A., Erbert, G., Jonsson, J., *et al.*, 2005. Passively cooled 940 nm laser bars with 73% wall-plug efficiency at 70 W and 25 C. Electronics Letters 41, 250.
Ko, J., Hegblom, E.R., Akulova, Y., Margalit, N.M., Coldren, L.A., 1997. AlInGaAs/AlGaAs strained-layer 850 nm vertical cavity lasers with very low thresholds. Electronics Letters 33, 1550–1551.
Kondo, T., Schlenker, D., Miyamoto, T., *et al.*, 2000. Lasing characteristics of 1.2 μm highly strained GaInAs/GaAs quantum well lasers. Japanese Journal of Applied Physics 40, 467–471.
Kondow, M., Kitatani, T., Nakatsuka, S., *et al.*, 1997. GaInNAs: a novel material for long wavelength semiconductor lasers. IEEE Journal of Selected Topics in Quantum Electronics 3, 719–730.
Koyama, F., Schlenker, D., Miyamoto, T., *et al.*, 1999. 1.2 μm highly strained GaInAs/GaAs quantum well lasers for single mode fiber datalink. Electronics Letters 35, 1079–1081.
Lang, R.J., Mehuys, D., Hardy, A., Dzurko, K.M., Welch, D.F., 1993. Spatial evolution of filaments in broad area diode laser amplifiers. Applied Physics Letters 62, 1209–1211.
Lee, J.J., Mawst, L.J., Botez, D., 2003. Improved performance InGaAs/InGaAsP asymemetric broad waveguide diode lasers via waveguide core doping. Electronics Letters 39, 1250–1252.
Lester, L.F., Offsey, S.D., Ridley, B.K., *et al.*, 1991. Comparison of the theoretical and experimental differential gain in strained layer InGaAs/GaAs quantum well lasers. Applied Physics Letters 59, 1162.
Liau, Z.L., Palmateer, S.C., Groves, S.H., Waipole, J.N., Missaggia, L.J., 1992. Low-threshold InGaAs strained-layer quantum-well lasers ($\lambda = 0.98$ μm) with GaInP cladding layers and mass-transported buried heterostructure. Applied Physics Letters 60, 6–8.
Lim, G, Park, Y, Zmudzinski, CA, *et al.*, 1991. SPIE laser Diode Technology and Applications III. San Jose, CA, vol. 1418, p. 123.
Mawst, L.J., Bhattacharya, A., Lopez, J., *et al.*, 1996. 8 W continuous wave front-facet power from broad-waveguide al-free 980 nm diode lasers. Applied Physics Letters 69, 1532–1534.
Mawst, L.J., Bhattacharya, A., Nesnidal, M., *et al.*, 1995. High CW output power InGaAs/InGaAsP/InGaP diode lasers: Effect of substrate misorientation. Applied Physics Letters 67, 2901–2903.
Mawst, L.J., Rusli, S., Al-Muhanna, A., Wade, J.K., 1999. Short-wavelength (0.7 μm $< \lambda < 0.78$ μm) high-power InGaAsP-active diode lasers IEEE. Journal of Selected Topics in Quantum Electronics 5, 785–791.
Mawst, L.J., Yang, H., Nesnidal, M., *et al.*, 1998. High-power, single-mode, Al-free InGaAs(P)/InGaP/GaAs distributed feedback diode lasers. Journal of Crystal Growth 195, 609–615.
McIlroy, P.W.A., Kurobe, A., Uematsu, Y., 1985. Analysis and application of theoretical gain curves to the design of multi-quantum well lasers. IEEE Journal of Quantum Electronics 21, 1958.
Meyer, C.A., Hoffman, C.A., Bartoli, F.J., Ram-Mohan, L.R., 1995. Type-II quantum-well lasers for the mid-wavelength infrared. Applied Physics Letters 67, 757–759.
Mitsuhara, M., Ogasawara, M., Oishi, M., Sugiura, H., 1998. Metalorganic molecular-beam-epitaxy-grown $In_{0.77}Ga_{0.23}As$/InGaAs multiple quantum well lasers emitting at 2.07 μm wavelength. Applied Physics Letters 72, 3106–3108.
Mogg, S., Chitica, N., Schatz, R., Hammar, R., 2002. Properties of highly strained InGaAs/GaAs quantum wells for 1.2-μm laser diodes. Applied Physics Letters 81, 2334–2336.
Mukai, K., Nakata, Y., Otsubo, K., *et al.*, 1999. 1.3-μm CW lasing of InGaAs/GaAs quantum dots at room temperature with a threshold current of 8 mA. IEEE Photonics Technology Letters 11, 1205–1207.
Nagahama, S., Iwasa, N., Senoh, M., *et al.*, 2000. High power and long-lifetime InGaN multi-quantum-well laser diodes grown on low-dislocation-density GaN substrate. Japanese Journal of Applied Physics 39, L647–L650.
Nagahama, S, Sugimoto, Y, Kozaki, T, Mukai, T, 2005. Recent progress of AlInGaN laser diodes. In: Proceeding of SPIE Photonics West, San Jose, CA.
Nagarajan, R., Bowers, J.E., 1993. Effects of carrier transport on injection efficiency and wavelength chirping in quantum-well lasers. IEEE Journal of Quantum Electronics 29, 1601–1608.
Nagarajan, R., Ishikawa, M., Fukushima, T., Geels, R.S., Bowers, J.E., 1992. High speed quantum-well lasers and carrier transport effects. IEEE Journal of Quantum Electronics 28, 1990–2008.
Nakamura, S., Fasol, G., Pearton, S.J., 2000. The Blue Laser Diodes: The Complete Story. Berlin: Springer.
Nakamura, S., Senoh, M., Nagahama, S., *et al.*, 1996. Room-temperature continuous-wave operation of InGaN multi-quantum-well structure laser diodes. Applied Physics Letters 69, 4056–4058.
Nakamura, S., Senoh, M., Nagahama, S., *et al.*, 1997a. Room-temperature continuous-wave operation of InGaN multi-quantum-well structure laser diodes with a lifetime of 27 hours. Applied Physics Letters 70, 1417–1419.
Nakamura, S., Senoh, M., Nagahama, S., *et al.*, 1997b. High-power, long-lifetime InGaN multi-quantum-well-stucture laser diodes Japanese. Journal of Applied Physics 36, L1059–L1061.
Nakamura, S., Senoh, M., Nagahama, S., *et al.*, 1997c. InGaN/GaN/AlGaN-based laser diodes with modulation doped strained-layer superlattices Japanese. Journal of Applied Physics 36, L1568–L1571.

Namegaya, T., Matsumoto, N., Yamanaka, N., *et al.*, 1994. Effects of well numbers in 1.3-μm GaInAsP/InP GRIN-SCH strained-layer quantum-well lasers. IEEE Journal of Quantum Electronics 30, 578–584.
Ng, H.M., 2002. Molecular-beam epitaxy of GaN/$Al_xGa_{1-x}N$ multiple quantum wells on R-plane (10(1)2) sapphire substrates. Applied Physics Letters 80, 4369–4371.
Nomoto, E., Taniguchi, T., Ohtoshi, T., *et al.*, 2008. 700–730 nm InGaAsP quantum well ridge-waveguide lasers. In: Proceedings of the SPIE – The International Society for Optical Engineering 6909.69091C-1–69091C-8.
Offsey, S.D., Lester, L.F., Schaff, W.J., Eastman, L.F., 1991. High-speed modulation of strained-layer InGaAs–GaAs–AlGaAs ridge waveguide multiple quantum well lasers. Applied Physics Letters 58, 2336.
Ohkubo, M., Ijichi, T., Iketani, A., Kikuta, T., 1994. 980-nm aluminum-free InGaAs/InGaAsP/InGaP GRIN-SCH SL-QW lasers. Journal of Quantum Electronics 30, 408–414.
Okamoto, K., Kashiwagi, J., Tanaka, T., Kubota, M., 2009. Nonpolar m-plane InGaN multiple quantum well laser diodes with a lasing wavelength of 499.8 nm. Applied Physics Letters 94, 071105.
Okamoto, K., Tanaka, T., Kubota, M., 2008. High-efficiency continuous-wave operation of blue-green laser diodes based on nonpolar m-plane gallium nitride. Applied Physics Express 1, 072201.
Onabe, K., 1982. Calculation of miscibility gap in quatemary InGaAsPs with strictly regular solution. Japanese Journal of Applied Physics 21, 797–798.
O'Reilly, E.P., Silver, M., 1993. Temperature sensitivity and high temperature operation of long wavelength semiconductor lasers. Applied Physics Letters 63, 3318–3320.
Oosenbrug, A., Latta, E.-E., 1994. High-power operational stability of 980 nm pump lasers for EDFA applications. In: Conference Proceedings of the Lasers and Electro-Optics Society Annual Meeting, vol. 2, pp. 37–38.
Oster, A., Bugge, F., Erbert, G., Wenzel, H., 1999. Gain spectra measurement of strained and strain-compensated InGaAsP–AlGaAs laser structures for $\lambda = 800$ nm. IEEE Journal of Selected Topics in Quantum Electronics 5, 631–636.
Oster, A., Erbert, G., Wenzel, H., 1997. Gain spectra measurements by a variable stripe length method with current injection. Electronics Letters 33, 864–866.
Palmer, D.J., Smowton, P.M., Blood, P., *et al.*, 2005a. The effect of nitrogen on the gain and efficiency in InGAsN QW lasers. Applied Physics Letters 86, 071121.
Palmer, D.J., Smowton, P.M., Blood, P., *et al.*, 2005b. The effect of temperature on the efficiency of InGaAs and InGaAsN quantum well laser structures. In: Proceedings of the Conference on Lasers and Electro-Optics (CLEO), vol. 1, pp. 101–103.
Park, J., Kawakami, Y., 2006. Photoluminescence property of InGaN single quantum well with embedded AlGaN δ layer. Applied Physics Letters 88, 202107.
Park, S.H., Park, J., Yoon, E., 2007. Optical gain in InGaN/GaN quantum well structures with embedded AlGaN delta layer. Applied Physics Letters 90, 023508.
People, R., Bean, J.C., 1985. Calculation of critical layer thickness versus lattice mismatch for Ge_xSi_{1-x}/Si strained-layer heterostructures. Applied Physics Letters 47, 322–324.
Peter, M., Kiefer, R., Fuchs, F., *et al.*, 1999. Light-emitting diodes and laser diodes based on a $Ga_{1-x}In_xAs/GaAs_{1-y}Sb_y$ type II superlattice on InP substrate. Applied Physics Letters 74, 1951–1953.
Peters, M., Rossin, V., Everett, M., Zucker, E., 2007. High power, high efficiency laser diodes at JDSU. In: Zediker, M. (Ed.), High Power Technology and Applications V. Proceedings – SPIE the International Society for Optical Engineering, vol. 6456, p. 64560G.
Petrescu-Prahova, I.B., Modak, P., Goutain, E., *et al.*, 2008. 253 mW/μm maximum power density from 9xx nm epitaxial laser structures with d/Γ greater than 1 μm. In: Proceedings of IEEE 21st International Semiconductor Laser Conference (ISLC), p. 135.
Phillips, A.F., Sweeney, S., Adams, A.R., Thijs, P.J.A., 1999. Temperature dependence of 1.3- and 1.5-μm compressively strained InGaAs(P) MQW semiconductor lasers. IEEE Journal of Selected Topics in Quantum Electronics 5, 401–412.
Pikhtin, N.A., Slipchenko, S.O., Sokolova, Z.N., *et al.*, 2004. 16 W continuous-wave output power from 100 μm-aperture laser with quantum well asymmetric heterostructure. Electronics Letters 40, 1413.
Ressel, P., Erbert, G., Zeimer, U., *et al.*, 2005. Novel passivation process for the mirror facets of Al-free active-region high-power semiconductor diode lasers. IEEE Photonics Technology Letters 17, 962–964.
Roberts, J.S., David, J.P.R., Chen, Y.H., Sale, T.E., 1997. Optical properties of MOVPE grown $Al_xGa_{1-x}As$ quantum wells. Journal of Crystal Growth 170, 621–625.
Roberts, J.S., David, J.P.R., Smith, L., Tihanyi, P., 1998. The influence of trimethylindium impurities on the performance of InAlGaAs single quantum well lasers. Journal of Crystal Growth 195, 668–675.
Rusli, S., Al-Muhanna, A., Earles, T., Mawst, L.J., 2000. 1 W CW reliable $\lambda = 730$ nm aluminum-free active layer diode lasers. Electronics Letters 36, 630–631.
Ryu, S.W., Dapkus, P.D., 1999. Low threshold current density GaAsSb quantum well (QW) lasers grown by metal organic chemical vapour deposition on GaAs substrates. Electronics Letters 36, 1387–1388.
Sale, T.E., Amamo, C., Ohiso, Y., Kurokawa, T., 1997. Using strained lasers $(Al_xGa_{1-x})_yIn_{1-y}AszP_{1-z}$ system materials to improve the performance of 850 nm surface- and edge-emitting lasers. Applied Physics Letters 71, 1002–1004.
Sato, S., 2000. Low threshold and high characteristics temperature 1.3 μm range GaInNAs lasers grown by metalorganic chemical vapor deposition. Japanese Journal of Applied Physics 39, 3403–3405.
Sato, S., Satoh, S., 1999a. Room-temperature continuous-wave operation of 1.24-μm GaInNAs lasers grown by metal–organic chemical vapor deposition. IEEE Journal of Selection Topics in Quantum Electronicics 5, 707–710.
Sato, S., Satoh, S., 1999b. 1.21 μm Continuous-wave operation of highly strained GaInAs quantum well lasers on GaAs substrates Japanese. Journal of Applied Physics 38, L990–L992.
Savolainen, P., Toivonen, M., Melanen, P., *et al.*, 1999. Solid source molecular beam epitaxy growth of low threshold and high temperature 1.3 μm AlGaInAs–AlInAs–InP laser diodes suitable for uncooled application. In: Proceedings 11th IPRM, pp. 99–102.
Schlenker, D., Miyamoto, T., Chen, Z.B., *et al.*, 2000. Critical layer thickness of 1.2-μm highly strained GaInAs/GaAs quantum wells. Journal of Crystal Growth 221, 503–508.
Schneider, R.P., Hagerott-Crawford, M., 1995. GaInAsP/AlGaInP-based near-IR (780 nm) vertical-cavity surface-emitting lasers. Electronics Letters 31, 554–556.
Schubert, E.F., 2006. Light Emitting Diodes, 2nd edn. Cambridge, UK: Cambridge University Press.
Sebastian, J., Beister, G., Bugge, F., *et al.*, 2001. High-power 810-nm GaAsP–AlGaAs diode lasers with narrow beam divergence. IEEE Journal of Selected Topics in Quantum Electronics 7, 334.
Sellin, R.L., Ribbat, Ch., Grundmann, M., Ledentsov, N.N., Bimberg, D., 2001. Close-to-ideal device characteristics of high-power InGaAs/GaAs quantum dot lasers. Applied Physics Letters 78, 1207–1209.
Shaklee, K.L., Leheny, R.F., 1971. Direct determination of optical gain in semiconductor crystals. Applied Physics Letters 18, 475–477.
Sharma, T.K., Arora, B.M., Kumar, S., Gokhale, M.R., 2002. Effect of growth temperature on strain barrier for metalorganic vapor phase epitaxy grown strained InGaAs quantum well with lattice matched InGaAsP barriers. Journal of Applied Physics 91, 5875–5881.
Shigihara, K., Nagai, Y., Karakida, S., *et al.*, 1991. High-power operation of broad-area laser diodes with GaAs and AlGaAs single quantum wells for Nd:YAG laser pumping. IEEE Journal of Quantum Electronics QE-27, 1537–1543.
Shterengas, L., Belenky, G., Yeh, J., Tansu, N., Mawst, L.J., 2004. Differential gain and linewidth enhancement factor and differential gain in dilute-nitride single-quantum well diode lasers. In: CLEO 2004, San Francisco, CA, May.
Shterengas, L., Belenky, G., Yeh, J., Tansu, N., Mawst, L.J., 2005. Differential gain and linewidth enhancement factor in dilute-nitride GaAs-based 1.3 μm diode lasers. IEEE Journal of Selected Topics in Quantum Electronics: Special Issue on Semiconductor Lasers 11, 1063–1068.
Smowton, P.M., Blood, P., 1997. IEEE Journal of Selected Topics in Quantum Electronics 3, 491.
Smowton, P.M., Hermann, E., Ning, Y., Summers, H.D., Blood, P., 2001. Optical mode loss and gain of multiple-layer quantum-dot lasers. Applied Physics Letters 78, 2629–2631.

Stintz, A., Liu, G.T., Li, H., Lester, L.F., Malloy, K.J., 2000. Low-threshold current density 1.3 – μm quantum-dot lasers with the dots-in-a-Well (DWELL) structure. IEEE Photonics Technology Letters 12, 591–593.
Stringfellow, G.B., 1989. Organometallic Vapor-Phase Epitaxy, first ed. San Diego, CA: Academic Press.
Sugimura, A., 1983. Auger recombination effect on the threshold current of InGaAsP quantum well lasers. IEEE Journal of Quantum Electronics QE-19, 932–941.
Sumpf, B., Beister, G., Erbert, G., *et al.*, 2001. 2W Reliable operation of $\lambda = 735$ nm GaAsP/AlGaAs laser diodes. Electronics Letters 37, 351–352.
Sundgren, P., Berggren, J., Goldman, P., Hammar, M., 2005. Highly strained InGaAs/GaAs multiple quantum-wells for laser applications in the 1200–1300 nm wavelength regime. Applied Physics Letters 87, 071104.
Sweeney, S.J., Phillips, A.F., Adams, A.R., O'Reilly, E.P., Thijs, P.J.A., 1998. The effect of temperature dependent processes on the performance of 1.5-μm compressively strained InGaAs(P) MQW semiconductor diode lasers. IEEE Photonics Technology Letters 10, 1076–1078.
Syrbu, A.V., Yakovlev, V.P., Suruceanu, G.I., *et al.*, 1996. ZnSe-facet-passivated InGaAs/InGaAsP/InGaP diode lasers of high CW power and 'wallplug' efficiency. Electronics Letters 32, 352–354.
Takeuchi, T., Chang, Y.-L., Leary, M., *et al.*., 2001. Low threshold 1.3 μm InGaAsN vertical cavity surface emitting lasers grown by metalorganic chemical vapor deposition. In: IEEE LEOS 2001 Post-Deadline Session San Diego, CA, November.
Takeuchi, T., Chang, Y.-L., Tandon, A., *et al.*, 2002. Low threshold 1.2 μm InGaAs quantum well lasers grown under low As/III ratio. Applied Physics Letters 80, 2445–2447.
Tanaka, S., Hiramatsu, K., Habu, Y., Sawaki, N., Akasaki, I., 1986. The initial stage of LPE growth of InGaAsP on GaAs in the region of immiscibility. Journal of Crystal Growth 79, 978–983.
Tansu, N., Chang, Y.-L., Takeuchi, T., *et al.*, 2002a. Temperature analysis and characteristics of highly-strained InGaAs(N)–GaAsP–GaAs ($\lambda > 1.17$ μm) quantum well lasers. IEEE Journal of Quantum Electronics 38, 640–651.
Tansu, N., Mawst, L.J., 2001. High-performance, strain compensated InGaAs–GaAsP–GaAs ($\lambda = 1.17$ μm) quantum well diode lasers. IEEE Photonics Technology Letters 13, 179–181.
Tansu, N., Mawst, L.J., 2003b. The role of hole-leakage in 1300-nm InGaAsN quantum well lasers. Applied Physics Letters 82, 1500–1502.
Tansu, N., Mawst, L.J., 2005. Current injection efficiency of InGaAsN lasers. Journal of Applied Physics 97, 054502.
Tansu, N., Quandt, A., Kanskar, M., Mulhearn, W., Mawst, L.J., 2003a. High-performance and high-temperature continuous-wave-operation 1300-nm InGaAsN quantum well lasers by organometallic vapor phase epitaxy. Applied Physics Letters 83, 18–20.
Tansu, N., Yeh, J., Mawst, J., 2003b. Extremely-low threshold-current-density InGaAs quantum well lasers with emission wavelength of 1215–1233 nm. Applied Physics Letters 82, 4038–4040.
Tansu, N., Yeh, J.Y., Mawst, L.J., 2003c. Experimental evidence of carrier leakage in InGaAsN quantum well lasers. Applied Physics Letters 83, 2112–2114.
Tansu, N., Yeh, J.Y., Mawst, L.J., 2004. Physics and characteristics of high performance 1200 nm InGaAs and 1300–1400 nm InGaAsN QW lasers obtained by MOCVD. Journal of Physics: Condensed Matter 16, S3277.
Tansu, N., Zhou, D., Mawst, L.J., 2000. Low temperature sensitive, compressively-strained InGaAsP active ($\lambda = 0.78$–0.85 μm) region diode lasers. IEEE Photonics Technology Letters 12, 603–605.
Thomson, J.D., Summers, H.D., Hulyer, P.J., Smowton, P.M., Blood, P., 1999. Determination of single-pass optical gain and internal loss using a multisection device. Applied Physics Letters 75, 2527–2529.
Tsao, J.Y., 1993. Materials Fundamentals of Molecular Beam Epitaxy. Boston, MA: Academic Press, Chapter 5, pp.183–186.
Tsvid, G, Kirch, J, Mawst, L.J, *et al.*, 2007. Radiative efficiency of InGaAs/GaAs quantum well lasers. In: IEEE LEOS Annual Meeting, November, Orlando, FL, p. 11.
Vahala, K.J., Zah, C.E., 1988. Effect of doping on the optical gain and spontaneous noise enhancement factor in quantum well amplifiers and lasers studied by simple analytic expressions. Applied Physics Letters 52, 1945–1947.
Vurgaftman, I., Felix, C.L., Bewley, W.W., *et al.*, 2001. Mid-infrared 'W' lasers. Philosophical Transactions of the Royal Society of London Series A 359, 489–503.
Valster, A., Meney, A.T., Downes, J.R., *et al.*, 1997. Strain-overcompensated GaInP–AlGaInP quantum-well laser structures for improved reliability at high-output powers. IEEE Journal of Selected Topics in Quantum Electronics 3, 180–187.
Vurgaftman, I., Meyer, J.R., 2003. Band parameters for nitrogen-containing semiconductors. Journal of Applied Physics 94, 3675–3696.
Vurgaftman, I., Meyer, J.R., Tansu, N., Mawst, L.J., 2003. (In)GaAsN–GaAsSb Type-II 'W' quantum-well lasers for emission at $\lambda = 1.55$ μm. Applied Physics Letters 83, 2742–2744.
Wade, J.K., Mawst, L.J., Botez, D., *et al.*, 1997. High continuous wave power, 0.8 μm-band, Al-free active-region diode lasers. Applied Physics Letters 70, 149–152.
Wade, J.K., Mawst, L.J., Botez, D., Morris, J.A., 1998. 8.8 W CW power from broad-waveguide Al-free active region ($\lambda = 0.805$ μm) diode lasers. Electronics Letters 35, 1100–1102.
Wang, S.M., Zhao, H., Adolfsson, G., *et al.*, 2009. Dilute nitrides and 1.3 μm GaInNAs quantum well lasers on GaAs. Microelectronics Journal 40, 386.
Walker, C.L., Bryce, A.C., Marsh, J.H., 2002. Improved catastrophic optical damage level from laser with nonabsorbing mirrors. IEEE Photonics Technology Letters 14, 1394–1396.
Waltereit, P., Brandt, O., Trampert, A., *et al.*, 2000. Nitride semiconductors free of electrostatic fields for efficient white light-emitting diodes. Nature 406, 865–868.
Waters, R.G., Bour, D.P., Yellen, S.L., Ruggieri, N.F., 1990. Inhibited dark-line defect formation in strained InGaAs/AlGaAs quantum well lasers. IEEE Photonics Technology Letters 2, 531–533.
Whiteaway, J.E.A., Thompson, G.H.B., Greene, P.D., Glew, R.W., 1991. Logarithmic gain/current-density characteristic of InGaAs/InGaAlAs/InP multi-quantum-well separate-confinement heterostructure lasers. Electronics Letters 27, 340.
Wilmsen, C., Temkin, H., Coldren, L.A., 1999. Vertical-Cavity Surface-Emitting Lasers. Cambridge: Cambridge University Press, Chapter 9, p. 345.
Wu, J., Walukiewicz, W., Yu, K.M., *et al.*, 2004. Valence band hybridization in N-rich $GaN_{1-x}As_x$ alloys. Physical Review B 70, 115214.
Xiao, D., Kim, K.W., Bedair, S.M., Zavada, J.M., 2004. Design of white light-emitting diodes using InGaN/AlInGaN quantum-well structures. Applied Physics Letters 84, 672–674.
Yablonovitch, E., Kane, E.O., 1986. Reduction of lasing threshold current-density by the lowering of valence band effective mass. Journal of Lightwave Technology 4, 504–506.
Yeh, J., Mawst, L.J., Tansu, N., 2005. The role of carrier transport on the current injection efficiency of InGaAsN quantum-well lasers. IEEE Photonics Technology Letters 17, 1779–1781.
Yellen, S.L., Shepard, A.H., Dalby, R.J., *et al.*, 1993. Reliability of GaAs-based semiconductor diode lasers: 0.6–1.1 μm. IEEE Journal of Quantum Electronics 29, 2058–2067.
Yellen, S.L., Shepard, A.H., Harding, C.M., *et al.*, 1992. Dark-line-resistant, aluminum-free diode laser at 0.8 μm. IEEE Photonics Technology Letters 4, 1328–1330.
Yonezu, H., Sakuma, I., Kamejima, T., *et al.*, 1979. High optical power density emission from a 'window-stripe' AlGaAs double-heterostructure laser. Applied Physics Letters 34, 637–639.
Yoo, J.S., Lee, H.H., Zory, P., 1991a. Enhancement of output intensity limit of semiconductor lasers by chemical passivation of mirror facets. IEEE Photonics Technology Letters 3, 202–204.
Yoo, J.S., Lee, H.H., Zory, P., 1991b. On surface recombination velocity and output intensity limit of pulsed semiconductor lasers. IEEE Photonics Technology Letters 3, 594–596.
Yoo, J.S., Lee, H.H., Zory, P., 1992. Temperature rise at mirror facet of CW semiconductor lasers. IEEE Journal of Quantum Electronics 28, 635–637.
York, P.K., Connolly, J.C., Hughes, N.A., *et al.*, 1992. MOCVD regrowth over GaAs/AlGaAs gratings for high power long-lived InGaAs/AlGaAs lasers. Journal of Crystal Growth 124, 709–715.

Zhao, H., Arif, R.A., Ee, Y.K., Tansu, N., 2009a. Self-consistent analysis of strain-compensated InGaN–AlGaN quantum wells for lasers and light-emitting diodes. IEEE Journal of Quantum Electronics 44, 66–78.
Zhao, H., Arif, R.A., Tansu, N., 2009b. Design analysis of staggered InGaN quantum wells light-emitting diodes at 500–540 nm. IEEE Journal of Selected Topics in Quantum Electronics 15, 1104–1114.
Zmudzinski, C.A., Zory, P.S., Lim, G.G., *et al.*, 1991. Differential gain in bulk and quantum well diode lasers. IEEE Photonics Technology Letters 3, 1057–1060.
Zory, P.S., Reisinger, A.R., Mawst, L.J., *et al.*, 1986. Anomalous length dependence of the threshold for thin quantum well diode lasers. Electronics Letters 22, 475–477.
Zou, Y., Osinski, J.S., Grodzinski, P., *et al.*, 1993. Experimental study of auger recombination, gain, and temperature sensitivity of 1.5 μm compressively strained semiconductor lasers. IEEE Journal of Quantum Electronics 29, 1565–1574.

Further Reading

Blood, P., Lewis, G.M., Smowton, P.M., *et al.*, 2003. Characterization of semiconductor laser gain media by the segmented contact method. IEEE Journal of Selected Topics in Quantum Electronics 9, 1275–1282.
Borchert, B., Egorov, A.Y., Illek, S., Riechert, H., 2000. Static and dynamics characteristics of 1.29 μm GaInNAs ridge-waveguide laser diodes. IEEE Photonics Technology Letters 12, 597–599.
Dmitry, Z., Garbuzov, N., Yu., Antonishkis, *et al.*, 1991. High-power 0.8 μm InGaAsP–GaAs SCH SQW lasers. IEEE Journal of Quantum Electronics 6, 1531–1535.
Fehse, R., Tomic, S., Adams, A.R., *et al.*, 2002. A quantitative study of radiative, Auger, and defect related recombination processes in 1.3-μm GaInNAs-based quantum-well lasers. IEEE Journal of Selected Topics in Quantum Electronics 8, 801–810.
Fukunaga, T., Wada, M., Hayakawa, T., 1999. High-power 0.8 μm InGaAsP/InGaP/AlGaAs single quantum well lasers with tensile-strained InGaP barriers. Japanese Journal of Applied Physics 38, L387–L389.
Gokhale, M.R., Studenkov, P.V., Wei, J., Forrest, S.R., 2000. Low-threshold current, high efficiency 1.3-mm wavelength aluminium-free InGaAsN-based quantum-well lasers. IEEE Photonics Technology Letters 12, 131–133.
Hohnsdorf, F., Koch, J., Leu, S., *et al.*, 1999. Reduced threshold current densities of (GaIn)(Nas)/GaAs single quantum well lasers for emission wavelengths in the range 1.28–1.38 μm. Electronics Letters 35, 571–572.
Kamoto, K., Niki, I., Shvartser, A., *et al.*, 2004. Surface-plasmon-enhanced light emitters based on InGaN quantum wells. Nature Materials 3, 601–605.
Livshits, D.A., Egorov, A.Yu., Riechert, H., 2000a. 8 W continuous wave operation of InGaAsN lasers at 1.3 μm. Electronics Letters 36, 1381–1382.
Livshits, D.A., Kochnev, I.V., Lantratov, V.M., *et al.*, 2000b. Improved catastrophic optical mirror damage level in InGaAs/AlGaAs laser diodes. Electronics Letters 36, 1848–1849.
Ohkubo, M., Ijichi, T., Iketani, A., Kikuta, T., 1992. Aluminum free InGaAs/GaAs/InGaAsP/InGaP GRIN-SCH SL-SQW lasers at 0.98 μm. Electronics Letters 28, 1149–1150.
Schatz, R., Bethea, C., 1994. Steady state model for facet heating leading to thermal runaway in semiconductor lasers. Journal of Applied Physics 76, 2509–2521.
Shchekin, O.B., Deppe, D.G., 2002. Low-threshold high-to 1.3-μm InAs quantum-dot lasers due to p-type modulation doping of the active region. IEEE Photonics Technology Letters 14, 1231.
Swerdlov, B., Muller, J., Pawlik, S., *et al.*, 2007. Broad area single emitter (BASE) modules with improved brightness. In: Proceedings of the European Conference on Lasers and Electro-Optics, Digital Object Identifier 10.1109/CLEOE-IQEC.2007.4385944.
Tansu, N., Kirsch, N.J., Mawst, L.J., 2002. Low-threshold-current-density 1300-nm dilute-nitride quantum well lasers. Applied Physics Letters 81, 2523–2525.
Tansu, N, Mawst, L.J., 2000. Compressively-strained InGaAsP-active ($\lambda = 0.85$ μm) VCSELs. In: Proceedings of LEOS'00, Rio Grande, Puerto Rico, pp. 724–725.
Tansu, N., Mawst, L.J., 2002a. Low-threshold strain-compensated InGaAs(N) ($\lambda = 1.19$–1.31 μm) quantum well lasers. IEEE Photonics Technology Letters 14, 444–446.
Tansu, N., Mawst, L.J., 2002b. Temperature sensitivity of 1300-nm InGaAsN quantum-well lasers. IEEE Photonics Technology Letters 14, 1052–1054.
Tansu, N., Mawst, L.J., 2003. Design analysis of 1550-nm GaAsSb–(In)GaAsN type-II quantum well laser active regions. IEEE Journal of Quantum Electronics 39, 1205–1210.
Tansu, N., Yeh, J.Y., Mawst, L.J., 2003. Low-Threshold 1317-nm InGaAsN Quantum Well Lasers with GaAsN Barriers. Applied Physics Letters 83, 2512–2514.
Tsvid, G., Kirch, J., Mawst, L.J., *et al.*, 2008. Spontaneous radiative efficiency and gain characteristics of strained-layer InGaAs–GaAs quantum-well lasers. IEEE Journal of Quantum Electronics 44, 732–739.
Vurgaftman, I., Meyer, J.R., Tansu, N., Mawst, L.J., 2004. InP-based dilute-nitride mid-infrared type-II 'W' quantum-well lasers. Journal of Applied Physics 96, 4653–4655.